WATER PROOF Marine Consultancy & Services BV.

Utrecht University

Master Thesis

Modelling the long term evolution of observed tidal sand waves in the North Sea

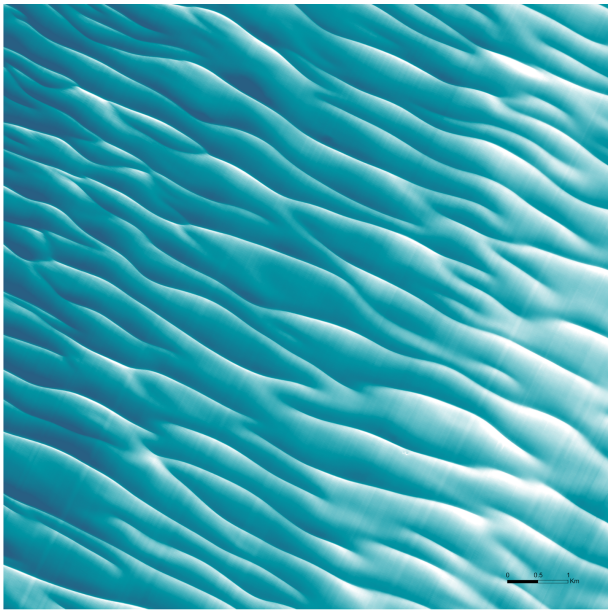

Author
Janneke
Krabbendam
5769183

Supervisors
Prof. dr. H.E. de Swart (IMAU)
Dr. A. Nnafie (IMAU/WaterProof B.V.)
Ir. L. M. Perk (WaterProof B.V.)

Climate Physics
Institute for Marine and Atmospheric Research

August 22, 2018

Figure: WaterProof B.V., 2017

Abstract

Sand waves on the outer shelf are rhythmic bedforms with wavelengths of 100-1000 m, wave heights up to 10 m and they can reach migration speeds of up to 10 m year^{-1}. Because of their dynamic nature these movements may expose cables and pipelines. Since the burial of cables and pipelines is a costly procedure, there is a need to determine the optimum burial depth for cables and pipelines. Specifically, the migration direction and speed and trough depth are of interest and what physical processes drive these dynamics. So far, the behaviour of sand waves has been assessed empirically by extrapolating trends from historical bathymetry data. However, this leads to uncertain results and is limited by the lack of good quality bathymetry data. Therefore, there is a demand to study the longterm evolution of sand waves with the use of process-based models.

The models so far used idealized settings to model the behaviour of sand waves. Here, the focus is on a recently published paper, where the finite-amplitude behaviour of tidal sand waves is modelled using the numerical model Delft3D. This nonlinear model is based on the 2DV shallow water equations coupled to sediment continuity and adapted in order to simulate sand waves in an observed situation in the North Sea. Therefore, first a sensitivity analysis towards numerical settings was performed, which showed that careful choices of these parameters is essential for robust model results.

Next, the sensitivity of the modelled sand waves to environmental parameters was studied. Decreasing the mean water depth H_0 or increasing the median sand grain size d_{50} results in higher initial growth rates and shorter equilibrium timescales. A smaller H_0 lead to shallower trough depths. A larger d_{50} lead to a higher saturation crest height, but the equilibrium trough depth was not affected significantly. When the bed slope parameter α_{bs} is increased, the growth rate decreases, because the slope induced sand transport is enhanced. Increasing the M_2 current amplitude that is imposed on the boundaries of the domain, caused the sand waves to move towards a different equilibrium state with both a larger wave height and length. Finally, including overtides or residual currents does not affect the growth significantly, but typically causes sand waves to migrate in the direction of the peak tidal flow.

As a final step the model was applied to an observed sand wave field in the North Sea. Mainly the migration rate was overpredicted and the modelled height of the sand waves was lower than measured. These issues could be solved in the future by including more tidal constituents, the effect of storms and waves, a spatially variable d_{50}, grain size sorting and 3D effects.

Acknowledgments

First of all, I would like to thank my supervisor Huib de Swart for the time he invested in me, for his constructive feedback and for sharing his knowledge with me. I would also like to thank Abdel Nnafie, for the good cups of espresso and tea while always being available to help, for feedback, discussions and words of encouragement when needed. Special thanks to everyone at WaterProof B.V., Luitze, Roelant, Kimberley, Joost and Marijke, for the nice lunch walks, the interesting discussions, the loads of cake and the great trip on the Bumblebee. Thank you, Bas Borsje, for sharing your experience with me. I would also like to thank Tjebbe and Jinyang who listened to all my practice presentations, for your suggestions and feedback. Thank you to my fellow students Joanne, Manon and Febru for the great and helpful coffee and lunch breaks. And finally, I want to thank Ruben, Annemarie and my parents for their understanding and words of encouragement. I am very much looking forward to continuing this project for the next four years!

Contents

Chapter 1

Introduction

Coastal seas lie between the coastline and the continental slope, the latter being the edge of the continental shelf at approximately 100-200 m depth (Masselink et al., 2014). They interact freely with the deep ocean. The coastal sea can be separated into two parts: the shoreface and the shelf. The transition is marked by a change in the bed slope: the shelf is characterised by bed slopes smaller than 10^{-3} m $^{-1}$. These slopes can usually be found at a depth of 20-30 m. In this area the hydrodynamic conditions are more geostrophic.

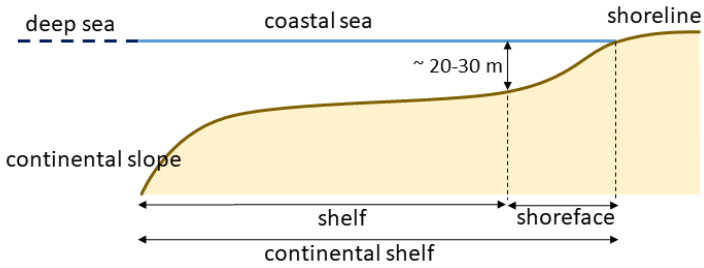

FIGURE 1.1: Coastal seas are located between the coastline and the continental slope (adapted from Masselink et al. (2014)).

Coastal seas interesting, both from an economic and ecological point of view. Many navigation routes to important ports pass through these seas, such as the route to Osaka and Kobe in the Seto Inland Sea or the route to Antwerp and Rotterdam in the North Sea. For example in figure 1.2 the amount of goods processed in European ports is indicated with the size of the circles. The blue lines across the seas and rivers correspond to the number of goods that are transported over water. It is immediately clear that the ports of Rotterdam and Antwerp are important to the European economy.

FIGURE 1.2: Amount of goods processed in ports and transported over sea (largest circle and widest blue line = 100 million tonnes per year) (Wolters-Noordhoff, 2005).

The bottom of these coastal seas displays a large variety of patterns with different spatial and temporal scales. Reineck et al. (1971) and Soulsby (1997) classified the largest bed forms as tidal sand banks and shoreface connected ridges, both characterized by distances between successive crests up to several kilometers and heights of approximately 10 m. They evolve over several centuries and they hardly migrate (order 1 m year^{-1}). Tidal sand waves have a spatial scale of several hundreds of meters forming in a couple of years, with heights up to 10 m and migration speeds of 10 m year^{-1}. An important difference between tidal sand banks, shoreface connected ridges and tidal sand waves is the orientation of their crestlines with respect to the principle tidal current. Tidal sand banks are oriented anti-clockwise with angles of 5-30 degrees (Dyer and Huntley, 1999), whereas shoreface connected ridges are oriented 20-40 degrees with respect to the coastline (Swift et al., 1978). The crests of tidal sand waves are directed perpendicular to the principal tidal current (McCave, 1971). Bedforms with wavelengths of several meters are called megaripples (distance between successive crests up to 10 m) and ripples (distances up to 1 m) by Reineck et al. (1971) and Soulsby (1997) and they have a typical timescale of days and hours, respectively. Both have waveheights on the order of centimeters and migrate several hundreds of meters per year. The crests of ripples and megaripples are oriented perpendicular to the principal tidal current. All these bedforms have been observed in the North Sea (figure 1.3) and are often superimposed on each other.

These bed forms provide a habitat for a large number of benthic species (Heip et al. (1992), Künitzer et al. (1992) and Rabaut et al. (2007)). Through tube building, burrowing activity and other forms of bio-engineering, these organisms interact with their environment to optimize their surroundings. By doing so, they mix and stir sand and interact with the North Sea morphology (Rabaut et al. (2007), Besio et al. (2008) and Borsje et al. (2009)).

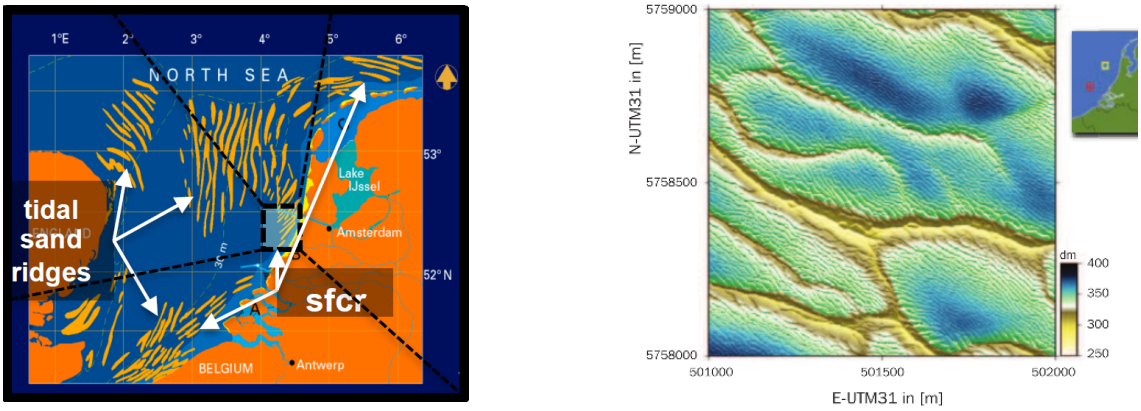

(A) (B)

FIGURE 1.3: Observations of bedforms of different spatial and temporal scales in the North Sea. **(A)** Tidal sand ridges and shoreface connected ridges (sfcr) (c. Deltares/NITG, Utrecht). **(B)** Sand waves with superimposed sand ripples, the exact location is indicated by the red square (Van Dijk et al., 2008).

This thesis focuses on tidal sand waves on the shelf of coastal seas. The interactions of sand waves with other bed forms are outside the scope of this study. Necessary conditions for sand wave formation are tidal currents with amplitudes larger than 0.5 m s^{-1}, water depths less than 50 m and a sandy bottom (Van Santen et al., 2011). Offshore tidal sand waves are observed in e.g. the North Sea (McCave, 1971), Argentina (Aliotta and Perillo, 1987), the Seto Inland Sea (Knaapen and Hulscher, 2002), the Gulf of Cadiz (Németh et al., 2007) and many other places in Canada (Duffy and Hughes-Clarke, 2005), China (Liao and Yu, 2005) and America (Barnard et al., 2006).

Tidal sand waves can be found in large parts of the North Sea, which becomes clear from figure 1.4, where the presence of sand waves is highlighted in yellow. The combination of their wave height and migration speed may cause them to interfere with human offshore activities (Nemeth et al., 2003). For example, if sand waves move into navigation channels, they reduce the water depth and thereby hamper shipping. They could also scour platforms and wind turbines. In addition to this, sand waves are at risk of exposing cables and pipelines buried in the North Sea (indicated by the red and black lines in figure 1.4), thereby endangering the electricity, oil and gas supply.

As part of the transition towards renewable energy, countries invest in the development of offshore wind farms. The Dutch government, for example, designated seven areas in the North Sea where wind farms will be built (Rijksoverheid, 2018). These areas are indicated by the red and blue polygons in figure 1.4. The red wind parks will be operational in 2023 and the blue ones in 2030, which means that many cable connections will be constructed in the coming years. To avoid cable exposure, they should be buried deep enough. However, they can not be buried too deep, because dredging is very expensive (Roetert, 2014) and cables might become overheated (Veritas, 2014). Therefore, the optimal burial depth needs to be determined before construction. So far, this has been done empirically by extrapolating trends from historical bathymetry data. This method is hindered by the lack of high resolution data and by errors in older datasets (WaterProof B.V., personal communication, June 3, 2018), resulting in large uncertainties in the trends and therefore unnecessary deep burial depths. Process-based models could improve the determination

of the burial depths. Because the typical lifetime of these cables is 50 years, the processes governing the dynamics of sand waves on the long term need to be understood. Process-based models are also key in unravelling these processes.

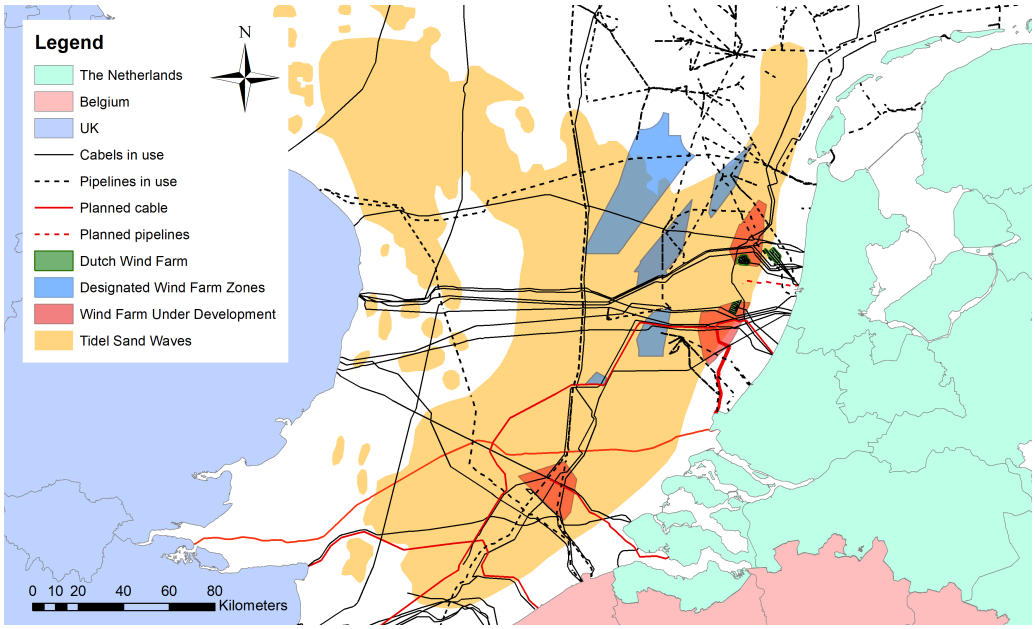

FIGURE 1.4: Map of Dutch North Sea, yellow area indicates presence of sand waves, black and red lines location of cables and pipelines and blue and red polygons future offshore wind farms (WaterProof B.V., 2018).

Sand waves form as free instabilities of the coupled bottom-water system (Hulscher et al. (1993) and Hulscher (1996)). The qualitative explanation is that the interaction of a wavy bottom perturbation with arbitrary wave length λ with an oscillating tidal flow results in residual circulation cells in the vertical plane on either side of the crest (indicated by the grey arrows in figure 1.5). The instantaneous velocity on the upstream (stoss) side of the sand wave is larger than on the downstream side (lee), because of the decrease in water depth. As sand transport increases faster than linear with the instantaneous velocity, this results in a net (i.e. tidally averaged) convergence of sand at the crest and a net divergence of sand in the troughs, causing the sand waves to grow. The slope effect causes a net transport of sand from the crest to the trough through the pull of gravity. The magnitude of this opposing effect is dependent on the bed slope. The combination of these effects determines whether a sand wave grows or decays, as for long wavelengths ($\lambda \to \infty$) the pattern of convergence and divergence is weak, so there is no growth. For small wavelengths ($\lambda \to 0$) the bed slope effect becomes dominant which limits the growth. This means that there is a certain λ for which the net sand convergence at the crest is maximum, this is called the fastest growing mode. Initially, the growth of sand waves is exponential, but as time moves on non-linear effects dampen this growth causing the sand waves to reach saturation (Van Gerwen et al., 2018, and references therein). If these residual circulation cells are asymmetric (e.g. when the flood flow is stronger than the ebb flow), the areas of convergence and divergences are shifted with respect to the trough and crest. This results in sand wave migration.

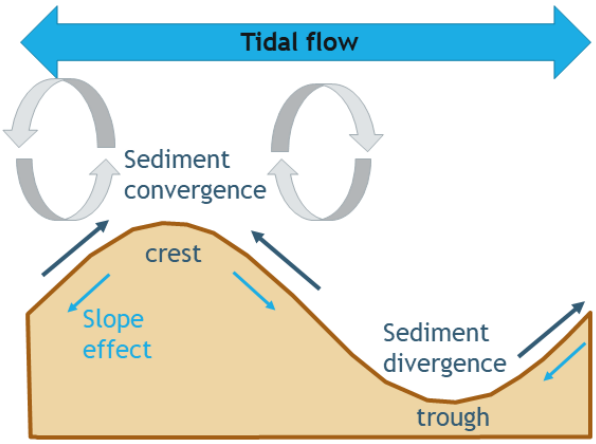

FIGURE 1.5: Interaction of oscillatory tidal flow (blue arrow) with the wavy bed causes residual circulation cells (grey arrows). Flow at the bed causes net sediment convergence at the crest (dark blue arrows), which is counteracted by the slope effect (light blue arrows).

The first quantitative, process-based models that describe the initial formation of tidal sand waves were presented by Hulscher et al. (1993), using a quasi 3D model, and by Hulscher (1996), using a full 3D model. They applied linear stability analysis to identify the fastest growing mode, by considering the wavy bottom as a superposition of a flat bed and a small sinusoidal bottom perturbation subject to tidal currents (for details of this method see e.g. Dodd et al. (2003)). If this perturbation grows positively in time, the flat bed is unstable and sand waves form. In case of a negative growth rate, the perturbations decay. These studies revealed that sand waves oriented with their crest line perpendicular to the principal tidal current grow fastest, which is in agreement with observations. Therefore in other model studies often the vertical and one horizontal direction are taken into account (2DV).

In the following years the model by Hulscher (1996) was extended with regard to the solution method (Gerkema (2000) and Besio et al. (2003)) and description of turbulence in the flow (Komarova and Hulscher (2000), Blondeaux and Vittori (2005a), Blondeaux and Vittori (2005b) and Besio et al. (2006)). The tidal forcing was updated to include a background current (Németh et al., 2002) and a superposition of multiple tidal components (Besio et al. (2003), Besio et al. (2004), Blondeaux and Vittori (2010) and Blondeaux and Vittori (2016)). The description of the sediment transport was extended by Besio et al. (2003) (bed shear stress) and Blondeaux and Vittori (2005a) and Blondeaux and Vittori (2005b) (suspended load transport). Roos et al. (2008), Van Oyen and Blondeaux (2009b) and Van Oyen and Blondeaux (2009a) included sediment with multiple grain sizes. Borsje et al. (2013) used the numerical model Delft3D to simulate the initial formation of sand waves with a complex description of turbulence. Borsje et al. (2014) extended this model to include suspended load transport. Recently, Campmans et al. (2017) studied the effect of storms on the initial formation by including both wind-waves and a wind-driven current. Overall, the range of modelled wavelengths and migration rates matches with observations. All of these studies employed linear stability analysis, which is only valid for small bottom perturbations, i.e. only for the initial stages of sand wave growth.

Non-linear effects cause the growth rate to slow down, therefore non-linear models are

needed to study the long term behaviour of sand waves. Németh et al. (2007) presented and discussed such a model. Sand waves were able to grow from a small initial perturbation to a finite height. However, the limitation of this model is that the domain was set to the wavelength of the fastest growing mode, therefore interactions between different wavelengths were not taken into account. Sterlini et al. (2009) used a non-linear model based on the work of Németh et al. (2007) to study sand wave morphology in the San Fransisco Bay. Their modelled sand wave shape agreed well with observations. However, this study did not include the time-evolution or the dynamics of these sand waves. Van den Berg et al. (2012) extended the work of Németh et al. (2007) with a different numerical solver. The goal was to make the computations more time efficient. This allowed them to study a larger domain including a range of wavelengths. Recently, the model by Borsje et al. (2013) was run for longer timescales and sand waves were able to grow from initial perturbation to an equilibrium height (Van Gerwen et al., 2018). The problem with the models of Németh et al. (2007), Van den Berg et al. (2012) and Van Gerwen et al. (2018) was that the final amplitude of the sand waves was higher than observed in the North Sea. Campmans et al. (2018) explain this difference by the fact that storm effects are not included in these models. Their study shows that both wind-driven currents and wind waves decrease the finite sand wave height.

Although the results of Van Gerwen et al. (2018) were promising, there are some limitations to this study. First of all, they indicated that the model results were very sensitive to the model settings. It is unknown to which parameters exactly and how changing these parameters affect the results. Besides this, they used this model for one water depth, sediment grain size and bed slope and only studied the effect of including a residual current. Therefore, it is unknown how sand waves evolve in a different environment on longer timescales (e.g. with a different water depth, grain size or other tidal constituents). Finally, the only initial states considered were sinusoidal sand waves with a small amplitude. In order to simulate the evolution of observed sand waves, sand waves with a finite height should be used as initial state. These three issues motivate the following research questions:

1. How sensitive are the model results, in particular crest heights and trough depths, obtained by Van Gerwen et al. (2018) to numerical parameters?

2. How sensitive are the characteristics of modelled sand waves to environmental parameters, such as water depth, tidal forcing, bed slope factor and sediment grain size?

3. How well do the model results compare to observations when a mature sand wave field is used as an initial bathymetry?

To address these research questions the state-of-the-art numerical model Delft3D (Lesser et al., 2004) is used, which is based on the model settings initially used by Van Gerwen et al. (2018). To answer the first research question, a default case is defined which was used as reference case. Then a series of runs is performed, where in each run one of the numerical parameters (time step, grid size and morphological acceleration factor) was changed. The sand waves are allowed to grow from a small perturbation to a finite height. The results for the different setting are compared to those of the reference case. Next, a

series of runs is performed, where one of the environmental parameters (water depth, tidal forcing, bed slope and sediment grain size) is changed at the time. Two types of runs are performed: long runs from initial perturbation to finite height and small runs allowing to study the initial growth rates using linear stability analysis. All output is compared to the new reference case. The last research question is addressed by using an observed sand wave field as model input and comparing the characteristics of the modelled sand waves (in particular crest heights, trough depths, shapes and migration speeds) with those of the observed sand waves.

In chapter 2 the theory behind sand transport will be discussed and the dynamics of sand waves will be explained in more detail. Chapter 3 discusses the Delft3D model. Chapter 4 describes the model set up in each of the experiments, the data that are used and how the model outputs are analysed. The results of this analysis are presented in chapter 5 and will be discussed in chapter 6. Recommendations for future research and conclusions are given in chapter 7.

Chapter 2

Theoretical concepts

2.1 Sand transport and bed evolution

Sand waves grow, decay and migrate, depending on the magnitude and direction of the net sand transport. Therefore it is important to take a closer look into the mechanisms governing sand transport. In short, the movement of a current over the bed generates bed shear stress. If this bed shear stress is larger than a critical value, sand is made available for transportation and is then transported by the current. If there are spatial divergences in this transport, the bed will change. This alters the flow because of changes in the water depth, thereby affecting the sand transport again.

Sand transport can also be the result of bed shear stress caused by waves, but in this study only the effect of currents is taken into account (for generalisation to waves and currents see Campmans et al. (2017)). How much sand is transported, depends on the properties of the sand grains. So these will be discussed first. Then the threshold for motion and the different transport modes will be described.

2.1.1 Sand properties

Sand particles have grain sizes d varying from 0.06 mm to 2 mm and consist of quartz, which has density $\rho_s = 2650$ kg m^{-3} (Soulsby, 1997). Natural sands consist of a range of grain sizes that can be identified through sieving. Often the resulting grain sizes are plotted in a cumulative curve, where the percentage on the y-axis corresponds to the part of the sample that is finer than the grain size on the x-axis. An example of such a curve is shown in figure 2.1. In this sample $d_{10} = 0.23$ mm, $d_{50} = 0.59$ mm and $d_{90} = 1.15$ mm and they are indicated by the black lines. These three grain sizes are often used in sand transport calculations, especially the median grain size d_{50} as this is the grain size for which 50% of the sample is smaller and 50% of the sample is larger.

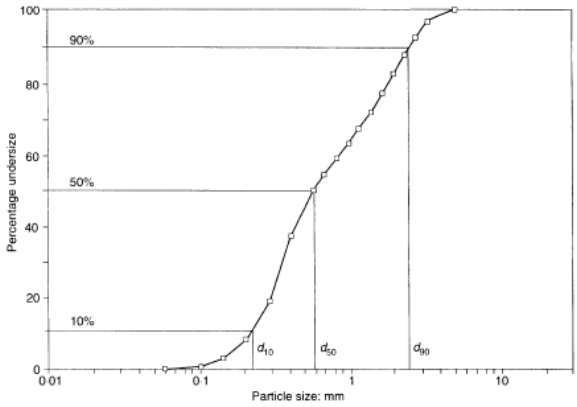

FIGURE 2.1: Example of cumulative curve of sand grain sizes (Soulsby, 1997).

The porosity of the bed ϵ indicates how much air- or water filled space there is between the sand particles as a fraction of the total volume occupied by the sand particles (Soulsby, 1997). This depends on the shape of the particles and on how closely they are packed, but is around 0.4 for natural sand beds.

The angle of repose ϕ is the angle at which sediment starts to avalanche with zero flow (Soulsby, 1997). The magnitude of this angle depends on the shape, sorting and packing and is approximately 32° for natural sands in water.

2.1.2 Settling velocity

The settling velocity w_s is the velocity with which particles in suspension sink to the bottom in motionless water (Deigaard and Fredsœ, 1992). This velocity is determined by the balance between the forces acting on the particle. The first is the drag force on the particle F_D,

$$F_D = \frac{1}{2}\rho C_D \frac{\pi}{4} d^2 w_s^2. \tag{2.1}$$

Here, ρ is the water density and C_D the drag coefficient. The drag coefficient depends on the Reynolds number Re, which describes the ratio of the inertial forces to the viscous forces in the fluid, i.e. whether the flow is turbulent ($Re \gg 1$) or laminar ($Re \ll 1$),

$$Re = \frac{w_s d}{\nu}. \tag{2.2}$$

In this equation ν is the kinematic viscosity of water, which has a value of 10^{-6} m^{2}s^{-1}. The force F_D is balanced by the gravitational force F_G,

$$F_G = (\rho_s - \rho)\frac{\pi}{6} d^3. \tag{2.3}$$

The force balance results in an equation for the settling velocity,

$$w_s = \sqrt{\frac{4(\rho_s/\rho - 1)gd}{3C_D}}. \tag{2.4}$$

So w_s increases for larger grain sizes and larger values of the drag coefficient.

2.1.3 Threshold for sand motion

There are three forces working on a sand particle at the bed (Dyer, 1986), these are shown in figure 2.2. The first two are driving forces: a drag force F_D in the direction of the current and a lift force F_L in the vertical direction. Both result from the friction and pressure differences along the particle surface, because the flow is slightly deflected when moving over a particle. The third force is the stabilizing gravitational force F_G, also called the weight of the submerged particle.

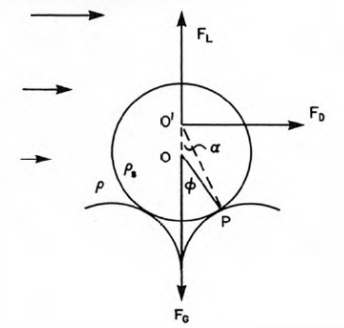

FIGURE 2.2: Forces working on sediment particles (Dyer, 1986).

The point P is the contact point between the particle and the bed, O is the centre of the particle, O' is the point where F_L and F_D work on the particle and ϕ is the angle of repose. If the sum of the forces F_D, F_L and F_G results in a net force perpendicular to the line OP, the particle will move. The force balance is

$$F_D \cos\alpha = (F_G - F_L)\sin\alpha. \tag{2.5}$$

Here α is the angle between the line $O'P$ and the vertical. The drag force F_D reads

$$F_D = \frac{1}{2}\rho C_D \frac{\pi}{4} d^2 (u_b)^2. \tag{2.6}$$

In this equation d is the particle grain size and u_b is the velocity at the bed. The lift force F_L can be expressed in a similar way:

$$F_L = \frac{1}{2}\rho C_L \frac{\pi}{4} d^2 (u_b)^2, \tag{2.7}$$

where C_L is the lift coefficient. The two driving forces can be combined into the total driving force $F_{driving}$: (Deigaard and Fredsœ, 1992)

$$F_{driving} = \frac{1}{2}\rho c_d \frac{\pi}{4} d^2 (\alpha_b u_*)^2. \tag{2.8}$$

Now c_d includes both the drag and lift coefficient and u_* is the friction velocity. The parameter α_b indicates that u_* is close to the bed. The stabilizing force F_G is defined in equation 2.3. Substituting equations 2.8 and 2.3 into the force balance (equation 2.5), results in an expression for the critical friction velocity u_{*c},

$$u_{*c} = \sqrt{\frac{4\tan\phi}{3 c_d \alpha_b}(\rho_s/\rho - 1) g d}. \tag{2.9}$$

If the $u_* > u_{*c}$, sand particles will start to move. The magnitude of u_{*c} depends on the grain size of the particle. The friction velocity is related to the bed shear stress τ_b,

$$\tau_b = \rho u_*^2 \quad \text{with } u_* \propto u_b, \tag{2.10}$$

where u_b is the velocity at the bed which is proportional to u_*. Therefore, the threshold for sand motion can also be expressed in terms of the bed shear stress: $\tau_b > \tau_{b,cr}$. Shields (1936) derived the threshold parameter θ_{cr0} from equation 2.9 (also called Shields parameter), which is the ratio of the critical bed shear stress $\tau_{b,cr}$ and the submerged weight of the particle:

$$\theta_{cr0} = \frac{\tau_{b,cr}}{(\rho_s - \rho)gd}. \tag{2.11}$$

The Shields parameter θ_{cr0} is a function of the particle Reynolds number Re_*. This is the ratio of particle grain size and the viscous boundary layer width,

$$Re_* = \frac{u_{*c}d}{\nu}. \tag{2.12}$$

For $Re_* < 5$ the grain size is smaller than the width of the viscous boundary layer, so the critical bed shear stress is independent of the grain size. For large values of the particle Reynolds number ($Re_* > 200$) θ_{cr0} has a constant value of approximately 0.05 (figure 2.3).

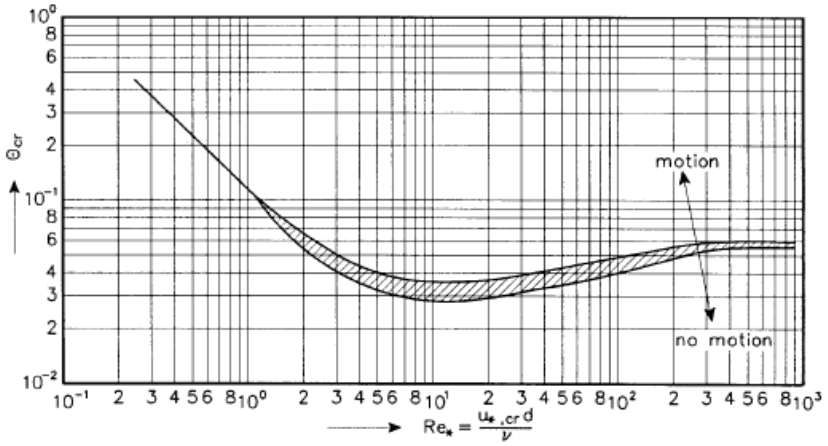

FIGURE 2.3: Shields curve relating Shields parameter θ_{cr0} to particle Reynolds number Re_* (source: Van Rijn (1993)).

So far, it has been assumed that the particles are on a flat bed. In reality the bed is often sloped. So now consider the case where the sand particle is on a bed with angle β in the direction of the flow (see figure 2.4). In this case the force balance is

$$(F_D - F_G \sin\beta)\cos\alpha = (F_G \cos\beta - F_L)\sin\alpha. \tag{2.13}$$

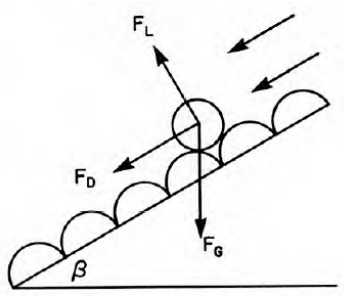

FIGURE 2.4: Force balance for grains under angle β in the direction of the flow (source: Dyer (1986)).

Following the same procedure as previously described, the Shields parameter becomes (Van Rijn, 1993)

$$\theta_{cr}(\beta) = \theta_{cr0}\left(1 + \frac{\tan\beta}{\tan\alpha}\right)\cos\beta. \tag{2.14}$$

If $\tan\beta$ is positive and the flow moves up-slope, the value of the critical bed shear stress increases. If the opposite happens and the flow moves down-slope, $\tan\beta$ becomes negative and the critical bed shear stress decreases. The result is that sand moves more easily down the slope than up the slope.

2.1.4 Sand transport modes

After sand is brought into motion, because the bed shear stress is larger than its critical value, it can be transported in to ways: as bed load transport and as suspended load transport. In bed load transport sediment particles slide or roll on the bottom, also saltating or hopping particles are counted as bed load transport as long as they stay close to the bed (Van Rijn, 1993). In suspended transport the particles are in suspension in the water column.

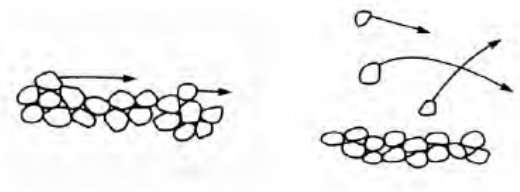

FIGURE 2.5: Modes of sediment transport, left: bed load transport, right: suspended load transport (source: Deigaard and Fredsœ (1992)).

Bed load transport takes place in a thin layer close to the bed where the effect of turbulence is so small that it does not affect the sediment particles. Therefore it is almost fully determined by the excess bed shear stress, yielding

$$\overrightarrow{q_b} = \delta_b c_b \overrightarrow{u_b} = \hat{\mathrm{q}}\left(\frac{\tau_b - \tau_{b,cr}}{\tau_{b,cr}}\right)^a \left[\frac{\overrightarrow{\tau}_{b,cr}}{\tau_{b,cr}} - \lambda_s \bigtriangledown z_b\right]. \tag{2.15}$$

Here δ_b is the thickness of the layer where bed load transport takes place, c_b the sediment concentration (the volume of sediment per volume of water), u_b the velocity in this layer and $\hat{q}$ the bed load coefficient. The coefficient a depends on sand properties and flow conditions and is usually a value between 1.5 and 3 (Van Rijn, 1993). The parameter z_b is the bed level and λ_s the slope parameter, which is related to the angle of repose ϕ,

$$\lambda_s = \frac{1}{\tan \phi}. \tag{2.16}$$

This slope parameter ensures that the bed slope does not become steeper than the angle of repose. Since the value of $\tau_{b,cr}$ depends on the local bed slope (equations 2.11 and 2.14), sand is transported more easily downhill than uphill.

The layer δ_b ends at reference height a where turbulent mixing becomes important. Sediment is lifted if the shear velocity u_* is larger than the sediment settling velocity w_s. If then the turbulent forces at this height are the same or larger than the submerged weight, the particle stays in suspension (Van Rijn, 1993). These particles move approximately with the same speed as the flow. Since suspended transport takes place in a large part of the water column, the transport is given by,

$$\overrightarrow{q_s} = \int_{(z_b+a)}^{z_s} \overrightarrow{u}(z) c(z)\, dz. \tag{2.17}$$

Where z_b indicates the location of the bed, z_s the top of the water column and c the volumetric concentration of suspended sand.

2.1.5 Bed evolution

Once the magnitude and direction of the bed load transport and suspended load transport are known, the resulting changes in the bed level can be calculated using the sediment budget equation (Soulsby, 1997),

$$(1-\epsilon)\frac{\partial z_b}{\partial t} + \overrightarrow{\nabla} \cdot (\overrightarrow{q_b} + \overrightarrow{q_s}) = 0. \tag{2.18}$$

This equation states that the bed level z_b will change in time depending on the divergence of the total volumetric sand transport, i.e. the volume of the pores is excluded by taking into account bed porosity ϵ. So, if there is a convergence of sand at one location, the bed will go up and in case of sand divergence, the bed level goes down.

2.2 Sand wave dynamics

2.2.1 Sand wave formation

The formation of sand waves as a free instability of the coupled bottom-water system can be understood assuming small bottom perturbations. The hydrodynamics can be analysed in an analogous manner as done by Zimmerman (1981), except that flow structures form in the vertical plane rather than in the horizontal plane (due to headland eddies).

As the tidal current flows over a bottom perturbation, flow is accelerated moving up the slope and decelerated moving down the slope. At the same time a frictional boundary layer develops, in which the velocity decreases towards zero at the bed, which results in vorticity production. First consider the flood phase, when the velocity is directed towards the right in figure 2.6 (the red arrows correspond to the flood phase). In this case clockwise vorticity is produced on the upstream side (and anticlockwise vorticity on the downstream side). Since the velocity is largest at the crest, there is more vorticity production at this location. The clockwise vorticity is transported towards the right by the tidal current. This results in a convergence of clockwise vorticity to the right of the perturbation and a divergence of clockwise vorticity to the left, which is equivalent to a build up of anticlockwise vorticity.

During the ebb phase (blue arrows in figure 2.6) the velocity is directed into the opposite direction, but the vorticity flux stays the same. There is now a production of anticlockwise vorticity which is advected to the left. So there is convergence of anticlockwise vorticity at the left and a divergence at the right. This is equivalent to the situation during flood, so there is again a build up of anticlockwise vorticity at the left and a build up of clockwise vorticity at the right of the perturbation. Since averaged over a tidal cycle there is a net build up of vorticity with opposite signs, this results in residual circulation cells in the flow with opposite signs. These cells are shown by the black lines and arrows in figure 2.6.

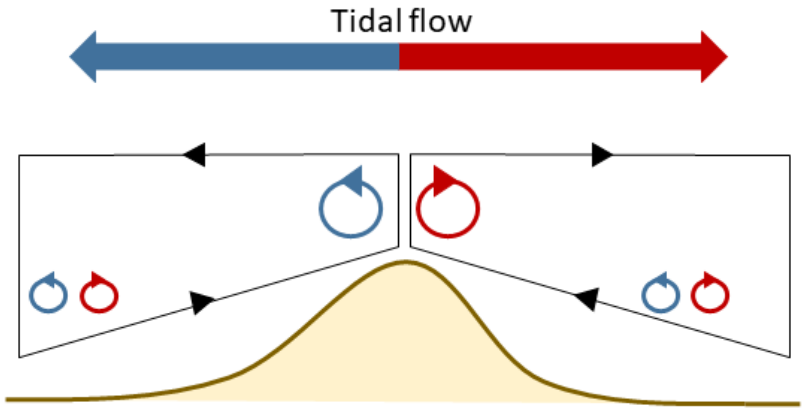

FIGURE 2.6: Interaction of tidal flow over a wavy bottom generates vorticity, where the red arrows correspond to the flood phase associated with clockwise vorticity and the blue arrows to the ebb phase (anticlockwise vorticity). The black lines and arrows show the resulting residual circulation cells (adapted from Zimmerman (1981)).

As stated before the flow is accelerated up-slope and decelerated down slope both in the flood and ebb phase. Since the bed load transport is related non-linearly to the instantaneous velocity at the bed (equation 2.15), this results in a larger sand transport up the crest than down the crest in both phases. Therefore, there is a net convergence of sand at the crest and a net divergence of sand in the troughs. This is the positive feedback causing growth of the sand waves.

2.2.2 Scale selection

Equations 2.14 and 2.15 show that sand transport is related to the bed slope β in such a way that sand is transported more easily down-slope than up-slope. This balances the positive feedback mechanism that causes sand waves growth. The strength of the growth and decay mechanisms depends on the wave length λ. If sand waves have large wave lengths ($\lambda \to \infty$ so $\beta \to 0$), the pattern of convergence and divergence of sediment becomes weak, as spatial differences in sand transport are small. So the growth mechanism is weak. However, for small wave lengths ($\lambda \to 0$), the bed slope becomes high ($\beta \to \infty$) just as the critical bed shear stress τ_{bc} that needs to exceeded. In other words, it is difficult to move sand up the crest and the decaying bed slope effect is strong. In both situations sand waves are not able to grow. Somewhere in between these extremes there is a value of λ for which the net convergence of sand at the crest is maximum. This mode is called the fastest growing mode (λ_{FGM}) and this mode often dominates in natural sand wave fields (Hulscher, 1996). The value of λ_{FGM} depends on the water depth, sand grain size, tidal current amplitude, tidal ellipticity and the presence of wind and waves (Besio et al. (2006), Van Oyen and Blondeaux (2009a), Blondeaux and Vittori (2011), Van Santen et al. (2011), Borsje et al. (2013) and Campmans et al. (2017)).

2.2.3 The effect of suspended load transport on sand wave formation

In the discussion of sand transport two transport modes were considered: bed load transport and suspended load transport. The growth and decay mechanisms discussed in the previous sections have considered bed load transport only. Suspended load transport has a damping effect on the growth of sand waves (Blondeaux and Vittori (2005a), Blondeaux and Vittori (2005b),Besio et al. (2006), Van Oyen and Blondeaux (2009b), Borsje et al. (2014) and Campmans et al. (2017)) if their wavelengths become short. The amount of sand transported in suspension depends on the suspended sand concentration and the velocity (equation 2.17). Both in the flood and ebb phase the concentration is higher down-slope of the crest than up-slope of the crest. The velocity shows the opposite pattern: it is higher up-slope than down-slope. This results in a net divergence of suspended sand at the crest and a net convergence in the trough and therefore a damping of the sand wave growth. This explains why natural sand wave fields are only observed in areas that are dominated by bed load transport. The suspended sand concentration depends strongly on the grain size, as smaller particles stay in suspension more easily, so the damping effect is stronger for smaller grain sizes. However, this mechanism is only the case for sand waves that are sufficiently small. The suspended load transport can add positively to the growth of sand waves for larger sand wave lengths (Campmans et al., 2017).

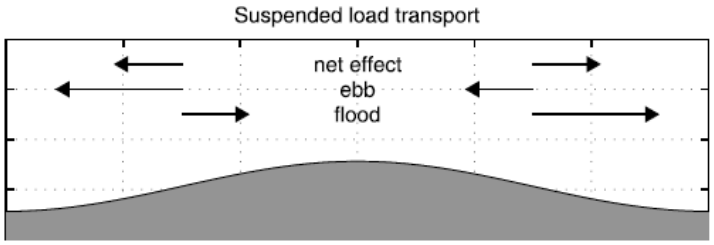

FIGURE 2.7: For sand waves that are sufficiently small, there is a net divergence of suspended sediment at the crest and a net convergence in the trough, this dampens the sand wave growth (source: Borsje et al. (2014)).

2.2.4 Sand wave migration

A symmetrical tidal forcing means that the peak ebb current is equal to the peak flood current, i.e. both the peak velocities and the duration of both phases are the same. Therefore, there will be no net bed load transport $\langle q_b \rangle = 0$, as long as the bed level z_b = constant. This is not true for the net suspended load transport due to settling lag effects (Groen, 1967). In the case of sand waves, this means that the residual circulation cells are symmetrical in shape, causing the areas of convergence and divergence to be exactly at the crests and troughs.

The tidal forcing can be asymmetrical in two ways: 1) either the peak flood amplitude or the flood duration is different from the peak ebb amplitude or duration; and 2) the duration of the transition from ebb to flood is different from the duration of the transition from flood to ebb. Both types cause the areas of sand convergence and divergence to be out of phase with the bed perturbation, resulting in sand wave migration. Tidal asymmetry can be caused by the presence of overtides or a residual current. For example, in the North Sea M_2 with a period of 12.41 hours is the dominant tidal constituent (Van de Kreeke and Robaczewska, 1993). In case both M_2 and its first overtide M_4 are present, the velocity can be written as

$$u(t) = A_{M2} \cos \omega t + A_{M4} \cos(2\omega t - \theta). \tag{2.19}$$

Here, A_{M2} is the amplitude of M_2 and ω is the angular frequency corresponding to the M_2 tide. The amplitude of M_4 is given by A_{M4} and θ is the phase difference between M_2 and M_4. In figure 2.8 the M_2 and M_4 velocity are shown with the solid and dashed lines, respectively. In all four panels, both are symmetrical and result in $\langle q_b \rangle = 0$ (as long as z_b is constant). The dotted lines in this figure correspond to the total velocity resulting from the interaction of M_2 and M_4 for four different values of θ. In each case, the velocity has become asymmetrical, the two left panels ($\theta = 0$ and $\theta = \pi$) show type 1 asymmetry and the two right panels ($\theta = \frac{\pi}{2}$ and $\theta = \frac{3\pi}{2}$) show asymmetry of type 2. Therefore, there will be net sand transport ($\langle q_b \rangle \neq 0$) in all four cases.

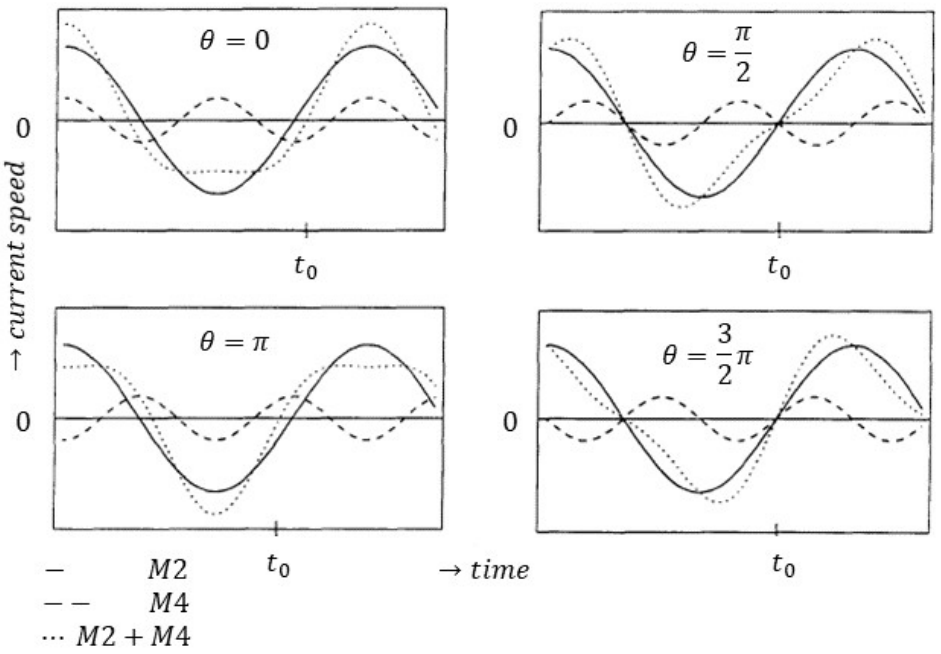

FIGURE 2.8: The M_2 velocity (solid lines), M_4 velocity (dashed lines) and the superposition of the two (total velocity, dotted lines) over time, for four cases of phase difference θ (adapted from Van de Kreeke and Robaczewska (1993)).

Chapter 3

Modelling tidal sand waves

In this chapter the model used in the present study will be described. It is based on the numerical model Delft3D-FLOW (Lesser et al., 2004) with the settings initially used by Van Gerwen et al. (2018). This model solves the two-dimensional vertical shallow water equations and the result is used to calculate the sand transport. This in turn determines how the bed changes through the sediment continuity equation. Figure 3.1 provides an overview of the model structure.

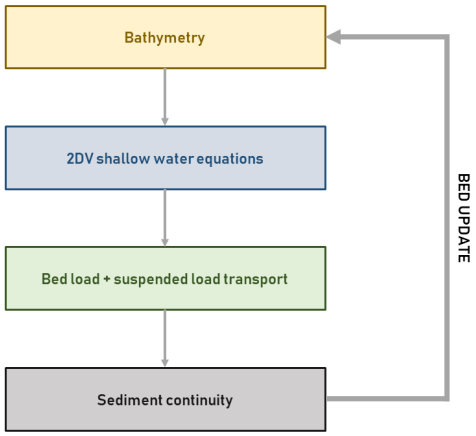

FIGURE 3.1: Overview of the model structure.

3.1 Domain

The model simulates the tidal flow, sand transport and bed evolution in two directions. As a first approximation, the crests are oriented perpendicular to the direction of the principle tidal current, which corresponds to observations (Wilson and Stride (1982) and Lankneus and Moor (1991)). Therefore, the x-direction is oriented perpendicular to the sand wave crests and the z-axis points in the vertical direction. In the y-direction the flow is zero and variations are assumed to be uniform. The domain of the model is sized L_x along the horizontal axis (figure 3.2). The lateral boundaries (at $x = 0$ and $x = L_x$) are open so tidal waves can pass through the domain. The undisturbed water level is denoted by H_0, so the undisturbed bed level is $z = -H_0$. The water level below reference level

$z = 0$ is $H(x,t)$ and this includes the perturbation of the bed $h(x,t)$ with respect to H_0. The total water depth D (x,t) includes both $H(x,t)$ and the free surface elevation $\zeta(x,t)$ with respect to $z = 0$. The bed level is found at $z = z_b$ and the free surface at $z = z_s$. The model solves the 2DV shallow water equations in $(x,\ y,\ \sigma)$-coordinates, where

$$\sigma = \frac{z-\zeta}{H+\zeta} = \frac{z-\zeta}{D}. \tag{3.1}$$

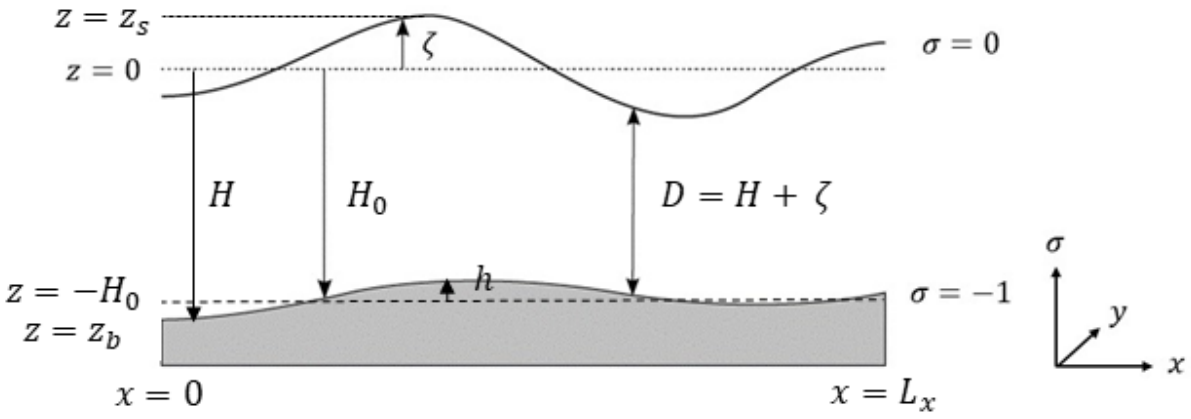

FIGURE 3.2: Schematic view of study area. For explanation of symbols see the text.

3.2 Hydrodynamics

The 2DV shallow water equations in (x,σ)-coordinates are

$$\frac{\partial u}{\partial t} + u\frac{\partial u}{\partial x} + \frac{\omega}{(H+\zeta)}\frac{\partial u}{\partial \sigma} = -\frac{1}{g}\frac{\partial \zeta}{\partial x} + \frac{\partial}{\partial x}\left(\nu_H\left(\frac{\partial u}{\partial x} + \frac{\partial u}{\partial \sigma}\frac{\partial \sigma}{\partial x}\right) + \frac{1}{(H+\zeta)^2}\frac{\partial}{\partial \sigma}\left(\nu_V\frac{\partial u}{\partial \sigma}\right)\right), \tag{3.2}$$

$$\frac{\partial \omega}{\partial \sigma} = -\frac{\partial \zeta}{\partial t} - \frac{\partial[(H+\zeta)u]}{\partial x}. \tag{3.3}$$

In these equations u is the horizontal velocity and ω the vertical velocity $((H\ +\ \zeta)\ \frac{D\ \sigma}{D\ t})$, where $\frac{D}{Dt}$ is the material derivative. The water density ρ_w is assumed to be constant and g is the gravitational acceleration. Furthermore, ν_H and ν_V represent the horizontal and vertical eddy viscosity, respectively. The Coriolis effect is not included in the 2DV shallow water equations.

3.3 Boundary conditions

3.3.1 Vertical boundaries

The bed (σ = -1) and the free surface ($\sigma = 0$) are assumed to be impermeable, therefore the vertical velocity is set to zero,

$$\text{at } \sigma = -1: \qquad \omega = 0, \tag{3.4}$$

$$\text{at } \sigma = 0: \qquad \omega = 0. \tag{3.5}$$

The stress at the bed is given by a quadratic friction law, while the stress at the free surface is set to zero:

$$\text{at } \sigma = -1: \qquad \tau_b = \rho_w \frac{\nu_V}{(H+\zeta)} \frac{\partial u}{\partial \sigma} = \rho_w u_* |u_*| = \rho_w c_b |u_b| u_b, \tag{3.6}$$

$$\text{at } \sigma = 0: \qquad \rho_w \frac{\nu_V}{(H+\zeta)} \frac{\partial u}{\partial \sigma} = 0. \tag{3.7}$$

In these equations ρ_w is the water density, τ_b is the bed shear stress, ν_V the vertical eddy viscosity coefficient and u_b is the velocity close to the bed

$$u_b = u(\sigma = -1 + \delta). \tag{3.8}$$

The value of δ can be chosen freely, but in this layered σ-model is is chosen as $\frac{1}{2}\Delta\sigma$, i.e. the distance between the middle of the lowest σ-layer to the bed. The vertical structure of the flow near the bed is given by a logarithmic profile

$$u = \frac{u_*}{\kappa} \ln\left(\frac{\sigma + 1}{\sigma_0}\right). \tag{3.9}$$

Here, κ is the Von Kármán constant (0.41). Combining equations 3.6 and 3.9 results in a definition of friction velocity u_*

$$u_*^2 = c_b \left[\frac{u_*}{\kappa} \ln\left(\frac{\delta}{\sigma_0}\right)\right]^2. \tag{3.10}$$

From this definition, the drag coefficient at the bed c_b can be determined:

$$c_b = \left[\frac{\kappa}{\ln(\delta/\sigma_0)}\right]^2. \tag{3.11}$$

The roughness height in σ-coordinates is σ_0, which is related through the local roughness height z_0,

$$z_0 = \zeta + D\sigma_0. \tag{3.12}$$

This local roughness height is related to the actual geometric roughness height k_s which is user-defined and set to 0.01 m,

$$z_0 = \frac{k_s}{30}. \tag{3.13}$$

Van Gerwen et al. (2018) chose the k-ϵ model as a closure model for the vertical eddy viscosity coefficient . Here k is the turbulent kinetic energy and ϵ the dissipation rate of k. A detailed description of this model can be found in Burchard et al. (2008). Both turbulent kinetic energy k and turbulent energy dissipation ϵ are calculated for every point in space and time and used to calculate the vertical eddy viscosity,

$$\nu_V = c_\mu \frac{k^2}{\epsilon}. \tag{3.14}$$

In this equation c_μ is an empirical constant set to 0.09 after Rodi (1984). The horizontal eddy viscosity v_H is assumed to be a superposition of an user-defined background eddy viscosity ν_{back} and the vertical eddy viscosity, such that $\nu_{back} \gg \nu_V$ (Deltares, 2013)

$$\nu_H = \nu_{back} + \nu_V. \tag{3.15}$$

3.3.2 Horizontal boundaries

At the lateral boundaries ($x = 0$ and $x = L_x$) the flow can be forced in several ways. Van Gerwen et al. (2018) chose the Riemann boundary condition, which is combination of water level ζ and a depth averaged flow U. This condition is weakly reflective and allows the tidal wave to pass through the boundaries (Deltares, 2013). In the vertical direction the velocity profile is assumed to be logarithmic.

3.4 Sand transport

Using the output of the hydrodynamic module, the sand transport is calculated using the equations by Van Rijn (1993), which is the default mode of Delft3D-FLOW. The sediment continuity equation describes how the bed changes as a result of convergence or divergence of sediment at each location,

$$(1 - \epsilon_p)\frac{\partial z_b}{\partial t} + \frac{\partial (q_b + q_s)}{\partial x} = 0. \tag{3.16}$$

In this equation, ϵ_p is the bed porosity and set to 0.4, and q_b is the magnitude of the bed load transport,

$$q_b = 0.5 \rho_s d_{50} u'_* T D_*^{-0.3}, \tag{3.17}$$

with ρ_s is the density of the sediment, d_{50} the median sediment grain size and T is the non-dimensional bed shear stress

$$T = \frac{\mu_c \tau_b - \tau_{b,cr}}{\tau_{b,cr}}. \tag{3.18}$$

Here, $\tau_{b,cr}$ is the critical bed shear stress for initiation of motion

$$\tau_{b,cr} = (\rho_s - \rho_w) g d_{50} \theta_{cr} \tag{3.19}$$

In this equation θ_{cr} is the Shields parameter, parametrized as

$$\theta_{cr} = 0.04 D_*^{-0.1}, \tag{3.20}$$

which in turn depends on the non-dimensional grain size D_*

$$D_* = d_{50}\left(\frac{\rho_s - \rho_w}{\nu^2}\right)^{1/3}, \tag{3.21}$$

with ν is the kinematic viscosity of water. The friction velocity due to currents u'_* is given by

$$u'_* = u_* \mu_c, \tag{3.22}$$

where coefficient μ_c takes into account that sediment transport is only due to part of the total bed stress, i.e. only the result of skin friction and not of form drag (Soulsby, 1997).

$$\mu_c = \frac{f'_c}{f_c}. \tag{3.23}$$

This coefficient is the ration of the grain-related friction factor f'_c

$$f'_c = 0.24\left[\log_{10}\left(\frac{12(H+\zeta)}{3d_{90}}\right)\right]^{-2}, \tag{3.24}$$

and the current-related friction factor f_c

$$f_c = 0.24\left[\log_{10}\left(\frac{12(H+\zeta)}{z_0}\right)\right]^{-2}. \tag{3.25}$$

The magnitude of the suspended load transport is given by the following equation:

$$q_s = \int_{-1+a/(H+\zeta)}^{0}\left(uc - \epsilon_{s,z}\frac{\partial c}{\partial x}\right)d\sigma \tag{3.26}$$

Here a is a reference height of $0.01H$, since sediment below this level reacts almost instantaneously to changes in the flow and is therefore considered part of the bed load. The sediment above this height is transported in suspension.

The advection-diffusion (mass-balance) for suspended sediment concentration c is given by,

$$\begin{aligned}\frac{\partial(H+\zeta)c}{\partial t} + \frac{\partial[(H+\zeta)cu]}{\partial x} + \frac{\partial(\omega - w_s)c}{\partial\sigma} &= (H+\zeta)\frac{\partial}{\partial x}\left(\epsilon_{s,x}\frac{\partial c}{\partial x}\right) \\ &+ \frac{\partial}{\partial\sigma}\left(\epsilon_{s,z}\frac{1}{(H+\zeta)}\frac{\partial c}{\partial\sigma}\right).\end{aligned} \tag{3.27}$$

At the free surface ($\sigma = 0$), c is assumed to be zero and at reference height a, the concentration is equal to reference concentration c_a

$$\text{at } \sigma = a: \qquad c = c_a = 0.015\rho_s \frac{d_{50}T^{1.5}}{aD_*^{0.3}}, \tag{3.28}$$

$$\text{at } \sigma = 0: \qquad -w_s c - \epsilon_{s,z}\frac{1}{(H+\zeta)}\frac{\partial c}{\partial\sigma} = 0. \tag{3.29}$$

In these equations $\epsilon_{s,z}$ is the vertical eddy diffusivity, which depends on the vertical eddy viscosity ν_V,

$$\epsilon_{s,z} = \frac{\nu_V}{\sigma_c}. \tag{3.30}$$

Here, σ_c is the Prandtl-Schmidt number, which is 1 in the case of the k-ϵ turbulence model (Deltares, 2013). The horizontal eddy diffusivity $\epsilon_{s,x}$ is a superposition of the vertical eddy diffusivity and an user-defined background diffusivity such that $\epsilon_{back} \gg \epsilon_{s,z}$,

$$\epsilon_{s,x} = \epsilon_{s,z} + \epsilon_{back}. \tag{3.31}$$

The settling velocity w_s depends on the representative suspended sediment grain size D_s

$$0.065\,\text{mm} < D_s \leq 0.1\,\text{mm} \quad w_s = \frac{(\rho_s/\rho_w - 1)gD_s^2}{18\nu} \tag{3.32}$$

$$0.1\,\text{mm} < D_s \leq 1\,\text{mm} \quad w_s = \frac{18\nu}{D_s}\left(\sqrt{1 + \frac{0.01(\rho_s/\rho_w - 1)gD_s^3}{\nu^2}} - 1\right) \tag{3.33}$$

$$D_s > 1\,\text{mm} \quad w_s = 1.1\sqrt{(\rho_s/\rho_w - 1)gD_s}. \tag{3.34}$$

In this equation ν is the kinematic viscosity of water and D_s is calculated based on the magnitude of the non-dimensional bed shear stress T, i.e.

$$T \leq 1 \quad D_s = 0.64d_{50} \tag{3.35}$$

$$1 < T \leq 25 \quad D_s = d_{50}(1 + 0.015(T - 25)) \tag{3.36}$$

$$T > 25 \quad D_s = d_{50}. \tag{3.37}$$

3.5 Numerical aspects

Delft3D solves the equations on a curvilinear, staggered grid. Along the vertical axis sigma layering is applied (Deltares (2013)), this means that the number of vertical layers stays constant regardless of the water depth. The time integration of the shallow-water equations is based on the Alternating Direction Implicit (ADI) method. The advection terms are discretized using the Cyclic method. This method is also used to solve the advection-diffusion equation (for explanation of these methods see Deltares (2013)).

A challenge in morphological modeling is that bed level changes occur on much larger time scales than the time scales associated with the hydrodynamical part of the model (Ranasinghe et al., 2011). To deal with this, Delft3D-FLOW provides the option to implement a morphological acceleration factor (MORFAC). After each time step the bed level changes are multiplied with this factor to scale them up to the level of hydrodynamic changes. This reduces the computation time significantly, but also introduces errors.

Chapter 4

Methodology

In this chapter, first the default model settings and the experiments performed to answer the three research questions will be discussed. In the last section the methods to analyse the results are presented.

4.1 Default model settings

In the default mode the horizontal domain L_x is 50 km long and the undisturbed water depth H_0 is 25 m. The undisturbed bed is perturbed with a sinusoidal function in the middle 5 km (from $x = 22.5$ km to $x = 27.5$ km) of the domain,

$$z_b = H_0 - \eta A_0 \cos\left(2\pi \frac{x - x_{mid}}{\lambda_0}\right). \tag{4.1}$$

In this equation z_b is the bed level, H_0 the undisturbed water depth, A_0 the initial sand wave amplitude, λ_0 the initial wavelength and x_{mid} the coordinate in the middle of the domain ($x_{mid} = 25$ km). The factor η represents an envelope function which depends on the location in the horizontal domain:

$$\begin{aligned}
\text{at } 0 \leq x < 22.5 \text{ km} &: \eta = 0, \\
\text{at } 22.5 \leq x < 23.5 \text{ km} &: \eta = \frac{1}{2}\left[1 - \cos\big(\pi(x - x_{mid})\right], \\
\text{at } 23.5 \leq x < 26.5 \text{ km} &: \eta = 1, \\
\text{at } 26.5 \leq x < 27.5 \text{ km} &: \eta = \frac{1}{2}\left[1 + \cos\big(\pi(x - x_{mid})\right], \\
\text{at } 27.5 \leq x \leq 50 \text{ km} &: \eta = 0.
\end{aligned}$$

This envelope function is included to provide a smooth and gradual transition from the flat bed at the boundaries to the perturbed bed in the middle of the domain. The distance between the boundaries and the area of interest prevents the flow from being influenced by boundary effects. The initial amplitude $A_0 = 0.25$ m and the wavelength $\lambda_0 = 204$ m. The latter is the fastest growing mode under these conditions (Van Gerwen et al., 2018),

and this initial wavelength is kept constant for all simulations. The perturbed part of the bed is shown in figure 4.1.

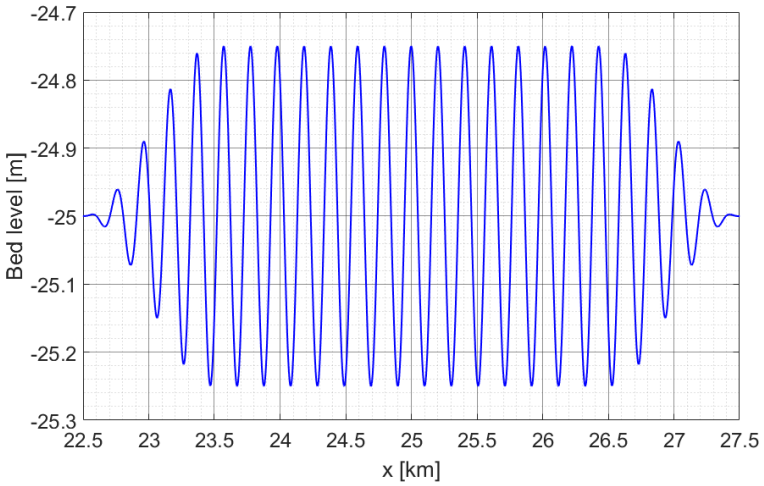

FIGURE 4.1: The initial bed perturbation ($h(t = 0)$) in the default configuration.

Both the horizontal and vertical grid spacing vary (figure 4.2). At the boundaries the horizontal distance between the grid points Δx is 1500 m and this gradually decreases to $\Delta x = 2$ m in the middle 5 km of the domain (figure 4.2a). In this region the sand waves are located. In the rest of the domain the water depth is assumed to be constant and the bed is flat.

In the vertical direction the domain is divided into 60 σ-layers of variable size. The closer the layers are to the bottom, the smaller the percentage of the water depth they contain (figure 4.2b). This higher resolution near the bed is necessary to accurately solve the boundary conditions, flow and sediment transport at this location.

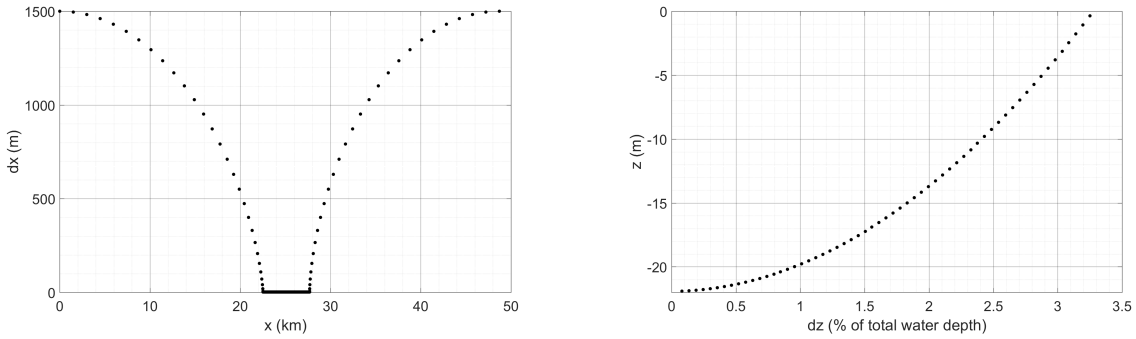

(A) (B)

FIGURE 4.2: (A) The horizontal distance between grid points Δx varies from 1500 m at the boundaries to 2m in the middle of the domain. (B) The vertical distance between grid points varies from from 0.05% of the total water depth at the bed to 3% of the water depth at the surface.

The hydrodynamic run time is 110 days with a time step of $\Delta t = 6$ s. The morphological acceleration factor (MORFAC) is 500, therefore the morphological run time is 150 years,

with a time step of 0.83 hours. The hydrodynamics are run for 5 days, before the bed level updating is switched on. The flow is forced at the lateral boundaries with an M_2 tidal current amplitude of 0.6 m s^{-1}, a frequency of $1.45 \cdot 10^{-4}$ s^{-1} and sea level amplitude of 0.2 m. There is no phase difference imposed between the lateral boundaries. These characteristics are combined into two positive Riemann invariants (Deltares, 2013). The bed slope parameter α_{bs} is set to 3, this corresponds to an angle of repose of sand of $\phi = 19°$ through the relation $\alpha_{bs} = 1/\tan(\phi)$. The median grain size $d_{50} = 0.35$ mm and the sand transport is calculated using the equations of Van Rijn (1993). An overview of all default model settings is given in table 4.1.

	Parameter	**Symbol**	**Value**	**Dimension**
Hydrodynamics	Horizontal width of domain	L_x	50	km
	Undisturbed water depth	H_0	25	m
	Initial sand wave wavelength	λ_0	204	m
	Initial sand wave amplitude	A_0	0.25	m
	Tidal current $x = 0$	$U_{M2,0}$, $\phi_{M2,0}$	0.6, 0	m s^{-1}, degrees
	Tidal current $x = L_x$	$U_{M2,x}$, $\phi_{M2,x}$	0.6, 0	m s^{-1}, degrees
	Water level $x = 0$	$\zeta_{M2,0}$, $\phi_{M2,0}$	0.2, 0	m, degrees
	Water level $x = L_x$	$\zeta_{M2,x}$, $\phi_{M2,x}$	0.2, 0	m, degrees
	Chézy roughness	C	75	$m^{1/2}s^{-1}$
	Background eddy viscosity	ν_{back}	1	m^2s^{-1}
	Background eddy diffusivity	ϵ_{back}	1	m^2s^{-1}
Sand	Median sand grain size	d_{50}	0.35	mm
	Sand density	ρ_s	2650	kg m^{-3}
	Water density	ρ	1000	kg m^{-3}
	Bed slope parameter	α_{bs}	3	-
	Reference height	a	0.01 H_0	m
	Roughness height	k_s	0.01	m
	Bed porosity	ϵ	0.4	-
Numerics	Hydrodynamic time step	Δt	6	s
	Horizontal grid spacing	Δx	2	m
	No of σ-layers	-	60	-
	Morphological acceleration factor	MORFAC	500	-

TABLE 4.1: Overview of default model settings for hydrodynamics, sand transport and numerics.

4.2 Experiments

4.2.1 Sensitivity to numerical parameters

To answer the first research question, a series of runs was performed. In each of these runs, one numerical parameter is changed with respect to the default case.

Morphological acceleration factor

Including a morphological acceleration factor, speeds up the computations, but also introduces errors (Ranasinghe et al., 2011). To make sure that the model results are not influenced by the value of MORFAC that is chosen, runs were performed with a MORFAC of 2000, 1000, 500 and 250.

Time step

To determine the right hydrodynamic time step, the Courant-Friedrichs-Lewy number (also called Courant number) needs to be taken into account. The Courant number relates the phase speed of gravity waves in the model ($c = \sqrt{gH}$ in shallow water) to the grid size and the time step, in order to ensure that the discrete time step chosen is small enough to compute the tidal wave in every horizontal grid point. This number is defined as (Cushman-Roisin and Beckers, 2011):

$$CFL = \frac{\Delta t \sqrt{gH_0}}{\Delta x} \tag{4.2}$$

For stability an maximum value of $CFL = 10$ is advised (Deltares, 2013), but it is recognized that a larger value is possible if the effect of a larger time step is tested. Ensuring that $CFL = 10$ corresponds to a time step of order $\mathcal{O}(1\text{ s})$ for the default model settings. In the default case with $\Delta t = 6$ s, the Courant number is $CFL \approx 46$. To test if the result is different with a different hydrodynamic time step, runs are performed with $\Delta t = 12$ s, $\Delta t = 6$ s, $\Delta t = 3$s and $\Delta t = 1.5$ s.

Number of σ layers and horizontal grid spacing

In the default setting, the vertical domain is divided into 60 σ layers. To test the robustness of this setting, runs were performed with 100 and 20 σ layers. The horizontal grid spacing varies from $\Delta x = 1500$ m at the lateral boundaries to $\Delta x = 2$ m in the middle of the domain. The spacing at the lateral boundaries is kept constant, but runs were performed with $\Delta x = 5$ and 10 m in the middle of the domain. As Δx also influences the Courant number (equation 4.2) and the value of CFL becomes 18 and 9, respectively.

Overview of performed experiments

In table an overview of all experiments with regard to the first research question can be found. All other model settings are the same as in the default case (table 4.1).

	Experiment	Δt (s)	Δx (m)	no. of σ layers	CFL	MORFAC
MORFAC	1A	6	2	60	46	2000
	1B	6	2	60	46	1000
	1C	6	2	60	46	500
	1D	6	2	60	46	250
Δt	1E	12	2	60	95	500
	1F	6	2	60	46	500
	1G	3	2	60	23	500
	1H	1.5	2	60	11	500
σ layers	1I	6	2	100	46	500
	1J	6	2	60	46	500
	1K	6	2	20	46	500
Δx	1L	6	2	60	46	500
	1M	6	5	60	18	500
	1N	6	10	60	9	500

TABLE 4.2: Overview of runs performed to test sensitivity to numerical parameters.

4.2.2 Sensitivity of model results to environmental parameters

To address the second research question, regarding the sensitivity of sand waves to environmental parameters, a series of runs was performed, in each one changing one of the environmental parameters with respect to the default case. In this part, two types of runs were done. The first ones are long term runs to study the finite amplitude behaviour as in the default case. The second type of runs were short runs. With these results the initial growth and migration rates were studied. In all these runs, λ_0 is the same as in the default case.

Water depth

The undisturbed water depth H_0 in the default case is 25 m. To investigate the long term evolution of the sand waves in shallower water, H_0 was decreased to 21.5 m. This is the water depth measured in the Hollandse Kust Zuid area, the case study described in section 4.2.3. Besides this, a short run with $H_0 = 30$ m was performed, to compare the initial growth rates for different water depths.

Sand grain size

In the default case, the median grain size $d_{50} = 0.35$ mm. A long run with $d_{50} = 0.25$ mm was done to study the evolution of sand waves formed in a bed with finer sand. Also a

short run with $d_{50} = 0.45$ mm was done, so the initial growth rates could be compared to those of the first two cases.

Bed slope parameter

In the default case $\alpha_{bs} = 3$, corresponding to an angle of repose of 19°. However, other values of α_{bs} are also possible. Based on the results of Sekine and Parker (1992), the angle of repose of sand in water filled sand ranges between 15°2pt and 30°. Therefore, three short runs were performed to study the effect of the bed slope parameter α_{bs} on the characteristics of initially forming sand waves. In these runs $\alpha_{bs} = 12$, $\alpha_{bs} = 6$ and $\alpha_{bs} = 1.5$. These values correspond to angles of 5° , 10° and 34°, respectively.

Tidal forcing

In the default case the flow was forced with the M_2 tidal constituent with an amplitude of 0.6 m s^{-1}. A long run with $M_2 = 0.75$ m s^{-1} was performed to investigate the effect of stronger currents. This amplitude was chosen, because it is the M_2 amplitude in the Hollandse Kust Zuid area (section 4.2.3). The effect of a smaller amplitude (0.5 m s^{-1}) was studied by doing a short run and investigating the initial formation. As asymmetrical tidal forcing causes sand wave migration, the effect of including a residual current M_0 with amplitude 0.05 m s^{-1} was investigated in a short run. The final four short runs include the first overtide M_4 with an amplitude of 0.05 m s^{-1}. The difference between these runs is the phase difference θ between M_2 and M_4. In the first case $\theta = 60°$, which is the phase difference between M_2 and M_4 in the HKZ area. To gain insight in the sensitivity to this phase, runs with $\theta = 120°$ and 180°were done. In a final short run, both M_4 (with $\theta = 60°$) and M_0 are included. This tidal forcing is similar to the tidal forcing in the HKZ area.

Overview of performed experiments

	Experiment	H_0 (m)	d_{50} (mm)	Tide (m s^{-1})	α_{bs}	Type
H_0	2A	21.5	0.35	M_2: 0.6	3	long
	2B	25	0.35	M_2: 0.6	3	long
	2C	30	0.35	M_2: 0.6	3	short
d_{50}	2D	25	0.25	M_2: 0.6	3	long
	2E	25	0.35	M_2: 0.6	3	long
	2F	25	0.45	M_2: 0.6	3	short
α_{bs}	2G	25	0.35	M_2: 0.6	1.5	short
	2H	25	0.35	M_2: 0.6	3	short
	2I	25	0.35	M_2: 0.6	6	short
	2J	25	0.35	M_2: 0.6	12	short
Tide	2K	25	0.35	M_2: 0.6	3	long
	2L	25	0.35	M_2: 0.75	3	long
	2M	25	0.35	M_2: 0.5	3	short
	2N	25	0.35	M_2: 0.6, M_4: 0.05, $\theta = 60°$	3	short
	2O	25	0.35	M_2: 0.6, M_4: 0.05, $\theta = 120°$	3	short
	2P	25	0.35	M_2: 0.6, M_4: 0.05, $\theta = 180°$	3	short
	2Q	25	0.35	M_2: 0.6, M_0: 0.05	3	short
	2R	25	0.35	M_2: 0.6, M_0: 0.05, M_4: 0.05, $\theta = 60°$	3	short

TABLE 4.3: Overview of runs to test sensitivity to environmental parameters

4.2.3 Application to an observed sand wave field

To address the third research question an observed sand wave field in the area of the future wind farm Hollandse Kust Zuid (HKZ) was used as an initial bed. This park will be located approximately 20 km off the coast, in the area between Scheveningen and Katwijk aan Zee (Noordzeeloket, 2017), as shown in figure 4.3.

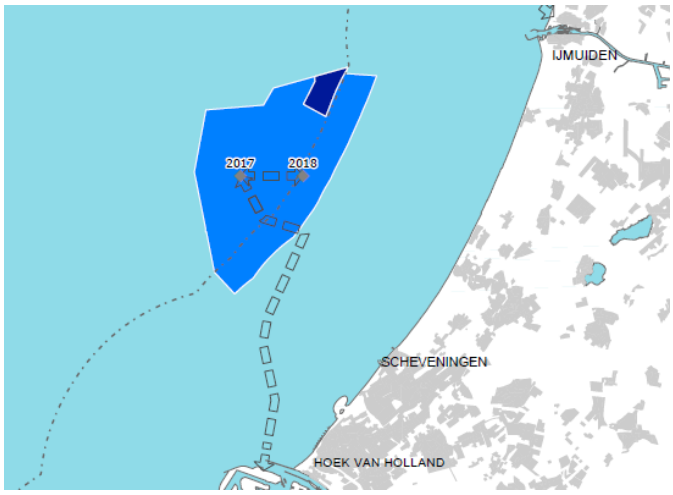

FIGURE 4.3: Location of the future wind park Hollandse Kust Zuid (source: Noordzeeloket (2017).

Two sets of bathymetry data from the HKZ area were used: the first is based on measurements by the Hydrographic Office of the Royal Dutch Navy in 1999 using single beam echosounding; the second is based on measurements by the offshore survey service Fugro in 2016 using multi beam echosounding. From this data, a 5 km transect close to point kp 40 was taken, the location of this transect is indicated by the red line in figure 4.4.

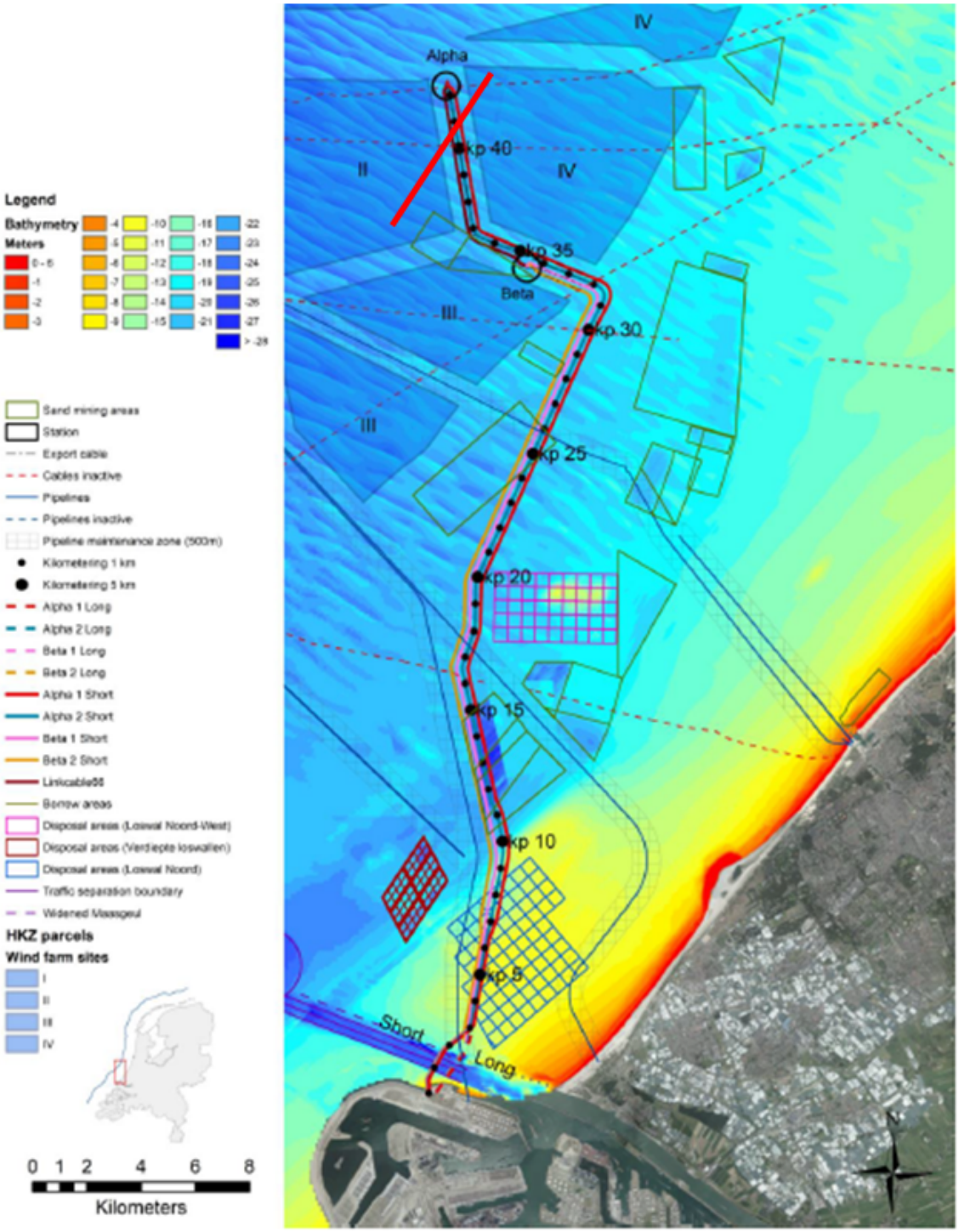

FIGURE 4.4: The planned location of the cable connecting HKZ to the mainland plotted on a bathymetry map based on measurements by Fugro in 2016 (source: WaterProof B.V. (2017)).

The data points were interpolated onto the grid using triangular interpolation. Before used as model input, the data in both sets were shifted to the same reference depth to minimize the effect of systematic measurement errors. This reference depth is $H_0 = 21.52$ m. The resulting bed levels are shown in figure 4.5. The bed level measured in 1999 is shown in black and the 2016 bed level in red.

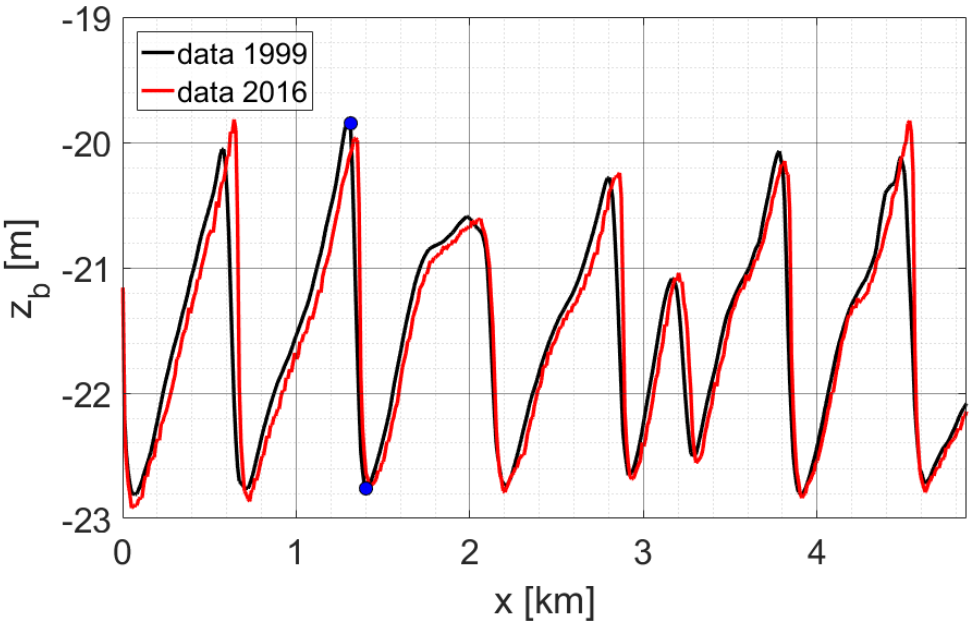

FIGURE 4.5: The bed level z_b at the HKZ transect as measured in 1999 (black) and 2016 (red). Blue dots indicate the sand wave that will be tracked in time (to be used later).

In 2016, offshore survey service Fugro also took sediment samples from which the median grain size was determined. Along the transect the d_{50} varied from 0.25 mm to 0.3 mm. In this study, it is assumed that this has not changed in the period 1999-2016, therefore all model runs regarding the HKZ case have $d_{50} = 0.25$ mm as input.

Determination of tidal forcing at HKZ location

The amplitudes and phases of the tidal constituents were determined based on the output of the Dutch Continental Shelf model (DCSMv6, see Zijl et al. (2013)). This model simulates the depth averaged flow and water level for the Dutch continental shelf. To find the coordinates of the locations of the boundaries $x = 0$ and $x = L_x$, the transect extended was both 22.5 km in the southwestern and 22.5 km in the northeastern direction. At these locations the output of the DCSMv6 model was taken. These time series of flow and water level were harmonically analysed using T-TIDE (Pawlowicz et al., 2002). The resulting amplitudes and phases of the current U and water level ζ are listed in table 4.4. These are combined into Riemann invariants and imposed on the lateral boundaries. On the southwestern boundary a positive Riemann invariant is imposed and on the northeastern boundary a negative invariant.

	Southwest			
	U [m s^{-1}]	Phase [degrees]	ζ [m]	Phase [degrees]
M_0	0.004	-	0.069	-
M_2	0.748	70.60	0.625	54.88
M_4	0.057	57.30	0.147	104.04
	Northeast			
	U [m s^{-1}]	Phase [degrees]	ζ [m]	Phase [degrees]
M_0	0.005	-	0.068	-
M_2	0.768	87.98	0.4877	105.24
M_4	0.057	167.05	0.1377	132.42

TABLE 4.4: Overview of phases and amplitudes of tidal constituents following from DCMv6 and T-TIDE.

Experiments

To study the evolution of this mature sand wave field of 1999, several runs were performed with different tidal forcing. The morphological run time was 17 years, so the output could be compared to the measurements of 2016. Since MORFAC is 500, this corresponds to a hydrodynamic run time of almost 2 weeks. In the middle 5 km of the model domain the transect measured at HKZ was placed. The numerical settings were the same as in the default case, but the water depth and the grain size are changed to the measured values in the HKZ area, i.e. $H_0 = 21.5$ m and $d_{50} = 0.25$ mm. As tidal forcing, the results of the Dutch Continental Shelf Model are combined into Riemann invariants and imposed on the southwestern (x=0) and the northeastern boundary (x=L_x) (table 4.4). First, a run with only the M_2 tide was done, which is the dominant tidal component in this location. Then, the residual current M_0 and M_4 were added separately. Finally, a run was performed with both M_2, M_4 and M_0.

Experiment	**Tidal forcing**
3A	M_2
3B	M_2 + M_0
3C	M_2 + M_4
3D	M_2 + M_4 + M_0

TABLE 4.5: Overview of runs with observed mature sand waves as an initial bathymetry.

4.3 Methodology to analyse results

4.3.1 Residual velocity

To identify the residual circulation cells, the residual velocity $\overrightarrow{u}_{m0}$ is computed by integrating the velocity over time and dividing by the amount of time passed,

$$\overrightarrow{u}_{m0} = \frac{1}{T}\int_0^T \overrightarrow{u}\,dt. \tag{4.3}$$

The residual sand transport is calculated in a similar way.

4.3.2 Initial growth and migration rate

The initial growth and migration rates were determined using linear stability analysis. In linear stability analysis the bed z_b is assumed to consist of a basic state z_{b0} (i.e. a flat bed) with a superimposed small perturbation h (Besio et al., 2008):

$$z_b(x,t) = z_{b0}(x) + h(x,t) \quad \text{with } |h| \ll |z_{b0}| \tag{4.4}$$

Because the perturbations are small, this allows for linearisation of the problem, yielding in the following equation for h,

$$\frac{\mathrm{d}h(x,t)}{\mathrm{d}t} = \Gamma(t)h(x,t). \tag{4.5}$$

With Γ the complex growth rate $\Gamma(t) = \gamma_r(t) + i\gamma_i(t)$. This growth rate depends on the wave length of the perturbation, the sand characteristics and on the flow. Since the tide oscillates, Γ is also a periodic function in time and can be split into a time averaged value $\bar{\Gamma}$ and a periodic part $\widetilde{\Gamma}$. The solution of the equation 4.5 is

$$h(x,t) = A_0(x)\exp\left[\int_0^t \Gamma(t)\mathrm{d}t\right]. \tag{4.6}$$

This results in the following solution for the bed z_b,

$$z_b(x,t) = z_{b0}(x) + \Re\left\{A_0(x)\exp\left[\bar{\gamma}_r t + \int_0^t (\widetilde{\gamma}_r(t)\mathrm{d}t\right]\exp\left[i\left(k_x x + \bar{\gamma}_i t + \int_0^t \widetilde{\gamma}_i(t)\mathrm{d}t\right)\right]\right\} \tag{4.7}$$

In this equation, $\Re$ denotes that only the real part of the complex variable is taken into account, k_x is the wave number, describing the wavelength λ of the perturbation since $\lambda = 2\pi/k_x$. The periodic parts of the growth and migration rate ($\widetilde{\gamma}_r$ and $\widetilde{\gamma}_i$) are small, because they describe oscillations during a tidal cycle. Therefore, these terms can be neglected, this yields for the bed perturbation

$$h(x,t) = A_0\exp\left[\bar{\gamma}_r t + i(k_x x + \bar{\gamma}_i t)\right]. \tag{4.8}$$

If $\bar{\gamma}_r > 0$ for a certain wave length, the basic state is unstable and this perturbation growths exponentially in time. The basis state is stable with respect to that perturbation, if $\bar{\gamma}_r < 0$. The imaginary time-averaged part of the growth rate $\bar{\gamma}_i$ is related to the migration of the perturbation as the phase speed is $c_x = -\bar{\gamma}_i/k_x$.

The time-averaged parts of the initial growth and migration rates will from now be denoted by γ_r and γ_i, respectively. These can be found by writing the bed perturbation h as Fourier series A_n (see e.g. Press et al. (1988))

$$A_n(k_n,t) = \sum_{j=0}^{N_x-1} h(x_j,t)\exp(ik_n x_j). \tag{4.9}$$

Here, $x_j = j\Delta x$ with $j = 0,1,2,..N_x - 1$ and k_n the wave number

$$k_n = \frac{2\pi n}{N_x}, \quad \text{with } n = -\frac{N_x - 1}{2}, .. \frac{N_x - 1}{2}. \tag{4.10}$$

The inversion of the Fourier series is,

$$h(x_j, t) = \sum_{n=-\frac{N_x-1}{2}}^{\frac{N_x-1}{2}} A_n(k_n, t) \exp(ik_n x_j) \tag{4.11}$$

Combining equations 4.8 and 4.11 and taking the natural logarithm, yields in equations for the growth rate γ_r and migration rate γ_i,

$$\gamma_r = \frac{1}{T_{01}} \Re\left\{ \ln\left(\frac{A_0}{A_1}\right)\right\}, \tag{4.12}$$

$$\gamma_i = -\frac{1}{k_x T_{01}} \Im\left\{ \ln\left(\frac{A_0}{A_1}\right)\right\}. \tag{4.13}$$

Here, $T_{01} = t_1 - t_0$, with t_0 the starting time and t_1 the time for which $A = A_1$.

4.3.3 Dominant wave length

The dominant wave length is determined by writing the bed level as a Fourier series (equations 4.11, 4.10 and 4.8). Then the power spectral density P (see e.g. Press et al. (1988)) can be computed at a certain time t,

$$P(k_n, t) = \frac{1}{N_x} |A(k_n, t)|^2. \tag{4.14}$$

When this power is plotted against k_n, the dominant wave lenghts in the signal $h(x_j, t)$ are revealed.

4.3.4 Global growth and migration rate

The global growth rate σ of the sand waves is calculated using the equation of Garnier et al. (2006):

$$\sigma = \frac{1}{h_{rms}^2} \overline{h \frac{\partial h}{\partial t}}. \tag{4.15}$$

Here h is the height of the bed relative to the undisturbed water depth H_0 and h_{rms} is the root-mean square of the bed perturbation:

$$h_{rms} = \sqrt{(\overline{h^2})} \tag{4.16}$$

The bar means that this value is averaged over the domain: $\frac{1}{L_x} \int dx$. The global migration rate V_m is calculated after Vis-Star et al. (2008):

$$V_m = -\frac{1}{(\overline{\frac{\partial h}{\partial x}})^2} \overline{\frac{\partial h}{\partial x} \frac{\partial h}{\partial t}}. \tag{4.17}$$

4.3.5 Wave height

The crest heights h_c and trough depths h_t of the sand waves are determined by identifying the local maxima and minima in the bed level $z_b(x,t) = H_0 + h(x,t)$. The sand wave heights are defined as the vertical difference between the crests and their subsequent troughs. To analyse the evolution of h_c and h_t over time, one sand wave is chosen. For the default case and the sensitivity to numerical and environmental parameters, this sand wave is located in the middle of the domain. In the HKZ case, one sand wave in the left of the domain is selected, of which the crest and trough are indicated by the blue dots in figure 4.5.

Chapter 5

Results

In this chapter, the results are presented. First, the initial state and the time-evolution of the default case are shown. Secondly, the sensitivity to numerical parameters is discussed, followed by the sensitivity to environmental parameters. Finally, the results from the application of the model to an observed sand wave field are presented.

5.1 Default case

The model configuration and values of the parameters of the model default case have been presented in section 4.1.

5.1.1 Initial state

Phase and amplitude of M_2

The phase and amplitude of the M_2 horizontal tidal velocity component u at the beginning of the simulation (with the bed level as in figure 4.1) are shown in figure 5.1. The amplitude of M_2 varies from a maximum of 0.58 m s $^{-1}$ at the surface, to 0.14 m s $^{-1}$ close to the bottom. The phase ϕ varies from 217° at the surface to 215° at the bottom. Initially, there is little horizontal variation in both the amplitude and phase of M_2. The tide is not progressive, due to the imposed boundary conditions.

The lower two panels of figure 5.1 show the amplitude and phase of the M_2 vertical tidal velocity component w. Vertical velocity is generated in the sand wave area, resulting from interaction of u with the sand wave field. In this area, the M_2 vertical velocity varies from a maximum value of $2.8{\cdot}10^{-3}$ m s $^{-1}$ at the bottom, at the location with the steepest bed slope and it decreases to 0 m s $^{-1}$ at the crests and troughs. There is a 180° phase difference γ between w up- and downstream of the crest. The phases and amplitudes of M_2 for the whole domain are given in appendix B.

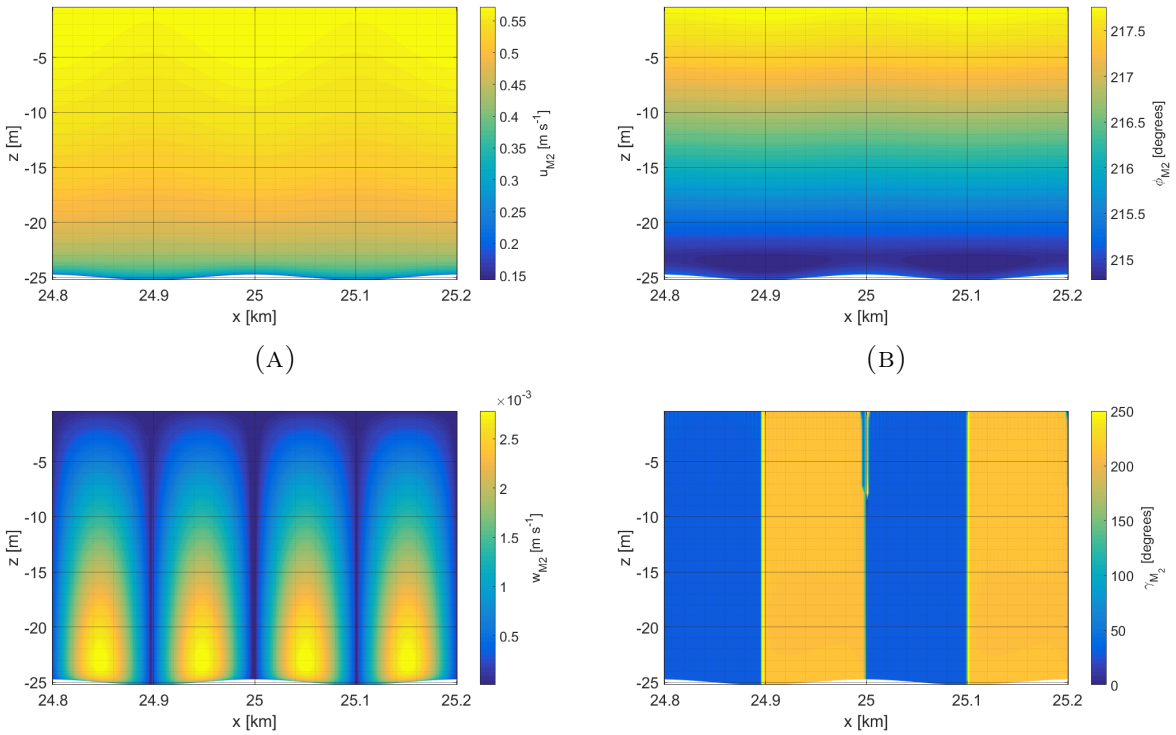

FIGURE 5.1: Amplitude U_{M2} (A) and phase ϕ_{M2} (B) of the M_2 horizontal tidal velocity component at $t = 0$ as a function of horizontal coordinate x and vertical coordinate z. Amplitude W_{M2} (C) and phase γ_{M2} (D) of the M_2 vertical tidal velocity component at $t = 0$.

Residual velocity

Averaging the velocity over a tidal cycle results in the residual velocity. Both the horizontal and vertical component of the residual velocity are shown in figure 5.2. The horizontal component of the residual velocity $\langle u \rangle$ is positive on the left side of the crest and negative at the right side. This means that the residual velocity close to the bed is always pointing towards the crest. The magnitude of $\langle u \rangle$ decreases from $1.9{\cdot}10^{-3}$ m s $^{-1}$ above the steepest slope to 0 m s $^{-1}$ at the crest and trough. Higher in the water column, the direction of the velocity is opposite to that at the bed and the magnitude is of the order $1{\cdot}10^{-4}$ m s $^{-1}$.

The vertical component of the residual velocity $\langle \omega \rangle$ vanishes outside of the sand wave area. In the sand wave area, the maximum magnitude is $6{\cdot}10^{-5}$ m s $^{-1}$ and is found above the crests (pointing upwards) and above the troughs (pointing downwards). The magnitude decreases towards the surface and towards the location of the steepest slope. Combining the horizontal and vertical components of the residual velocity results in the residual circulation cells pointing towards the crest at the bottom and towards the trough higher in the water column, similar to figure 2.6.

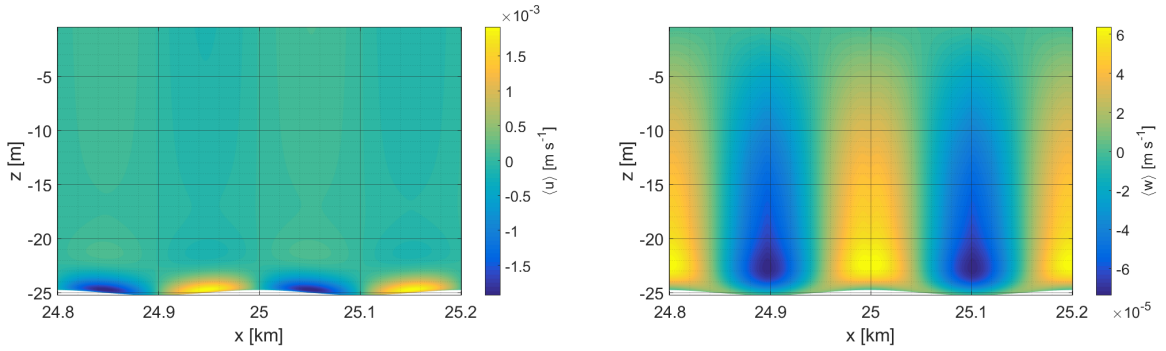

(A) (B)

FIGURE 5.2: (A) Horizontal component of residual velocity $\langle u \rangle$ at $t = 0$. (B) Vertical component of residual velocity $\langle w \rangle$ at $t = 0$.

Sand transport

Similar to the residual velocity, maximum values of the residual bed load $\langle q)b \rangle$ and suspended load transport $\langle q_s \rangle$ appear on the left and right side of the crest (figure 5.3a). These maxima have opposite signs. Since a positive value corresponds to a transport in the positive x-direction and vice versa, there is a convergence of sand at the crest and a divergence of sand in the trough. The horizontal gradient of sand transport $\langle q_b \rangle$ (figure 5.3b) indicates that the maximum sand transport is found at the crest and trough and that these have opposite signs. Because of the sediment continuity equation (3.16),

$$(1 - \epsilon_p)\frac{\partial z_b}{\partial t} + \frac{\partial (q_b + q_s)}{\partial x} = 0, \tag{5.1}$$

a negative value of the horizontal sand transport gradient, results in a rise of the bed level, which happens at the crest. The exact opposite is true for the troughs, resulting in a lowering of the bed level. Figure 5.3b reveals that $\frac{\partial \langle q_b \rangle}{\partial x}$ is asymmetric, as the peak above the troughs is larger in magnitude, but the peak at the crests spans a wider area.

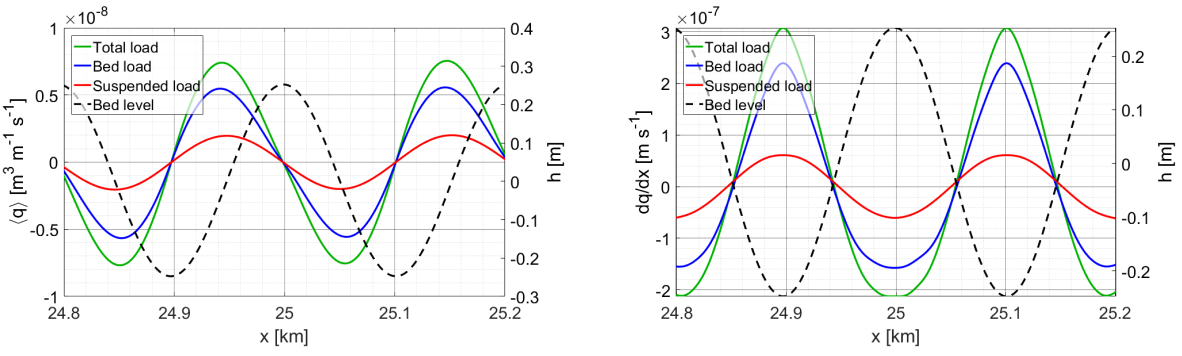

(A) (B)

FIGURE 5.3: (A) The residual bed load $\langle q_b \rangle$ (blue), suspended load $\langle q_s \rangle$ (red) and total sand transport $\langle q_t \rangle$ (green) at $t = 0$. The black dotted line is the bed level h and corresponds to the right y-axis. (B) Horizontal gradient of residual sand transport $\frac{\partial \langle q_b \rangle}{\partial x}$ (blue), $\frac{\partial \langle q_s \rangle}{\partial x}$ (red) and $\frac{\partial \langle q_t \rangle}{\partial x}$ (green).

5.1.2 Evolution of variables over time

The net convergence of sand at the crest and net divergence of sand at the trough cause the sand waves to grow until they reach a finite amplitude. This is evident from figure 5.4a, which shows the evolution of the crest height and trough depth over time. Crest height and trough depth h are defined with respect to the undisturbed bed level $z_{b0} = -H_0$ and their location is indicated in figure 5.4b. Initially, between $t = 0$ and $t = 50$ years, the crests grow exponentially, after which their growth reduces until they reach a saturation value of 5.5 m at $t \simeq 70$ years. The reduction of the growth of the troughs already starts after 40 years and these troughs reach equilibrium in about 60 years. The trough depth is then 3.6 m, resulting in a total wave height (crest to trough distance) of 9.1 m.

Now consider the four morphological times $t_1 = 1$ year, $t_2 = 37.5$ years, $t_3 = 75$ years and $t_4 = 125$ years. The bed level at each of these times is shown in figure 5.4b. The initial residual sand transport was slightly asymmetric (figure 5.3b) and this causes the sand waves to grow asymmetric in shape. After 1 year (magenta), the bed is close to the initial bed, but after 37.5 years (blue) the crests have grown to a height of 1 m and the troughs to a depth of 1.5 m. The troughs are stabilized and flattened at a depth of 3.5 m at $t_3 = 75$ years (red). The crests grow another meter from 4.5 to 5.5 m in the following years ($t_4 = 125$ years, green).

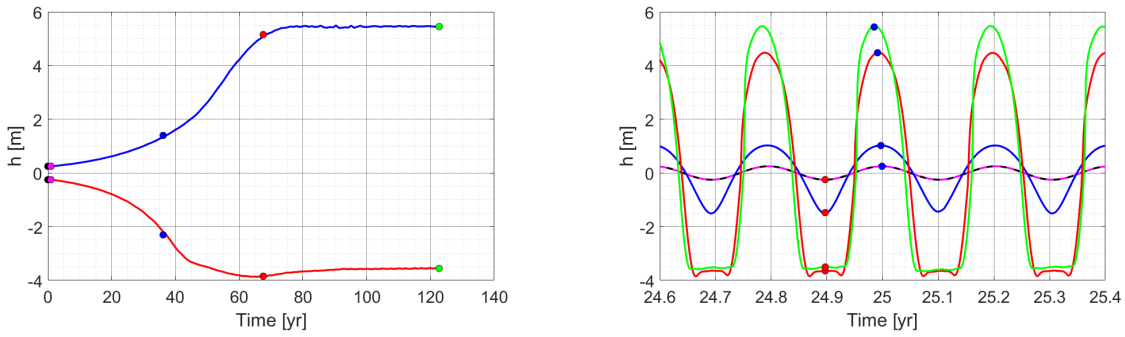

(A) (B)

FIGURE 5.4: (A) The evolution of crest height (upper blue line) and trough depth (lower blue line) over time. (B) The initial bed level in black, the bed level after 1 year (dotted magenta line), after 37.5 years (blue line), after 75 years (red line) and after 125 years (green line).

The growth of the sand waves impacts the residual velocity patterns. As the wave height increases, there are larger differences in water depth in the domain. This causes the magnitude of the residual velocity to increase, which becomes clear in figure 5.5. Here, $\langle u \rangle$ and $\langle w \rangle$ are shown at $t_2 = 37.5$ years and at $t_4 = 125$ years (note the difference in scale). Especially in figure 5.5d the velocity becomes large, because of the steep slopes. The residual velocity at $t_1 = 1$ year and $t_3 = 75$ years is given in figure B.1.

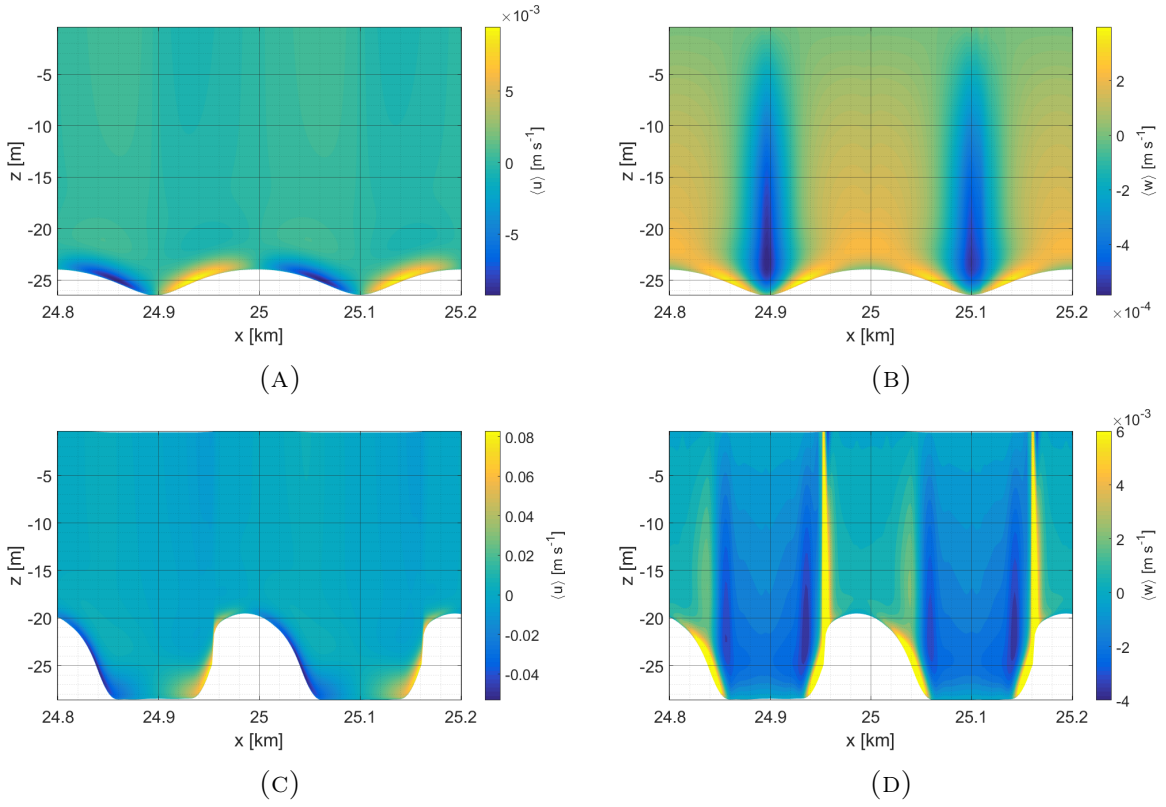

FIGURE 5.5: The horizontal (A) and vertical (B) components of the residual velocity ($\langle u \rangle$ and $\langle w \rangle$) at $t_2 = 37.5$ years. The horizontal (C) and vertical (D) components of the residual velocity ($\langle u \rangle$ and $\langle w \rangle$) at $t_4 = 125$ years. Note the difference in scales.

The growth and shape change of the sand waves affects the residual sand transport. The magnitude increases until the sand waves are in equilibrium (figure 5.6 and compare figure 5.6b with figure C.1). The residual sand transport is nonzero at the crest, even when the sand waves are in equilibrium. This is because the crests move from slightly left to right without changing their wave height (figure 5.4b). Therefore, the peaks in $\frac{\partial \langle q_t \rangle}{\partial x}$ are located at the sides of the crests. The troughs are stable in the equilibrium state and there $\frac{\partial \langle q_t \rangle}{\partial x} = 0$.

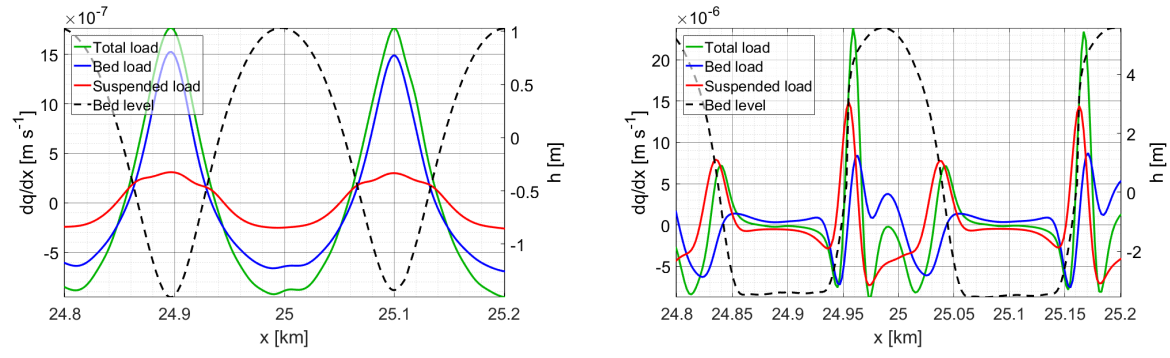

FIGURE 5.6: The residual bed load $\langle q_b \rangle$ (blue), suspended load $\langle q_s \rangle$ (red) and total sand transport $\langle q_t \rangle$ (green) at (A) $t_2 = 37.5$ years and (B) $t_4 = 125$ years. The black dotted line is the bed level h and corresponds to the right y-axis.

5.2 Sensitivity to numerical parameters

In this section, the sensitivity of the model results to numerical parameters will be explored by comparing the time-evolution of the trough and crest height for different cases. The residual velocity in the different cases is presented in appendix B and the residual sand transport is shown in appendix C.

5.2.1 Morphological acceleration factor

The results of experiments 1A - 1D (table 4.2) are shown in figure 5.7a, where the time evolution of trough depth and crest height is depicted. Although all simulations result in approximately the same time scale ($\sim$ 70 years) and the same crest height ($\sim$ 5.5 m) and trough depth ($\sim$ 3.8 m), a too large MORFAC (MF = 2000) causes oscillations of the finite crest height. These oscillations are reduced for decreasing MORFAC, which is clearly visible in figure 5.7b. This figure shows the difference between the crest height in the default case (MF = 500) and crest heights in cases with different MORFAC. The trough depths are relatively less affected by MORFAC than the crests (figure 5.7c). The maximum difference in the crest height compared to the default case is 0.75 m and results from choosing MORFAC 2000. This is reduced to 0.2 m (MF = 1000) and 0.1 m (MF = 250) for smaller values of MORFAC. The largest difference in trough depth occurs at 40 years and is 0.44 m and 0.21 m for a MORFAC of 2000 and 1000, respectively. For MF=250 the maximum difference with the default case (MF = 500) of the trough depth is 0.1 m. So, for both the saturation crest height, trough depth and time scale, a MORFAC of 500 is optimal in terms of both accuracy and computation time, as decreasing this value leads to minimal changes. Nevertheless, MORFAC of 2000 is used to conduct the rest of the experiments regarding the sensitivity to numerical parameters to save computation time.

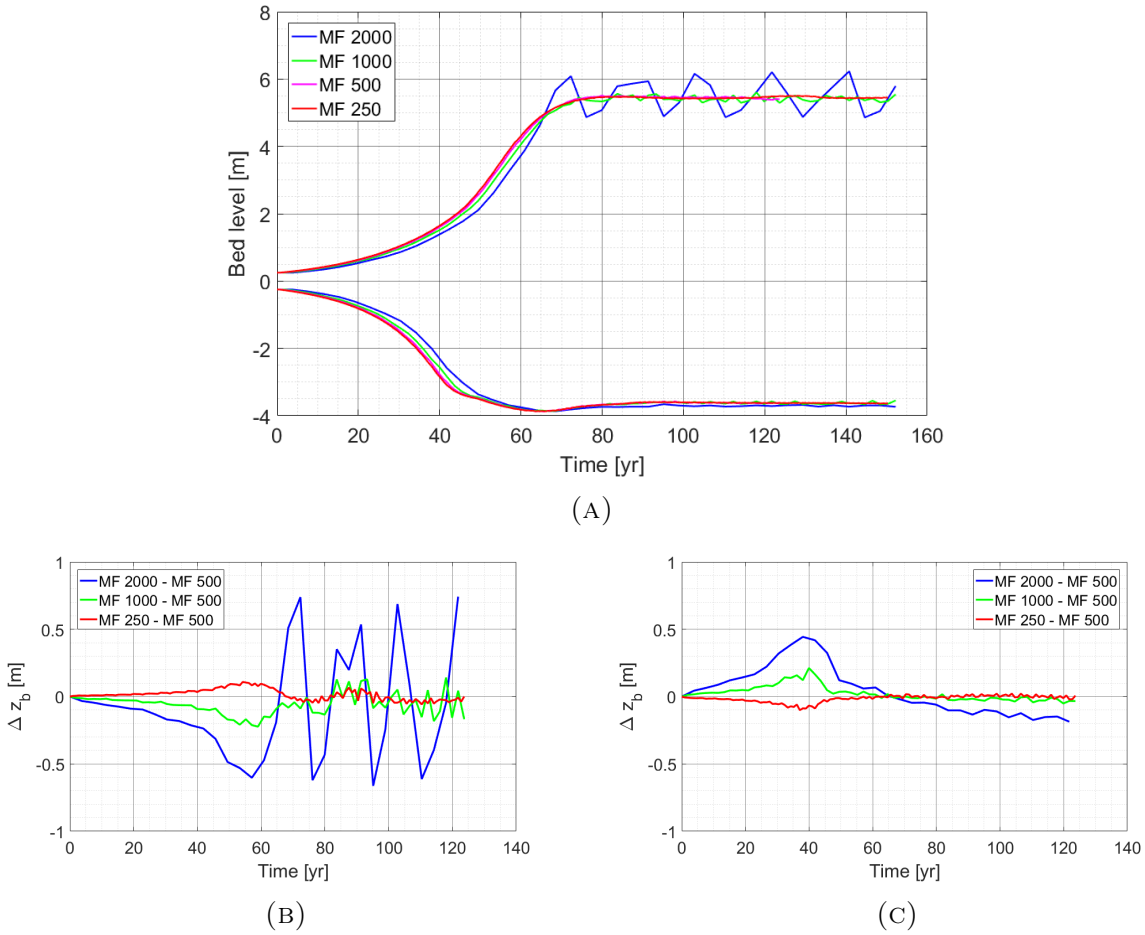

FIGURE 5.7: (A) As in figure 5.4a, but for a morphological acceleration factor MF = 2000 (blue), MF = 1000 (green), MF = 500 (magenta) and MF = 250 (red). (B) The difference in crest height MF 2000 (blue), MF 1000 (green) and MF 200 (red) and the default case (MF 500). (C), as (B), but for trough depth.

5.2.2 Time step

The result of experiments 1E - 1H (table 4.2) are shown in figure 5.8a. This figure shows the evolution of the crest height and the trough depth over time for runs with different hydrodynamic time steps. The result with $\Delta t = 12$ s is not included in the figure, because the simulation crashed due to a too high Courant number. Overall, both the equilibrium time scale (approximately 70 years) and the equilibrium crest height (5.5 m) and trough depth (3.8 m) of runs with $\Delta t = 6$ s, 3 s and 1.5 s are the same. Figures 5.8b and 5.8c show the difference in crest height and trough depth relative to the default case, which has $\Delta t = 6$ s. The crest height is more strongly affected by using smaller Δt than the trough depth. For instance, choosing $\Delta t = 3$ s results in a maximum difference in crest height of 0.35 m and a maxmimum difference in trough depth of 0.09 m with respect to $\Delta t = 6$ s. For $\Delta t = 1.5$ s these differences are 0.45 m and 0.1 m, respectively. Therefore, it can be concluded that $\Delta t = 6$ s is sufficient to compute the finite amplitude behaviour of sand waves.

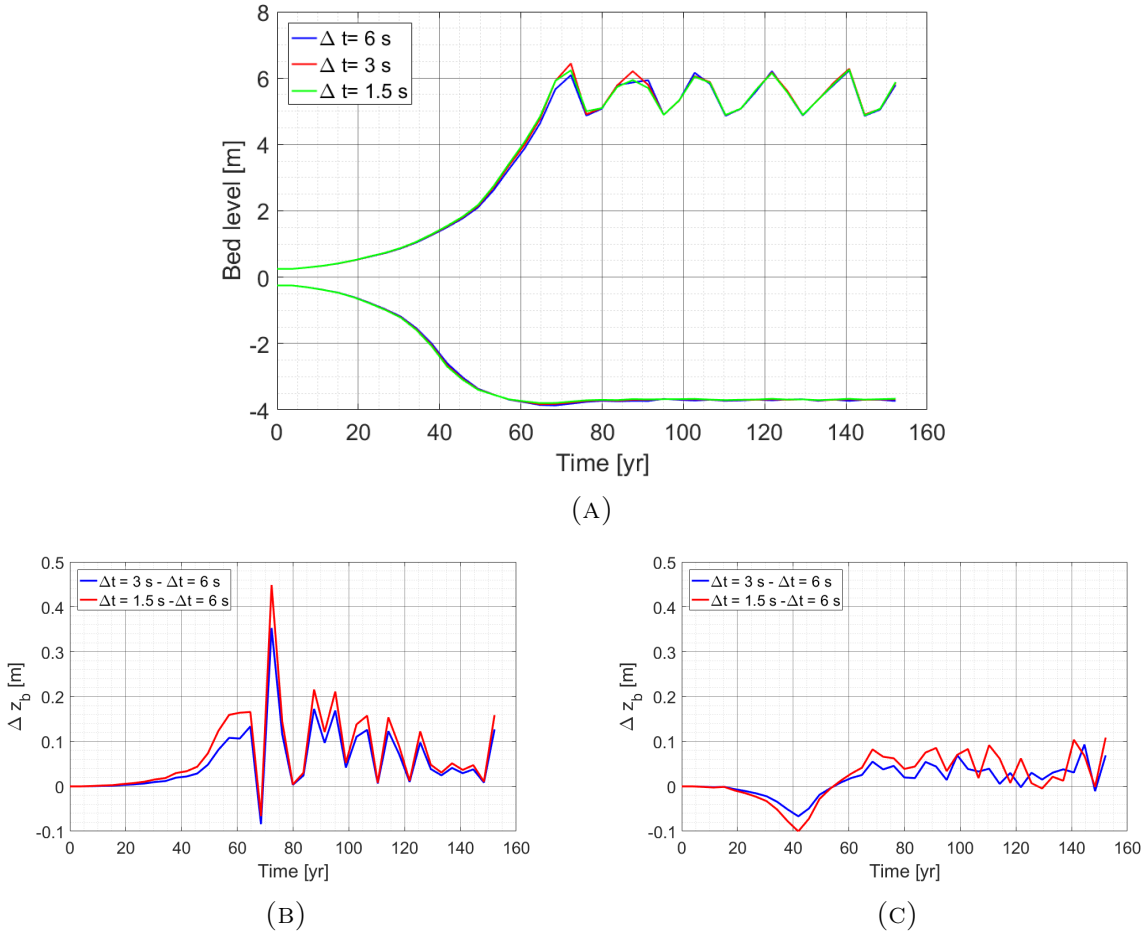

FIGURE 5.8: (A) As in figure 5.4a, but for hydrodynamic time step $\Delta t = 6$ s (blue), $\Delta t = 3$ s (red) and $\Delta t = 1.5$ s (green). (B) The difference in crest height between $\Delta t = 3$ s (blue), $\Delta t = 1.5$ s (red) and the default case ($\Delta t = 6$ s). (C), as (B), but for trough depth.

5.2.3 Grid size

Vertical resolution

The verification of the sensitivity of the model results to the number of σ-layers is done only for the initial formation in order to save computation time (experiments 1I - 1K, table 4.2). These results are presented in figure 5.9, which shows the initial growth rates γ_r for different numbers of σ-layers . In default model settings, 60 σ-layers are included, resulting in an initial growth rate of $2.4 \cdot 10^{-9}$ s^{-1}. When 100 layers are used, the growth rate is approximately the same. This is not the case for 20 layers, because then the growth rate changes to - $0.2 \cdot 10^{-9}$ s^{-1}. These results clearly demonstrate that a sufficient amount of σ-layers is needed to accurately resolve the sand wave dynamics. The difference can be explained by differences in the horizontal component of the residual velocity (figure B.3). The maximum magnitude of $\langle u \rangle$ for 20 σ layers is significantly lower than for 60 and 100 σ layers, which results in less residual sand transport.

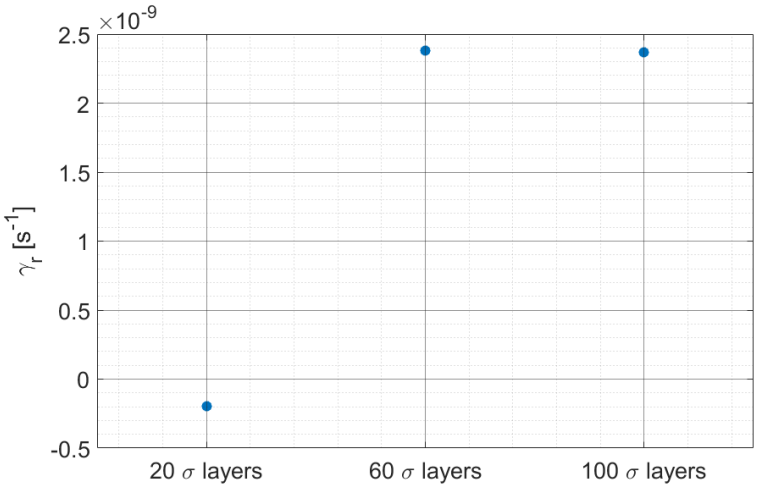

FIGURE 5.9: Initial growth rates in the cases of 20, 60 and 100 σ-layers.

Horizontal grid size

From figure 5.10a, it appears that large differences exist between crest heights and trough depths for different cases of Δx (experiments 1L - 1N in table 4.2). Increasing horizontal grid spacing Δx results in 1) an increase of the saturation time scale; 2) a reduction of the crest height; and 3) an increase of the trough depths. It is interesting to note that the oscillations in the finite crest height disappear with increasing Δx. Figures 5.10b and 5.10c show the differences of the crest height and trough depth with respect to the default case, which has $\Delta x = 2$ m. For $\Delta x = 5$ m the maximum differences in crest height and trough depth are 2.1 m and 0.8 m, respectively. When a grid spacing of 10 m is used, the crest height differs 3.8 m relative to the default case ($\Delta x = 2$ m)and the trough depth 2 m.

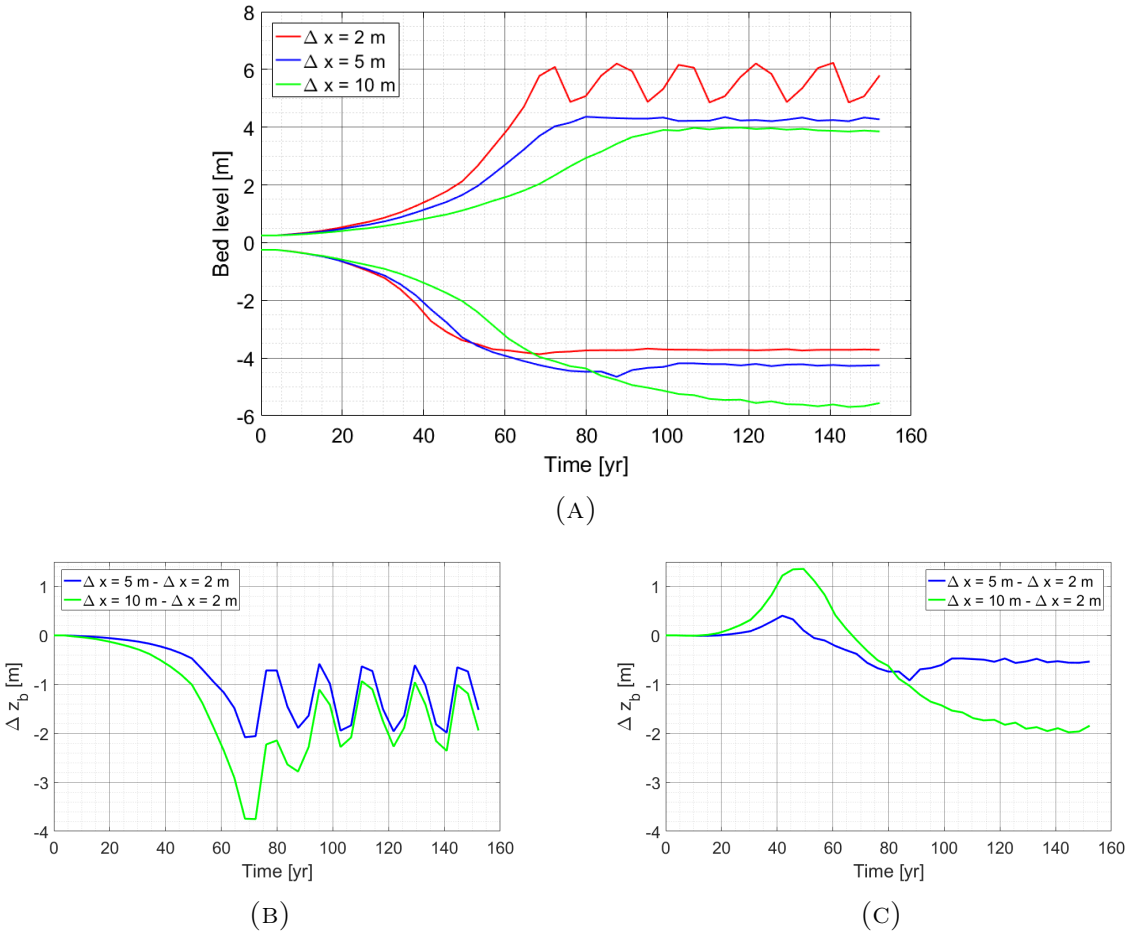

FIGURE 5.10: (A) As in figure 5.4a, but for horizontal grid spacing $\Delta x = 2$ m (red), $\Delta x = 5$ m (blue) and $\Delta x = 10$ m (green). (B) The difference in crest height between $\Delta x = 5$ m (blue), $\Delta x = 10$ m (green) and the default case ($\Delta x = 2$ m). (C) as in (B), but for trough depth.

5.3 Sensitivity of model results to environmental parameters

In this section, the sensitivity of sand wave characteristics to environmental parameters will be explored with the experiments described in section 4.2.2. For each case, the initial growth and migration rates (if present) and the time evolution of the trough depth and crest height will be presented. The residual velocity of the different cases is presented in appendix B and the residual sand transport of the different cases is shown in appendix C.

5.3.1 Water depth

The initial growth rate decreases with increasing values of the undisturbed water level H_0, which becomes clear from figure 5.11a in which the initial growth rate for different cases of H_0 is shown (experiments 2A - 2C in table 4.3). Figure 5.11b displays the long-term

time evolution of crest height and trough depth for $H_0 = 21.5$ m (red line) and $H_0 = 25$ m (blue line). Clearly, with increasing H_0 it takes longer for the crests and troughs to reach their equilibrium values. The equilibrium wave height (crest to trough distance) is higher in deeper water, it is 8.8 m for $H_0 = 21.5$ m and 9.2 m for $H_0 = 25$ m. The difference is caused by deeper troughs for $H_0 = 25$ m. The processes of both growth and saturation are weakened, but growth weakens less than saturation in deeper water.

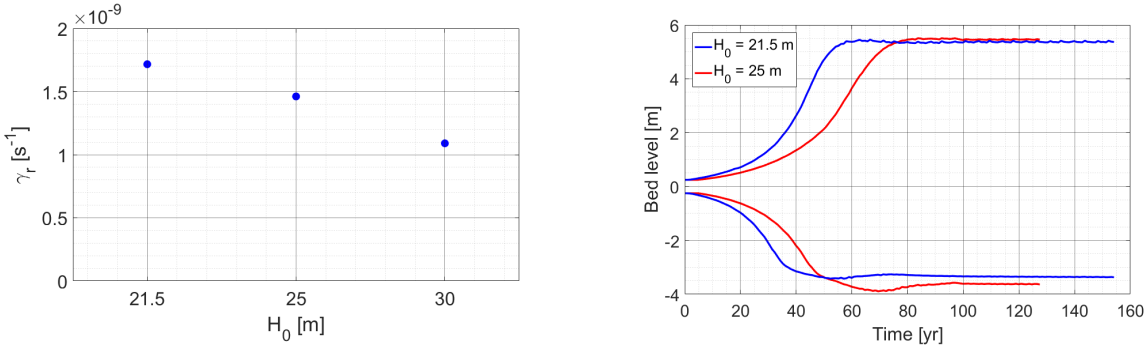

(A) (B)

FIGURE 5.11: (A) Initial growth rate γ_r for different values of mean water depth H_0. (B) Evolution of crest height and trough depth over time for $H_0 = 21.5$ m (red) and $H_0 = 25$ m (blue).

5.3.2 Sand grain size

The initial growth rates and evolution of crest height and trough depth for different sand grain sizes are shown in figure 5.12 (experiments 2D - 2F in table 4.3). The growth rate increases for larger grain sizes and so does the equilibrium time scale. For $d_{50} = 0.25$ mm, the equilibrium time scale for the crests is 110 years and for the troughs it is 90 years, whereas for $d_{50} = 0.35$ mm the values are 80 and 60 years, respectively. The grain size also affects the equilibrium height of the sand waves, which is 7.4 m for $d_{50} = 0.25$ mm and 9.1 m for $d_{50} = 0.35$ mm. The difference arises from differences in the crest height, as it is 1.7 m lower for $d_{50} = 0.25$ mm than for $d_{50} = 0.35$ mm.

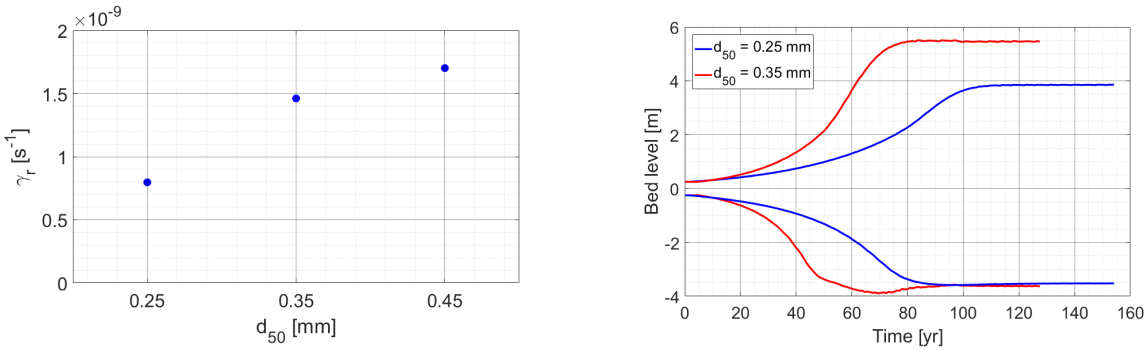

(A) (B)

FIGURE 5.12: (A) Initial growth rate γ_r for different values of the median grain size d_{50}. (B) Evolution of crest height and trough depth over time for $d_{50} = 0.25$ mm (red) and $d_{50} = 0.35$ mm (blue).

5.3.3 Bed slope parameter

The initial growth rates resulting from including different values of the bed slope parameter α_{bs} are shown in figure 5.13 (experiments 2G - 2J in table 4.3). The growth rate decreases for increasing values of α_{bs} and becomes negative for $\alpha_{bs} = 6$ and $\alpha_{bs} = 12$.

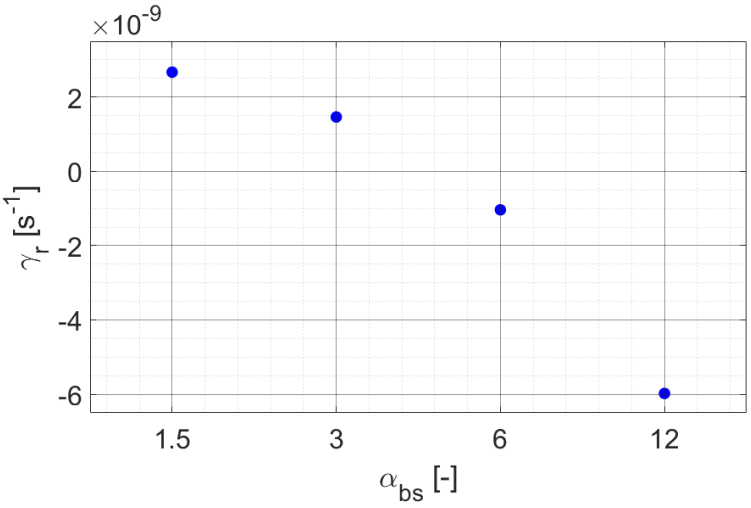

FIGURE 5.13: Initial growth rate γ_r for different values of the bed slope parameter α_{bs}.

5.3.4 Tidal forcing

Single tidal constituents

The initial growth rates for different imposed M_2 tidal current amplitudes (at the boundaries) are shown in figure 5.14a (experiments 2K - 2M in table 4.3). With respect to the default case ($M_2 = 0.6$ m s^{-1}), the initial growth rate γ_r for $M_2 = 0.5$ m s^{-1} decreases, but γ_r increases for $M_2 = 0.75$ m s^{-1}. Figure 5.14b shows the long term evolution of the trough depth and crest height for $M_2 = 0.6$ m s^{-1} and $M_2 = 0.75$ m s^{-1}. In case of the latter, the maximum bed level is in each year is shown. The sand waves slowly change their wavelength, to a new dominant wave length mode that matches the tidal forcing. This becomes clear in figure 5.14c. The growth and adjustment of the wavelength starts in the middle of the domain and gradually, the other sand waves change in a similar way, until the wavelength has changed from the initial 204 m to $\sim$ 1000 m. At the end of the simulation, the crests are almost 10 m high and the troughs are 14 m deep. The wiggles in the crest height are the result of instabilities, as the crest move slightly from left to right (figure 5.14c and see also figure 5.4b). The jumps in the trough depth are caused by the transition to a different sand wave that has become deeper. As both the maximum crest height and trough depth are still growing at the end of the simulation, these sand waves are not in equilibrium yet and will continue to grow.

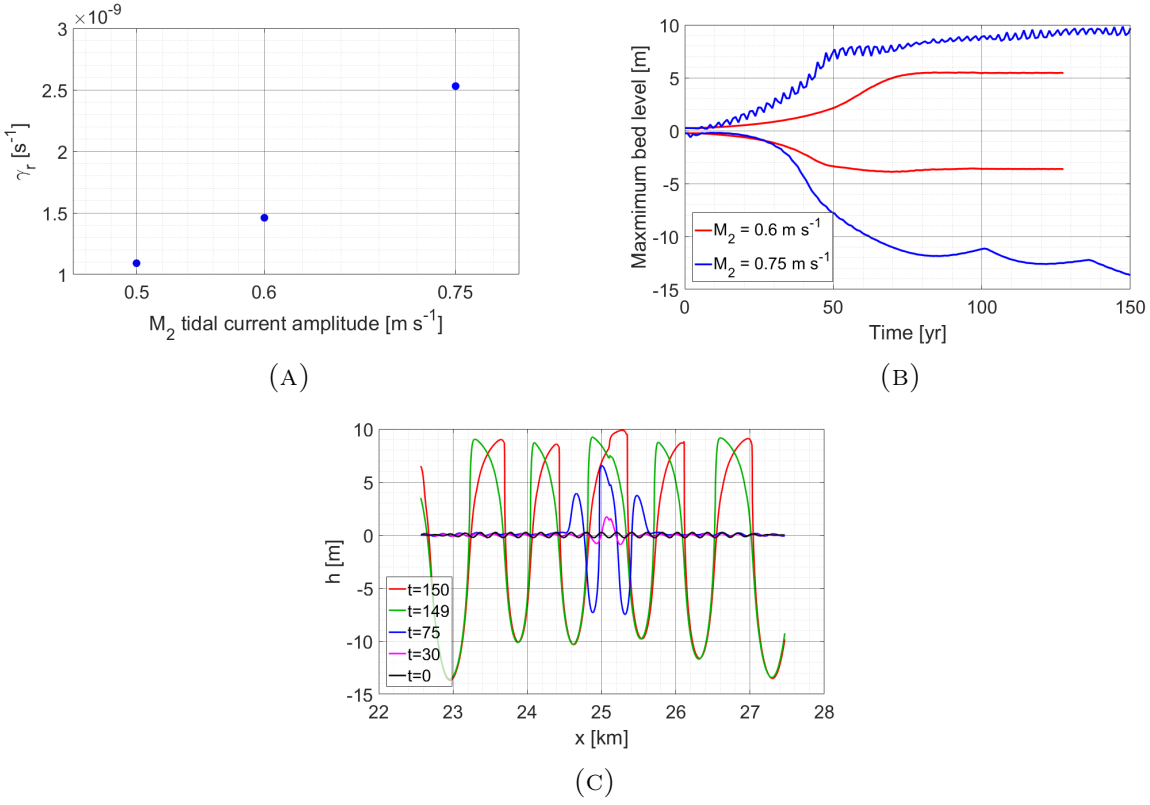

FIGURE 5.14: (A) Initial growth rate γ_r for different amplitudes of the M_2 tidal current imposed at the boundaries. (B) Evolution of crest height and trough depth over time for $M_2 = 0.6$ m s^{-1} (red) and $M_2 = 0.75$ m s^{-1} (blue). (C) Bed level at $t = 0$ (black), at $t = 30$ years (magenta), at $t = 75$ years (blue), at $t = 149$ years (green) and $t = 150$ years (red) for $M_2 = 0.75$ m s^{-1}.

Multiple tidal constituents

Adding the M_4 component to the M_2 tidal forcing mainly affects the migration of the sand waves, which becomes clear in figure 5.15a. This figure shows the initial growth and migration rates for different cases of phase difference θ (experiments 2N - 2P in table 4.3). The growth rates of all cases are approximately the same, but the migration rates are quite different. Including M_4 (with $\theta = 60°$), causes sand wave migration in the positive x-direction. However, for $\theta = 120°$ or $\theta = 180°$, the migration becomes negative, meaning that the sand waves migrate in the opposite direction.

Adding residual current M_0 to the M_2 tidal forcing (experiment 2Q in table 4.3), slightly reduces the initial growth rate and causes a migration into the positive x-direction. Then, adding M_4 with $\theta = 60°$ to the tidal forcing of 2Q (experiment 2R in table 4.3), further decreases the growth rate, but results in a higher migration than when only M_2 and M_4 or M_2 and M_0 are included.

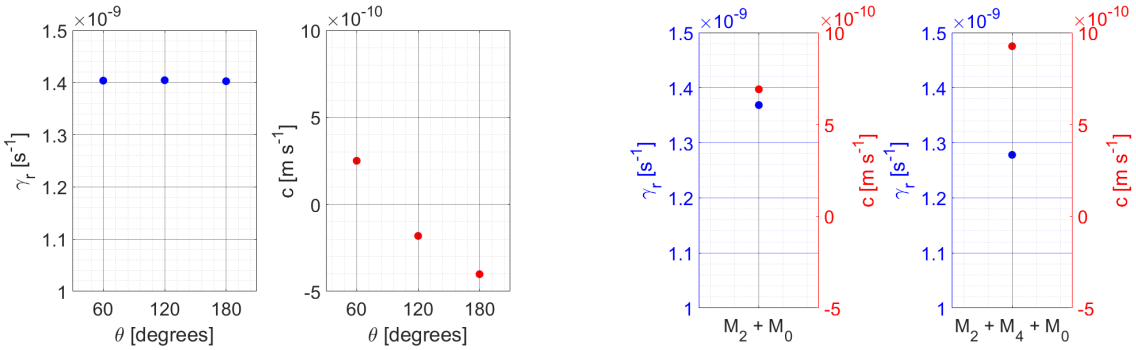

FIGURE 5.15: (A) Initial growth rate γ_r (left panel) and migration rate c (right panel) for different values of M_2-M_4 phase difference θ. (B) Initial growth rate γ_r (blue) and migration rate c (red) for a tidal forcing of M_2 and M_0 (left panel) and for a tidal forcing of M_2, M_4 and M_0 (right panel).

5.4 Application to HKZ data

The final set of experiments (experiments 3A - 3D in table 4.5) have the HKZ bathymetry as measured in 1999 as initial bed. Because these runs last for 17 years, the output can be compared with the measured bathymetry of 2016. In figure 5.16 the model results for each case are plotted together with the 2016 data (black). The measurements indicate that these sand waves migrated with a speed of 3 m year^{-1} in a north-easterly direction (which corresponds to the positive x-direction in figure 5.16). All the troughs became approximately 10 cm deeper and 5 of the 7 crests increased in height with a few centimeters. This resulted in a global growth rate σ of 1 mm year^{-1}. The shape and wavelength stayed the same over the period 1999-2016. Comparing the data with the model output, reveals that there are quite a few differences between the two. For example, for M_2-forcing only (second panel in figure 5.16), the sand waves do not migrate, but their shape changes as wiggles form on the left side of the crest and the crests tilt to the left, making the sand wave shape more symmetrical. Both the growth of the crests and troughs is positive and much higher than the data indicates. This is different when M_4 or M_0 is included in the tidal forcing (third panel in figure 5.16), because now the crests decrease in height, but the troughs become even deeper than for M_2 only. The inclusion of M_4 or M_0 causes the sand waves to migrate with a speed of approximately 15 m year^{-1}. This rate is increased to 30 m year^{-1} when both M_4 and M_0 are included, which can be seen in the fourth panel of figure 5.16. A combination of M_2, M_4 and M_0 causes a larger decrease of the crests but a smaller deepening of the troughs than when only M_4 or M_0 is used as tidal forcing.

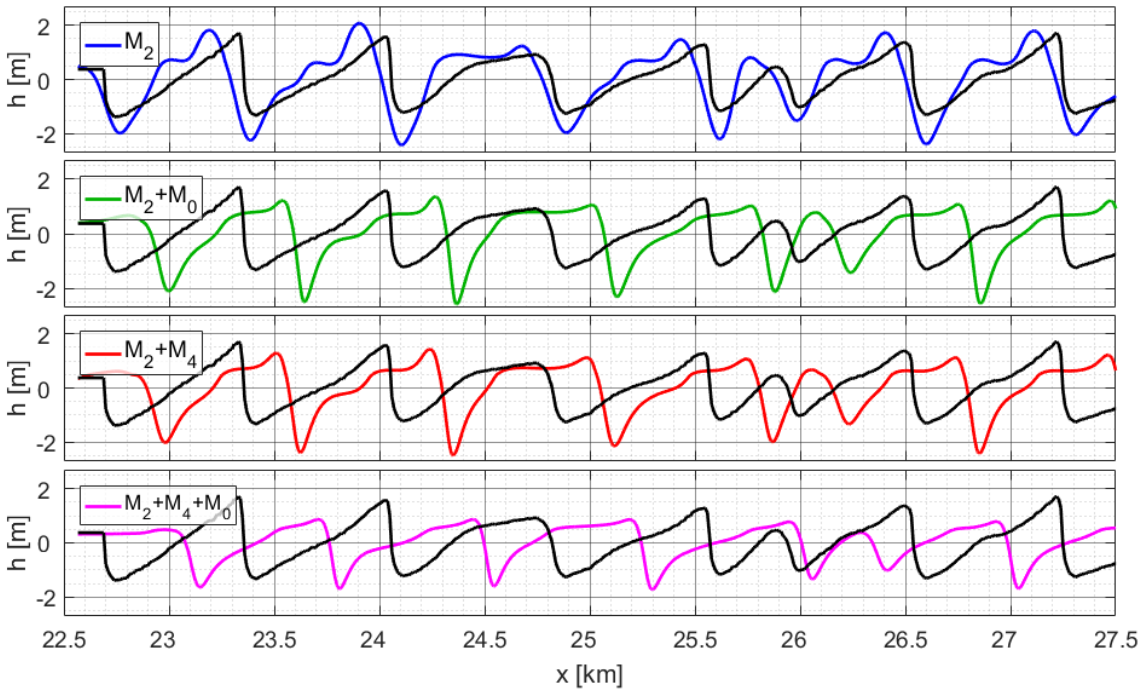

FIGURE 5.16: (A) The observed bed level in 2016 h_{obs} (2016) (black) and the modelled bed level in 2016 h_{mod} (2016) for a tidal forcing that consists of solely M_2 (blue). (B) as in (A), but h_{mod} (2016) for a tidal forcing of M_2 and M_0 (green). (C) as in (A), but h_{mod} (2016) for a tidal forcing of M_2 and M_4 (red). (D) as in (A), but h_{mod} (2016) for a tidal forcing of M_2, M_4 and M_0 (magenta).

The evolution of the crest height and trough depth over time for different cases of tidal forcing is shown in figure 5.17a and the observed and modelled position of these crest and troughs in 2016 is presented in figure 5.17b. The measured crest height in 2016 is 1.6 m and the trough depth 1.2 m, resulting in a wave height of 2.8 m. Forcing the model with M_2 results in a wave height of 4 m after 17 years. Including either M_4 or M_0 reduces the crest height with respect to a tidal forcing of M_2 only and it increases the trough depth in such a way that the wave height is also 4 m. The combined effect of M_4 and M_0 results in a lower crest height and trough depth, such that the wave height is 2.5 m, which is lower than the measured wave height of this sand wave. Using M_2 and M_0 or M_2 and M_4 forcing results in a modelled crest height that is close to the measured height, but is furthest removed from the measured trough depth. Including both M_4 and M_0 results in the best prediction of the trough depth, but then results in the worst prediction of the crest height. As in all cases the crests and troughs significantly change their height in only 17 years, suggests that the system is far from equilibrium.

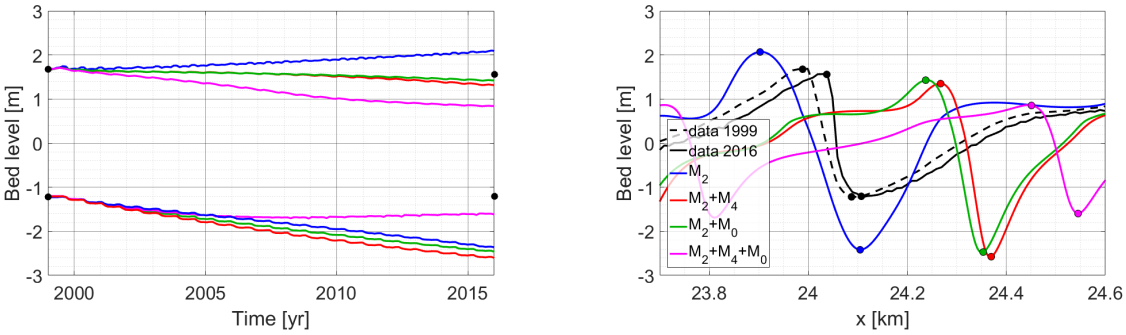

(A) (B)

FIGURE 5.17: (A) Evolution of crest height and trough depth over time for different cases of tidal forcing. (B) Position of modelled and observed crests and troughs in (A) at 2016.

Chapter 6

Discussion

6.1 Default case

The model settings in the default case are based on the settings by Van Gerwen et al. (2018), but the value of the morphological acceleration factor (MORFAC) and the hydrodynamic time Δt step are changed with respect to Van Gerwen et al. (2018). Here, the value of MORFAC was set to 500, based on the performed sensitivity study. Reducing the value of MORFAC to 250, resulted in differences in the saturation sand wave height of approximately 2%, but significantly increased the computation time with respect to MF=500. Increasing MORFAC to 1000 decreased to needed computation time, but lead to differences in the wave height of 5% and larger instabilities in the crest height. Therefore, MF=500 was selected. Van Gerwen et al. (2018) chose a value of 2000 for MORFAC, but this study showed that MF=2000 results in instabilities (oscillations in the crest height). In this study, Δt was 6 s and in the study of Van Gerwen et al. (2018) it was 12 s. In case of the latter, the solution became unstable.

Both this study and the study by Van Gerwen et al. (2018) show that the sand waves grow to be asymmetric, as the troughs have a different final shape than the crests (figure 5.4b). This is unexpected, since both the initial bed level and the tidal forcing are symmetric (i.e. the flood current is equal to the ebb current). Nonlinear effects cause the velocity at the bed to be slightly asymmetric and therefore, the residual sand transport at $t = 0$ is also asymmetric (figure 5.3b). The saturated sand waves move slightly from left to right (figure 5.4b), which is why the residual sand transport $\langle q_t \rangle$ is nonzero when the sand waves are in equilibrium. This also occurred when MF=250.

6.2 Sensitivity to numerical parameters

A limitation of the model presented in this study, is that it requires a large computational effort. Because of this, the sensitivity study into the numerical parameters, was done with MF=2000. As a result, small initial differences in the residual velocity and sand transport, can lead to large differences in the final bed level. Therefore, the differences between the equilibrium sand wave heights for the different cases presented in section 5.2 will be different for smaller values of MORFAC. As an extra check, short runs for

different values of Δx and Δt were performed without morphological updating in order to compare the initial differences in the residual velocity (figures B.4 and B.2). This showed that the difference between the residual velocities at the bed at $t = 0$ between $\Delta x = 2$ m en $\Delta x = 10$ m is 5%, which significantly affects the residual sand transport. The difference between $\langle u \rangle$ at $t = 0$ for $\Delta x = 2$ m and $\Delta x = 5$ m and for the differences between $\Delta x = 1.5$ s, $\Delta t = 3$ s with Δt =6 s were smaller (order 1%). For the amount of σ-layers only the initial formation was considered with MORFAC = 1, so here MORFAC has no influence.

6.3 Sensitivity to environmental parameters

Results (figure 5.11) showed that the initial growth rate decreases and the saturation time scale of sand waves increases for increasing values of the undisturbed water level H_0. For a decreasing water depth, residual velocity increases (figure B.5) and so does the bed shear stress and the residual bed load transport. For each of the cases of H_0 the residual bed shear stress $\langle \tau_b \rangle$ at $t = 0$ is shown in figure 6.1a and the residual bed load $\langle q_b \rangle$ (solid lines) and suspended load transport $\langle q_b \rangle$ (dashed lines) at $t = 0$ in figure 6.1b. The residual bed shear stress $\langle \tau_b \rangle$ is strongest for the lowest water depth ($H_0 = 21.5$ m) and this results in the highest residual bed load transport $\langle q_b \rangle$ as the two are related non-linearly. The residual suspended load transport $\langle q_s \rangle$ is the same for all three cases. The results for the initial growth rate is in agreement with the model results of Gerkema (2000), Van Santen et al. (2011) and Blondeaux and Vittori (2011), which revealed sand waves with larger wave lengths and smaller growth rates for deep water.

The saturation wave height is lower for $H_0 = 21.5$ m than for $H_0 = 25$ m. This matches with observations of lower wave heights in shallower water, as sand waves tend to have heights of up to 30% of the water depth (McCave (1971), Lanckneus and De Moor (1995),Flemming (2000) and Damen et al. (2018)). The initial higher residual velocity for $H_0 = 21.5$ m causes the sand waves to grow faster. During this growth, the velocity increases (figure 5.2), causing increasing rates of suspended load transport (figure 5.3). The latter is one of the processes causing saturation (Van Gerwen et al., 2018) and therefore leads to lower equilibrium sand wave heights. In other words, reducing the water depth increases both the processes of growth and saturation, but the latter is increased more strongly.

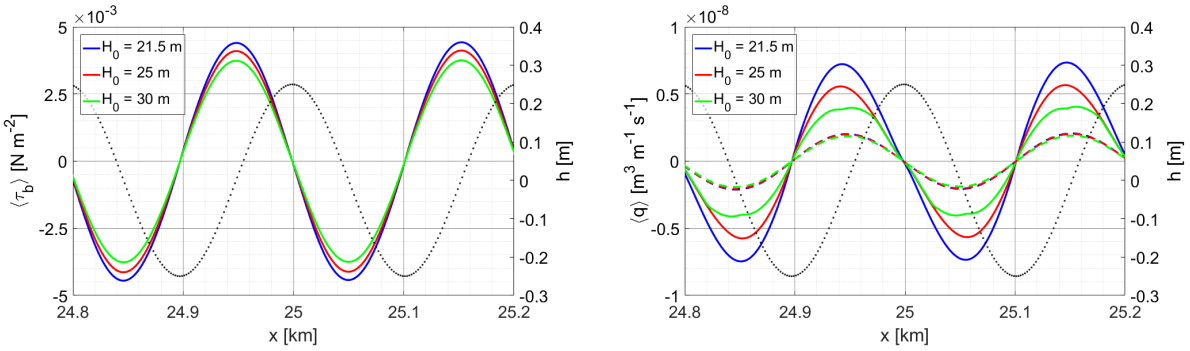

FIGURE 6.1: (A) The residual bed shear stress $\langle \tau_b \rangle$ at $t = 0$ for $H_0 = 21.5$ m (blue), $H_0 = 25$ m (red) and $H_0 = 30$ m (green). The black dotted line is h at $t = 0$ and corresponds to the right y-axis. (B) The residual bed load $\langle q_b \rangle$ (solid lines) and suspended load $\langle q_s \rangle$ (dashed lines) at $t = 0$ for different cases of H_0.

In the linear regime, the initial growth rate decreases for decreasing values of the median grain size d_{50} (figure 5.12), which is in agreement with some previous studies (Blondeaux and Vittori (2005a), Blondeaux and Vittori (2005b), Besio et al. (2006) and Van Gerwen et al. (2018)). However, the measurements analysed by Van Santen et al. (2011) did not show a clear relationship between grain size and growth rate. For smaller grain sizes, a larger portion of the sand is transported in suspension. This becomes clear in figure 6.2, which shows the residual bed load $\langle q_b \rangle$ (solid lines) and suspended load transport $\langle q_s \rangle$ (dashed lines) for different cases of d_{50}. Because the settling velocity increases for smaller grain sizes (equation 2.4), a lower value of d_{50} results in less sand available to be transported as bed load and more sand available for suspended load. Borsje et al. (2014) showed that suspended load transport has a damping effect on sand wave growth, because its tidal average $\langle q_s \rangle$ is 180° out of phase with $\langle q_b \rangle$ and therefore $\langle q_s \rangle$ causes a divergence of sand in the crest. However, this is dependent on the model settings and there are quite some differences in model set-up between this study and the one of Borsje et al. (2014), such as grid spacing, number of σ-layers, bed roughness, initial length and height. In addition to this, Campmans et al. (2017) showed that for a certain range of settings, the suspended transport does contribute positively to the growth. Here, the tidal average of the total volumetric sand transport (sum of $\langle q_b \rangle$ and $\langle q_s \rangle$) is smaller for smaller grain sizes (figure 6.2), explaining why the growth rate is smallest for $d_{50} = 0.25$ mm.

On the long term, a smaller value of d_{50} increases the equilibrium time scale and decreases the saturation wave height. During the sand wave growth, the residual velocity increases, which increases the amount of residual suspended load transport. In addition to this, the suspended sand particles are transported in increasingly larger parts of the water column. This enhances the balancing effect of suspended load transport on the sand wave growth and this effect is stronger for smaller grain sizes (see figure C.4). This explains why the saturation wave height decreases for $d_{50} = 0.25$ mm with respect to $d_{50} = 0.35$ mm.

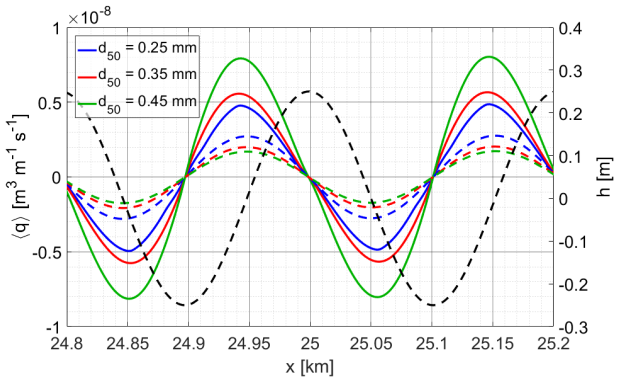

FIGURE 6.2: (A) The residual bed load $\langle q_b \rangle$ (solid lines) and suspended load $\langle q_s \rangle$ (dashed lines) transport for $d_{50} = 0.25$ mm (blue), $d_{50} = 0.35$ mm (red) and $d_{50} = 0.45$ mm (green). Black dotted line is the bathymetry.

The growth rate decreases for increasing values of the bed slope parameter α_{bs} (figure 5.13) and therefore for decreasing values of the angle of repose ϕ, as α_{bs} is inversely related to ϕ. The angle of repose determines how steep the slopes of the sand waves can get before avelanching occurs. The slope-induced part of the bed load transport is larger for larger values of α_{bs} and this counteracts the sand wave growth. Figure 6.3 shows the horizontal gradient of the residual bed load transport $\frac{\partial \langle q_b \rangle}{\partial x}$ for different cases of α_{bs}. For $\alpha_{bs} = 6$ and 12, the slope-induced transport is so large, that there is a net divergence of sand at the crest. This causes a decay of the sand wave and thus a negative growth rate. For $\alpha_{bs} = 1.5$ and 3, there is a net convergence of sand at the crest, which explains the positive growth rate. These results are in agreement with the study of Gerkema (2000), who also found smaller growth rates (and larger wavelengths) for a larger value of the bed slope parameter. In the future, also long term runs should be performed to investigate the effect of α_{bs} on the finite-amplitude behaviour of sand waves.

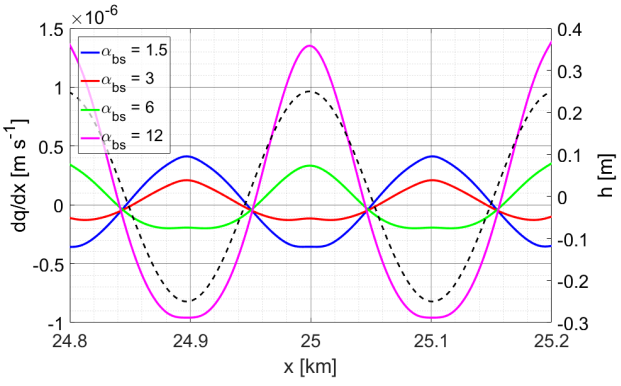

FIGURE 6.3: The horizontal gradient of the residual bed load transport $\frac{\partial \langle q_b \rangle}{\partial x}$ at $t = 0$ for $\alpha_{bs} = 1.5$ (blue), $\alpha_{bs} = 3$ (red), $\alpha_{bs} = 6$ (green) and $\alpha_{bs} = 12$ (magenta). Black dotted line is the bathymetry.

In the case that the amplitude of the M_2 tidal forcing is varied, a decrease of the growth rate is observed for a smaller amplitude and vice versa (figure 5.14). This is because a smaller (larger) M_2 leads to a decrease (increase) of the bottom stresses and the residual

velocity (both horizontal and vertical, see appendix B). Therefore, the residual sand transport also decreases (increases) which in turn affects the growth rate. Besio et al. (2003) and Van Santen et al. (2011) found the same relationship between tidal current amplitude and growth rate. In the long term, imposing $M_2 = 0.75$ m s^{-1} led to a wave length of ∼1000 m and a wave height of ∼20 m at $t = 150$ years. This is much larger than the equilibrium wave length of 204 m and equilibrium wave height of 9.2 m resulting from a tidal forcing of $M_2 = 0.6$ m s^{-1}. In the case of $M_2 = 0.75$ m s^{-1}, the sand waves are still growing at the end of the simulation. Even though an M_2 amplitude of 0.75 m s^{-1} is quite high, it has been observed in the North Sea in areas where sand waves occur (Borsje et al., 2009). The large growth suggests that some key balancing mechanisms are missing in the model, which becomes especially important for larger M_2 amplitudes. For example, Van Gerwen et al. (2018) showed that the introduction of a residual current results in lower values of the saturation wave height and Campmans et al. (2018) showed that the effect of storms reduce the wave height.

In the linear regime, including other tidal constituents such as a residual current M_0 or M_4 only has a small effect on the growth rate, but causes the sand waves to migrate (figure 5.15). The migration direction depends on the direction of M_0 and the phase shift θ between M_2 and M_4. The latter, especially, should be treated with care, as increasing θ from 60° to 120° resulted in migration in the opposite direction. The reason is that the tidal velocity becomes asymmetric in time, in the sense that the peak flood current is not equal to the peak ebb current. For $\theta = 60°$, the maximum flood velocity is higher than the maximum ebb velocity, but the ebb phase spans a longer time period than the flood phase. As a result, the horizontal residual velocity has a higher magnitude on the left side of the crest than on the right, but the left part of $\langle u \rangle$ spans a larger area (figure 6.4a). In other words, the residual circulation cells have become asymmetrical with respect to the bed. This moves the area of maximum convergence of sand towards the right side of the crest, which results in sand wave migration. This can be seen in figure 6.4b, where the horizontal gradient of the residual sand transport is shown at $t = 0$ for the bathymetry as in the default case. The exact opposite is true when $\theta = 120°$. Adding M_0 to the tidal forcing of M_2 and M_4 with $\theta = 60°$, reduces the growth rate, but enhances the migration increases. These results agree with these of Németh et al. (2002), Besio et al. (2004), Borsje et al. (2013) and Blondeaux and Vittori (2016), as in all these studies the inclusion of M_4 or M_0 resulted in small changes in the growth rates, but in migration rates depending on M_0 and θ. Besio et al. (2004) found that the value of θ is especially important, because it can overcome the migration induced by M_0 when both M_4 and M_0 are included.

Van Gerwen et al. (2018) investigated the effect of including a residual current M_0 on the finite amplitude behaviour. They showed that the saturation wave height decreased due to M_0 and that M_0 induced a migration of the sand waves in the direction of M_0. Both effects increased for increasing values of M_0.

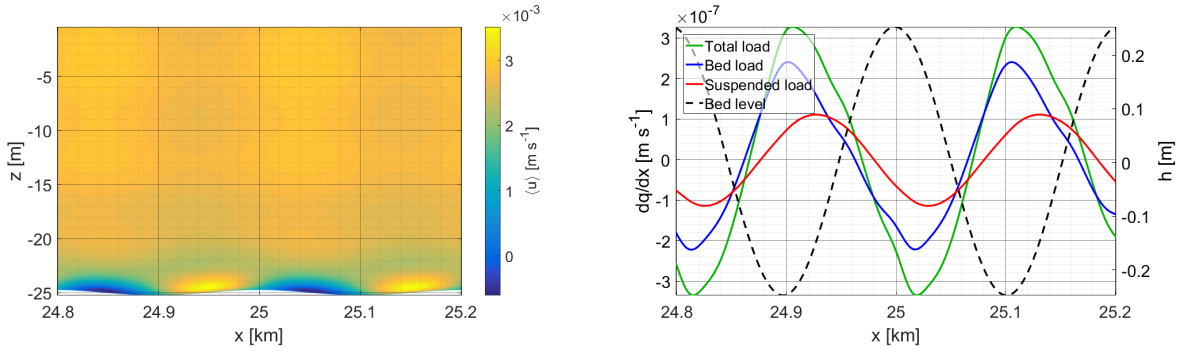

(A) (B)

FIGURE 6.4: (A) Horizontal component of the residual velocity $\langle u \rangle$ for a tidal forcing of M_2 and M_4 with $\theta = 60°$ for the bathymetry as in the default case at $t = 0$. (B) Horizontal gradient of residual sand transport $\frac{\partial \langle q_b \rangle}{\partial x}$ (blue), $\frac{\partial \langle q_s \rangle}{\partial x}$ (red) and $\frac{\partial \langle q_t \rangle}{\partial x}$ (green). Black dotted line is the bathymetry.

6.4 Simulation of HKZ

There is a clear mismatch between the measured bed level of 2016 and the modelled bed level, when the observed bathymetry of 1999 is used as model input (figure 5.16). Remarkably, forcing the model with M_2 and M_0 or with M_2 and M_4 gave almost the same output. This is a coincidence, as Van Gerwen et al. (2018) showed that both the migration and the saturation wave height are very sensitive to the value of M_0. Including both M_4 and M_0 enhances the migration, which was also the case in the linear regime. The migration rate (resulting from M_2, M_4 and M_0 tidal forcing) is over-predicted, as the data showed that the sand waves migrated but 3 m year$^-$1, but the modelled migration was 30 m year$^-$1. The modelled bed level shows a decrease in the crest heights and increase of trough depths of up to 1 m, while data reveals that there is hardly any change in trough depth and crest height over time. These differences have three origins: 1) the model set-up, 2) uncertainties in the tidal forcing and 3) from processes that are still missing in the model.

First of all, using a morphological acceleration factor results in errors in both the wave height and migration rate. Reducing this value will improve the results. Initially, reducing time step Δt would lead to differences in the residual velocity of the order 1%. Besides this, the model results are quite sensitive to the chosen type of lateral boundary conditions. If the same run was performed, but instead of Riemann invariants, a combination of water level boundary conditions and Neumann water level gradients are imposed. For this, ζ was imposed at $x = 0$ and $x = L_x$ (table 4.4) and on the sea ward boundary an alongshore water level gradient ($\frac{\partial \zeta}{\partial x}$) was imposed (for details see appendix D). As it turns out, no residual circulation cells form and the sand waves decay and do not migrate. Therefore, imposing lateral boundary conditions different than Riemann or Neumann, might alter the results.

Uncertainties in the tidal forcing result from the fact that the output of the Dutch Continental Shelf model was used to force the flow. This might not match completely with the tidal forces actually at work in the HKZ area. Even though DSMv6 is verified extensively against data (Zijl et al., 2013), there are still uncertainties in the output. The tide gauge

data from stations at Scheveningen and IJmuiden, showed that the modelled water level amplitude of M_2 and M_4 is over-predicted by several centimeters. This would mean that the bed shear stress is underpredicted and that the sand transport is actually lower. This does not explain the overprediction of the migration rate.

Besides this, there were differences between the modelled and observed phases of M_2 and M_4 of 15° . As the migration is very sensitive to the phase difference between M_2 and M_4, this could significantly affect the migration rate. At the same time, errors arise from using T-TIDE to analyse the velocity time series. For the major tidal constituents the error in the amplitude can be up to 5%. The error in the M_2 phase is of the same order, but for the error in the M_4 phase can be up to 20% (Pawlowicz et al., 2002). Since the model results were quite sensitive to different values of M_2 and θ, errors in these quantities could cause differences between the modelled and observed migration rates. In addition to this, the results by Sterlini et al. (2009) indicated that the magnitude of the tidal current, together with the water depth, were the most important parameters to determine the saturation wave height and length, suggesting that a more accurate representation of the HKZ tidal current, could resolve the issues regarding the height of the sand waves. To achieve this, measurements of either velocity or water level in the HKZ area are needed.

Simulations regarding HKZ were done with M_2, M_4 and M_0. Van de Kreeke and Robaczewska (1993) showed that a combination of these constituents is sufficient to explain the patterns of residual sand load transport. Sterlini et al. (2009) showed that a combination of M_2 and M_0 was sufficient to model the basic dimensions of sand waves in the San Fransisco Bay, but their study did not focus on migration rates. However, other constituents might still have an effect. For example, Blondeaux and Vittori (2010) showed that the spring-neap cycle (superposition of S_2 and M_2) can significantly influence the sand waves during the stages of initial formation. In addition to this, observations by Ferret et al. (2010) indicated that sand wave shape and migration varied with a periodicity of ∼18 years. This periodicity was related to the 18.6 lunar nodal cycle which affects tidal amplitudes. The effects of this long term cyclicity and other tidal constituents such as S_2 on sand wave evolution have not been studied in model studies so far, but including these might improve the model results. However, this would require a significantly smaller values of MORFAC to achieve the same accuracy.

One of the missing processes, is the effect of multiple grain sizes. In this model the median grain size is assumed to be the same everywhere in the domain, while measurements by the survey service Fugro showed that d_{50} varies between 0.25 mm and 0.3 mm along the transect. Measurements at other locations in the North Sea indicate that sorting patterns are observed along sand waves (see e.g. Roos et al. (2007)). Van Oyen and Blondeaux (2009a) showed that sorting patterns can significantly affect the initial formation of sand waves. Including a spatially variable d_{50} could improve the predictions, as the simulations with different values of d_{50} showed that both the saturation time scale and the saturation crest height are affected by the value of d_{50}. The saturation trough depth was not affected as strongly.

To conclude, the migration rate could be improved by reducing MORFAC and Δt and by a further study of the boundary conditions. Improvement could also be achieved changing the amplitudes and especially the phases of the tidal constituents used as tidal forcing, for example by using measurements in the HKZ area itself. Finally, the difference in wave height and migration rate suggest that some processes are missing in the model. The most

important ones are the effect of wind and waves and the effects of sand characteristics. Including these will improve the modelled migration rate. The missing processes are listed in the next section, where the model limitations and the suggestions for future research are discussed.

6.5 Limitations and recommendations

In this section, five limitations and accompanying recommendations will be discussed. The first limitation is that the model results are sensitive to the chosen type of lateral boundary conditions. In this study Riemann invariants were used, but further study is necessary to investigate other types of boundary conditions.

The second limitation is that a large computational effort is needed to study the saturation behaviour of sand waves with this model. To speed up the computation time, a morphological acceleration factor was implemented, but this introduces errors. To increase better accuracy, a time-dependent MORFAC could be included, i.e. a smaller value of MORFAC in the initial stages of formation and larger once the sand waves reaching equilibrium.

In this model, only tidal forcing is taken into account. However, observational studies show that wind, waves and storms can significantly affect the evolution of sand waves by reducing the wave height (Terwindt (1971), McCave (1971), Houthuys et al. (1994) and Van Dijk and Kleinhans (2005)) and by enhancing or opposing the migration (Bokuniewicz et al. (1977), Harris (1989), Fenster et al. (1990), Le Bot et al. (2000) and Ferret et al. (2010)). This was also shown in idealized model studies (Campmans et al. (2017) and Campmans et al. (2018)). The effect of wind, waves and storms has not yet been considered in complex model studies and this remains to be done.

In this model, the median grain size is assumed to be the same everywhere, but observations show that this is not realistic (e.g. Roos et al. (2007)). Therefore, grain sorting patterns should be included.

Finally, sand waves are a three dimensional phenomenon (see figure on the front page) and in this study one horizontal dimension is left out. Blondeaux and Vittori (2009) included the weakly non-linear interaction between different modes. With this they were able to simulate the initial formation of 3D sand waves in highly idealized model, but they did not study the saturation of 3D sand waves. This could be investigated using Delft3D.

Chapter 7

Conclusions

The first aim of this study was to investigate the sensitivity of the model results by Van Gerwen et al. (2018) to several numerical parameters. This concerns the non-linear dynamics in two dimensions (one horizontal and the vertical direction) of sand waves with initially small amplitudes relative to the mean water depth. Overall, the model results proved to be quite sensitive to changes in these parameters. First, different values of the morphological acceleration factor were implemented. For values ranging between 250-2000 the results were qualitatively the same, except for oscillations in crest height. These oscillations were only present for MORFAC = 2000 and therefore the result of errors. Secondly, the hydrodynamic time step was increased from 1.5 s to 12 s. The differences between the results were small, but $\Delta t = 12$ s proved to be too large for this grid. Choosing a sufficient number of σ-layers is very important, because the processes close to the bed need to be resolved with sufficient resolution. Therefore, there are large differences between the results with different amounts of σ-layers. The same holds for the horizontal grid spacing Δx, which needs to be small enough to compute small variations in the residual velocity field. Hence, the set of numerical parameters used should be selected with care in order to make sure that model results are not influenced by these parameters.

Secondly, this study looked into the sensitivity of the evolution of sand waves to different environmental parameters. Sand waves react quite strongly to changes in environmental parameters. Reducing the undisturbed water level H_0, for example, leads to an increase of the growth rate in the short term and a decrease of the saturation time scale in the long term. This is caused by higher bed shear stresses in shallower water. The saturation wave height decreases for decreasing values of H_0, because the processes governing saturation are increased more than the growth. Subsequently, increasing the median grain size d_{50}, increases the growth rate and the saturation wave height and decreases the saturation time scale. The explanation for this is that the total volumetric sand transport increases for smaller grains. Next, there is a clear relation between the value of the bed slope parameter α_{bs} and the initial growth rate of sand waves: the larger α_{bs}, the smaller the growth rate. This is because α_{bs} is inversely related to the angle of repose. As a smaller angle of repose is more easily exceeded, slope induced transport plays an important role, which reduces the sand wave growth. Finally, the study showed that increasing the value of the M_2 tidal current amplitude imposed at the lateral boundaries of the domain, increases the growth rate and the saturation timescale, wave height and wave length significantly, as the sand

waves move to a different mode. Finally, the phase difference θ between M_2 and M_4 is crucial, because a shift of can change the magnitude and direction of the migration.

The third and final part of this study was to apply the model to an observed sand wave field in the HKZ area. The modelled migration of crests and troughs was much larger than observed, and both the crest height decreased and the trough depth increased, even though the data suggests almost no change. Therefore, this model is not yet ready for practical application. There are several improvements that could be made, such as including a spatially variable d_{50}, changing the boundary conditions based on measurements, including the effect of wind and waves and taking into account 3D effects. Including these processes to improve the model is a necessary step to help understand long term sand wave movements in shallow coastal seas. This will also make it possible to use the model to determine optimal burial depths of cables accompanying offshore wind farms.

Bibliography

Aliotta, S. and Perillo, G. M. E. (1987). A sand wave field in the entrance to Bahia Blanca estuary, Argentina. *Marine Geology*, 76:1–14.

Barnard, P. L., Hanes, D. M., Rubin, D. M., and Kvitek, R. G. (2006). Giant sand waves at the mouth of San Francisco Bay. *Eos, Transactions American Geophysical Union*, 87(29):285–289.

Besio, G., Blondeaux, P., Brocchini, M., Hulscher, S. J., Idier, D., Knaapen, M. A., Németh., A. A., Roos, P. C., and Vittori, G. (2008). The morphodynamics of tidal sand waves: A model overview. *Coastal Engineering*, 55(7-8):657–670.

Besio, G., Blondeaux, P., Brocchini, M., and Vittori, G. (2004). On the modeling of sand wave migration. *Journal of Geophysical Research: Oceans*, 109(C4).

Besio, G., Blondeaux, P., and Frisina, P. (2003). A note on tidally generated sand waves. *Journal of Fluid Mechanics*, 485:171–190.

Besio, G., Blondeaux, P., and Vittori, G. (2006). On the formation of sand waves and sand banks. *Journal of Fluid Mechanics*, 557:1–27.

Blondeaux, P. and Vittori, G. (2005a). Flow and sediment transport induced by tide propagation: 1. the flat bottom case. *Journal of Geophysical Research: Oceans*, 110(C7). doi:10.1029/2004JC002532.

Blondeaux, P. and Vittori, G. (2005b). Flow and sediment transport induced by tide propagation: 2. the wavy bottom case. *Journal of Geophysical Research: Oceans*, 110(C8). doi:10.1029/2004JC002545.

Blondeaux, P. and Vittori, G. (2009). Three-dimensional tidal sand waves. *Journal of Fluid Mechanics*, 618:1–11.

Blondeaux, P. and Vittori, G. (2010). Formation of tidal sand waves: Effects of the spring-neap cycle. *Journal of Geophysical Research: Oceans*, 115(C10).

Blondeaux, P. and Vittori, G. (2011). The formation of tidal sand waves: Fully three-dimensional versus shallow water approaches. *Continental Shelf Research*, 31(9):990–996.

Blondeaux, P. and Vittori, G. (2016). A model to predict the migration of sand waves in shallow tidal seas. *Continental Shelf Research*, 112:31–45.

Bokuniewicz, H., Gordon, R., and Kastens, K. (1977). From and migration of sand waves in a large estuary, Long Island Sound. *Marine Geology*, 24(3):185–199.

Borsje, B. W., de Vries, M. B., Bouma, T. J., Besio, G., Hulscher, S. J. M. H., and Herman, P. M. J. (2009). Modeling bio-geomorphological influences for offshore sandwaves. *Continental Shelf Research*, 29(9):1289–1301.

Borsje, B. W., Kranenburg, W. M., Roos, P. C., Matthieu, J., and Hulscher, S. J. M. H. (2014). The role of suspended load transport in the occurrence of tidal sand waves. *Journal of Geophysical Research: Earth Surface*, 119(4):701–716.

Borsje, B. W., Roos, P. C., Kranenburg, W. M., and Hulscher, S. J. M. H. (2013). Modeling tidal sand wave formation in a numerical shallow water model: The role of turbulence formulation. *Continental Shelf Research*, 60:17–27.

Burchard, H., Craig, P. D., Gemmrich, J. R., van Haren, H., Mathieu, P.-P., Meier, H. M., Smith, W. A. M. N., Prandke, H., Rippeth, T. P., Skyllingstad, E. D., et al. (2008). Observational and numerical modeling methods for quantifying coastal ocean turbulence and mixing. *Progress in oceanography*, 76(4):399–442.

Campmans, G., Roos, P., de Vriend, H., and Hulscher, S. (2018). The influence of storms on sand wave evolution: a nonlinear idealized modeling approach. *Journal of Geophysical Research: Earth Surface*. doi: 10.1029/2018jf004616.

Campmans, G. H., Roos, P. C., de Vriend, H. J., and Hulscher, S. J. (2017). Modeling the influence of storms on sand wave formation: A linear stability approach. *Continental shelf research*, 137:103–116.

Cushman-Roisin, B. and Beckers, J.-M. (2011). *Introduction to geophysical fluid dynamics: physical and numerical aspects*, volume 101. Academic Press.

Damen, J. M., Van Dijk, T. A. G. P., and Hulscher, S. J. M. H. (2018). Spatially Varying Environmental Properties Controlling Observed Sand Wave Morphology. *Journal of Geophysical Research: Earth Surface*, 123(2):262–280.

Deigaard, R. and Fredsœ, J. (1992). *Mechanics of coastal sediment transport*, volume 3. World scientific publishing company, Advanced series of Ocean Engineering.

Deltares (2013). User manual Delft-3D FLOW. Technical report, Deltares, Delft.

Dodd, N., Falqués, A., Hulscher, S. J. M. H., Rózynski, G., Vittori, G., Blondeaux, P., Calvete, D., and De Swart, H. E. (2003). Understanding coastal morphodynamics using stability methods. *Journal of Coastal Research*, 19(May 2014):849–865.

Duffy, G. P. and Hughes-Clarke, J. E. (2005). Application of spatial cross correlation to detection of migration of submarine sand dunes. *Journal of Geophysical Research: Earth Surface*, 110(F4).

Dyer, K. (1986). Coastal and estuarine sediment dynamics. *John Wiley and Sons, Chichester, Sussex (UK), 358*.

Dyer, K. R. and Huntley, D. A. (1999). The origin, classification and modelling of sand banks and ridges. *Continental Shelf Research*, 19(10):1285–1330.

Fenster, M. S., Fitzgerald, D. M., Bohlen, W. F., Lewis, R. S., and Baldwin, C. T. (1990). Stability of giant sand waves in eastern Long Island Sound, USA. *Marine Geology*, 91(3):207–225.

Ferret, Y., Le Bot, S., Tessier, B., Garlan, T., and Lafite, R. (2010). Migration and internal architecture of marine dunes in the eastern English Channel over 14 and 56 year intervals: the influence of tides and decennial storms. *Earth Surface Processes and Landforms*, 35(12):1480–1493.

Flemming, B. (2000). The role of grain size, water depth and flow velocity as scaling factors controlling the size of subaqueous dunes. In *Marine sandwave dynamics, international workshop*, pages 23–24.

Garnier, R., Calvete, D., Falqués, A., and Caballeria, M. (2006). Generation and nonlinear evolution of shore-oblique/transverse sand bars. *Journal of Fluid Mechanics*, 567:327–360.

Gerkema, T. (2000). A linear stability analysis of tidally generated sand waves. *Journal of Fluid Mechanics*, 417:303–322.

Groen, P. (1967). On the residual transport of suspended matter by an alternating tidal current. *Netherlands Journal of Sea Research*, 3(4):564–574.

Harris, P. T. (1989). Sandwave movement under tidal and wind-driven currents in a shallow marine environment: Adolphus Channel, northeastern Australia. *Continental Shelf Research*, 9(11):981–1002.

Heip, C., Basford, D., Craeymeersch, J., Dewarumez, J., Dörjes, J., De Wilde, P., Duineveld, G., Eleftheriou, A., Herman, P., Niermann, U., Kingston, P., Kiinitzer, A., Rachor, E., Rumohr, H., Soetaert, K., and Soltwedel, T. (1992). Trends in biomass, density and diversity of North Sea macrofauna. *ICES Journal of Marine Science*, 49(1):13–22.

Houthuys, R., Trentesaux, A., and De Wolf, P. (1994). Storm influences on a tidal sandbank's surface (Middelkerke Bank, southern North Sea). *Marine Geology*, 121(1-2):23–41.

Hulscher, S. J., de Swart, H. E., and de Vriend, H. J. (1993). The generation of offshore tidal sand banks and sand waves. *Continental Shelf Research*, 13(11):1183–1204.

Hulscher, S. J. M. H. (1996). Tidal-induced large-scale regular bed form patterns in a three-dimensional shallow water model. *Journal of Geophysical Research*, 101(20):727–744.

Knaapen, M. A. F. and Hulscher, S. J. M. H. (2002). Regeneration of sand waves after dredging. *Coastal Engineering*, 46(4):277–289.

Komarova, N. L. and Hulscher, S. J. M. H. (2000). Linear instability mechanisms for sand wave formation. *Journal of Fluid Mechanics*, 413:219–246.

Künitzer, A., Basford, D., Craeymeersch, J., Dewarumez, J., Dörjes, J., Duineveld, G., Eleftheriou, A., Heip, C., Herman, P., Kingston, P., et al. (1992). The benthic infauna of the North Sea: species distribution and assemblages. *ICES Journal of Marine Science*, 49(2):127–143.

Lanckneus, J. and De Moor, G. (1995). Bedforms on the middelkerke bank, southern north sea. In *Tidal signatures in modern and ancient sediments*, volume 24, pages 33–51. Blackwell Science Oxford.

Lankneus, J. and Moor, G. (1991). Present-day evolution of sand waves on a sandy shelf bank. *Oceanologica Acta, Special issue*, 11:123–127.

Le Bot, S., Idier, D., Garlan, T., Trentesaux, A., and Astruc, D. (2000). Dune dynamics: from field measurements to numerical modelling. Application to bathymetric survey frequency in the Calais-Dover Strait. pages 101–108. In: Trentesaux, A., Garlan, T. (Eds.), Proceedings of the International Workshop on Marine Sand Dynamics, Lille, France. University of Lille, Lille, France.

Lesser, G., Roelvink, J. v., Van Kester, J., and Stelling, G. (2004). Development and validation of a three-dimensional morphological model. *Coastal Engineering*, 51(8-9):883–915.

Liao, H.-R. and Yu, H.-S. (2005). Morphology, hydrodynamics anti sediment characteristics of the Changyun Sand Ridge offshore western Taiwan. *Terrestrial, Atmospheric and Oceanic Sciences*, 16(3):621–640.

Masselink, G., Hughes, M., and Knight, J. (2014). *Introduction to coastal processes and geomorphology*. Routledge.

McCave, I. N. (1971). Sand waves in the North Sea off the coast of Holland. *Marine Geology*, 10(3):199–225.

Nemeth, A., Hulscher, S. J., and De Vriend, H. J. (2003). Offshore sand wave dynamics, engineering problems and future solutions. *Pipeline and Gas Journal*, 230(4):67–69.

Németh, A. A., Hulscher, S. J. M. H., and De Vriend, H. J. (2002). Modelling sand wave migration in shallow shelf seas. *Continental Shelf Research*, 22:2795–2806.

Németh, A. A., Hulscher, S. J. M. H., and Van Damme, R. M. J. (2007). Modelling offshore sand wave evolution. *Continental Shelf Research*, 27(5):713–728.

Noordzeeloket (2017). Windenergiegebieden huidige routekaart. https://www.noordzeeloket.nl/functies-en-gebruik/windenergie/windenergiegebieden/. [Online; accessed 19-May-2018].

Pawlowicz, R., Beardsley, B., and Lentz, S. (2002). Classical tidal harmonic analysis including error estimates in MATLAB using T_TIDE. *Computers & Geosciences*, 28(8):929–937.

Press, W. H., Teukolsky, S. A., Vetterling, W. T., and Flannery, B. P. (1988). Numerical recipes in C. *Cambridge University Press*, 1:3.

Rabaut, M., Guilini, K., Van Hoey, G., Vincx, M., and Degraer, S. (2007). A bio-engineered soft-bottom environment: the impact of Lanice conchilega on the benthic species-specific densities and community structure. *Estuarine, Coastal and Shelf Science*, 75(4):525–536.

Ranasinghe, R., Swinkels, C., Luijendijk, A., Roelvink, D.and Bosboom, J., Stive, M., and Walstra, D. J. (2011). Morphodynamic upscaling with the MORFAC approach: Dependencies and sensitivities. *Coastal Engineering*, 58(8):806–811.

Reineck, H., Singh, I., and Wunderlich, F. (1971). Einteilung der Rippeln und anderer mariner Sandkörper. *Senckenbergiana Maritima*, 3:93–101.

Rijksoverheid (2018). Windenergie op zee. https://www.rijksoverheid.nl/onderwerpen/duurzame-energie/windenergie-op-zee. [Online; accessed 20-June-2018].

Rodi, W. (1984). Turbulence models and their application in hydrodynamics - a state of the art review. Technical report, University of Karlsruhe, Germany.

Roetert, T. J. (2014). Optimization of offshore wind farm power cable routing. Master's thesis, University of Twente, The Netherlands.

Roos, P. C., Hulscher, S., Van Der Meer, F., Van Dijk, T., Wientjes, I. G., and van den Berg, J. (2007). Grain size sorting over offshore sandwaves: observations and modelling. In *5th IAHR Symposium on River, Coastal and Estuarine Morphodynamics, Twente*. University of Twente, The Netherlands.

Roos, P. C., Hulscher, S. J. M. H., Meer, F. V. D., and Wientjes, I. G. M. (2008). Grain size sorting over offshore sandwaves : Observations and modelling. *Built Environment*, (Hirano 1971):649–656.

Sekine, M. and Parker, G. (1992). Bed-load transport on transverse slope. I. *Journal of Hydraulic Engineering*, 118(4):513–535.

Shields, A. (1936). *Anwendung der Aehnlichkeitsmechanik und der Turbulenzforschung auf die Geschiebebewegung*. PhD thesis, Technical University Berlin. Preussischen Versuchsanstalt für Wasserbau.

Soulsby, R. (1997). *Dynamics of marine sands: a manual for practical applications*. Thomas Telford.

Sterlini, F., Hulscher, S. J. M. H., and Hanes, D. M. (2009). Simulating and understanding sand wave variation: A case study of the Golden Gate sand waves. *Journal of Geophysical Research: Earth Surface*, 114(2):1–15.

Swift, D. J., Parker, G., Lanfredi, N. W., Perillo, G., and Figge, K. (1978). Shoreface-connected sand ridges on American and European shelves: a comparison. *Estuarine and Coastal Marine Science*, 7(3):257–273.

Terwindt, J. H. (1971). Sand waves in the Southern Bight of the North Sea. *Marine Geology*, 10(1):51–67.

Van de Kreeke, J. and Robaczewska, K. (1993). Tide-induced residual transport of coarse sediment; application to the Ems estuary. *Netherlands Journal of Sea Research*, 31(3):209–220.

Van den Berg, J., Sterlini, F., Hulscher, S. J. M. H., and Van Damme, R. (2012). Non-linear process based modelling of offshore sand waves. *Continental Shelf Research*, 37:26–35.

Van Dijk, T. A. and Kleinhans, M. G. (2005). Processes controlling the dynamics of compound sand waves in the North Sea, Netherlands. *Journal of Geophysical Research: Earth Surface*, 110(F4). doi: 10.1029/2004JF000173.

Van Dijk, T. A. G. P., Lindenbergh, R. C., and Egberts, P. J. P. (2008). Separating bathymetric data representing multiscale rhythmic bed forms: A geostatistical and spectral method compared. *Journal of Geophysical Research: Earth Surface*, 113(4):1–16.

Van Gerwen, W., Borsje, B. W., Damveld, J. H., and Hulscher, S. J. (2018). Modelling the effect of suspended load transport and tidal asymmetry on the equilibrium tidal sand wave height. *Coastal Engineering*, 136:56–64.

Van Oyen, T. and Blondeaux, P. (2009a). Grain sorting effects on the formation of tidal sand waves. *Journal of Fluid Mechanics*, 629:311–342.

Van Oyen, T. and Blondeaux, P. (2009b). Tidal sand wave formation: Influence of graded suspended sediment transport. *Journal of Geophysical Research: Oceans*, 114(C7). doi:10.1029/2008JC005136.

Van Rijn, L, C. (1993). *Principles of sediment transport in rivers, estuaries and coastal seas*. Aqua Publishers, the Netherlands.

Van Santen, R. B., De Swart, H. E., and Van Dijk, T. A. (2011). Sensitivity of tidal sand wavelength to environmental parameters: A combined data analysis and modelling approach. *Continental Shelf Research*, 31(9):966–978.

Veritas (2014). Subsea power cables in shallow water renewable energy applications. Det Norske Veritas Report DNV-RP-J301, Høvik, Norway, http://www.dnv.com.

Vis-Star, N. C., de Swart, H., and Calvete, D. (2008). Patch behaviour and predictability properties of modelled finite-amplitude sand ridges on the inner shelf. *Nonlinear Processes in Geophysics*, 15(6):943.

Wilson, J. and Stride, A. (1982). Offshore tidal sands: processes and deposits.

Wolters-Noordhoff (2005). *De Grote Bosatlas*, volume 52e editie. Wolters-Noordhoff Atlas Productions, Groningen.

Zijl, F., Verlaan, M., and Gerritsen, H. (2013). Improved water-level forecasting for the Northwest European Shelf and North Sea through direct modelling of tide, surge and non-linear interaction. *Ocean Dynamics*, 63(7):823–847.

Zimmerman, J. (1981). Dynamics, diffusion and geomorphological significance of tidal residual eddies. *Nature*, 290(5807):549.

Appendix A

Phases and amplitudes of tidal constituents

A.1 Default case

A.1.1 Initial state

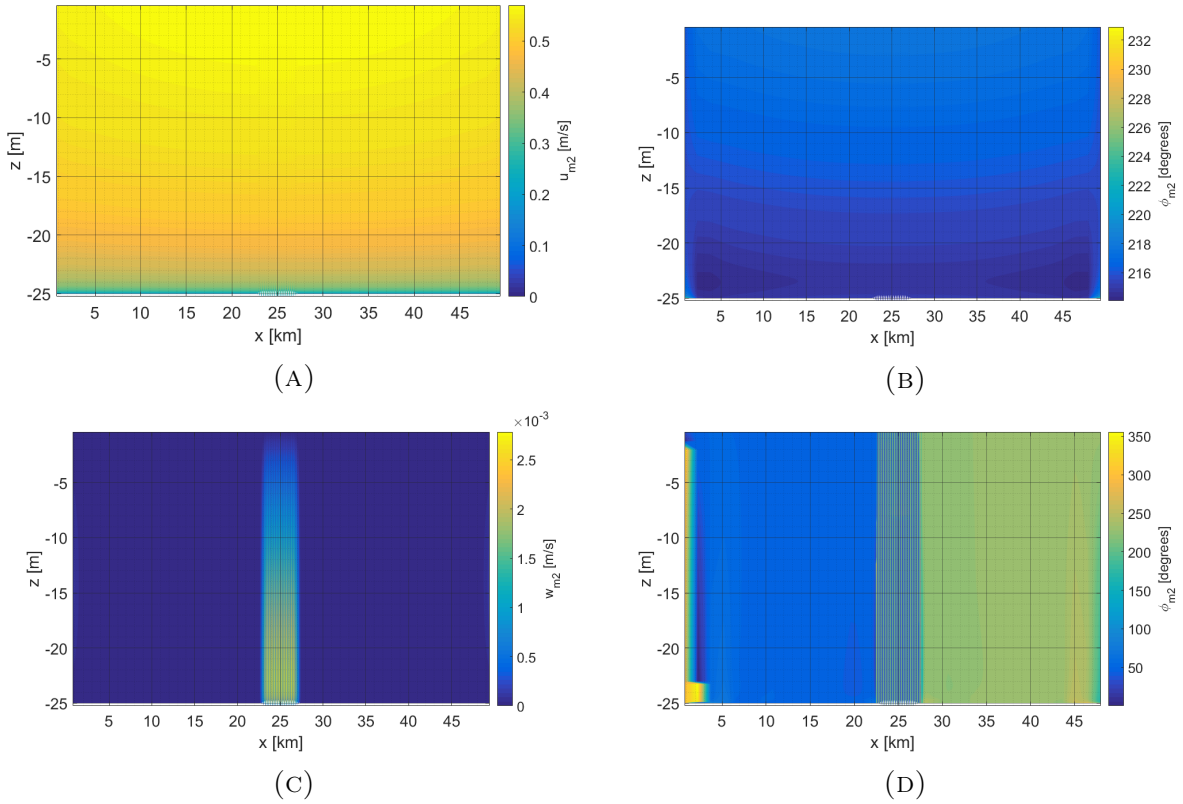

FIGURE A.1: M_2 amplitude (A) and phase (B) of horizontal velocity u at $t = 0$. M_2 amplitude (A) and phase (B) of vertical velocity w at $t = 0$.

A.1.2 Evolution over time

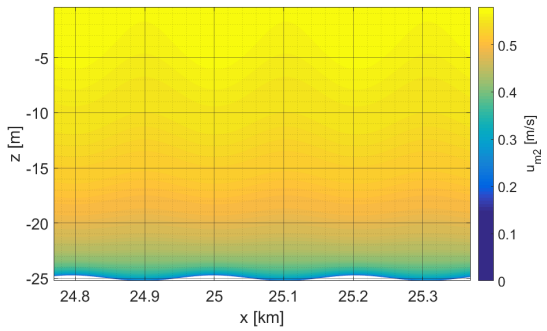

(A) $t_1 = 1$ year

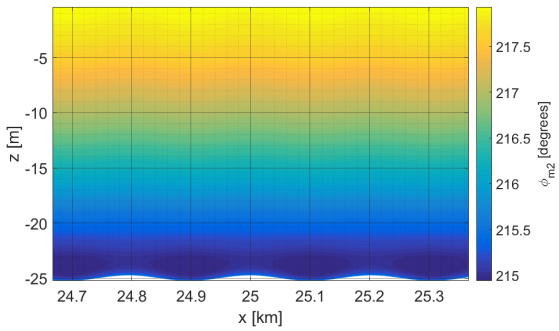

(B) $t_1 = 1$ year

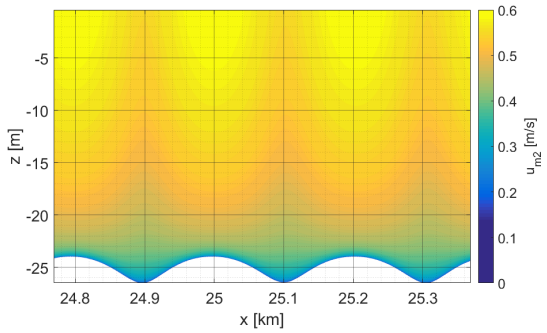

(C) $t_2 = 37.5$ years

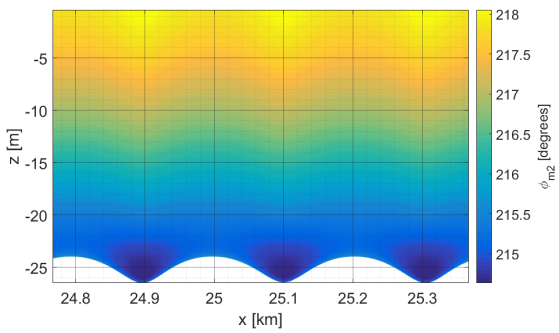

(D) $t_2 = 37.5$ years

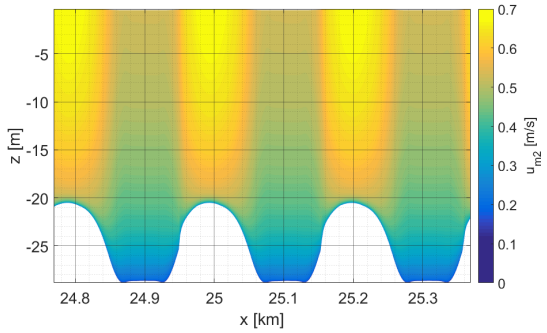

(E) $t_3 = 75$ years

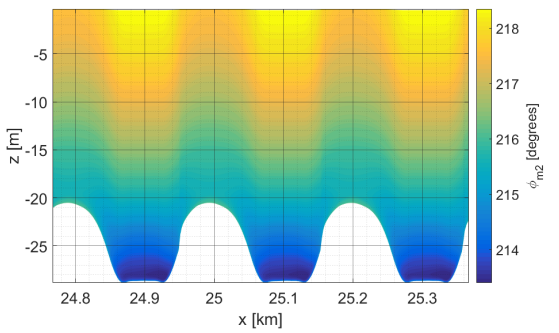

(F) $t_3 = 75$ years

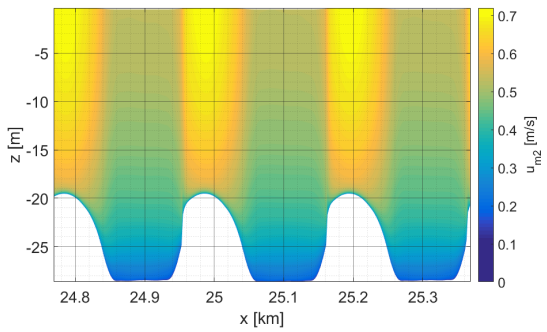

(G) $t_4 = 125$ years

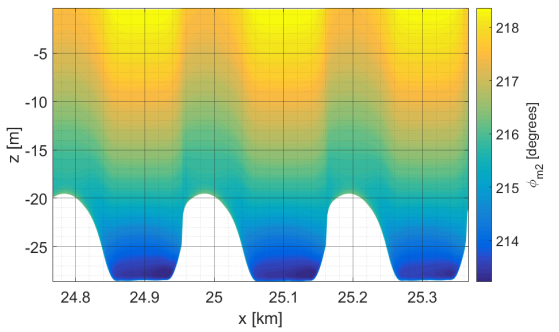

(H) $t_4 = 125$ years

FIGURE A.2: The amplitude (A) and phase (B) of M_2 of the horizontal velocity u at $t_1 = 1$ year, at $t_2 = 37.5$ ((C) and (D)), at $t_3 = 75$ years ((E) and (F)) and at $t_4 = 125$ years ((G) and (H)). Note the difference scales.

A.2 HKZ case

A.2.1 Phase and amplitude of M_2

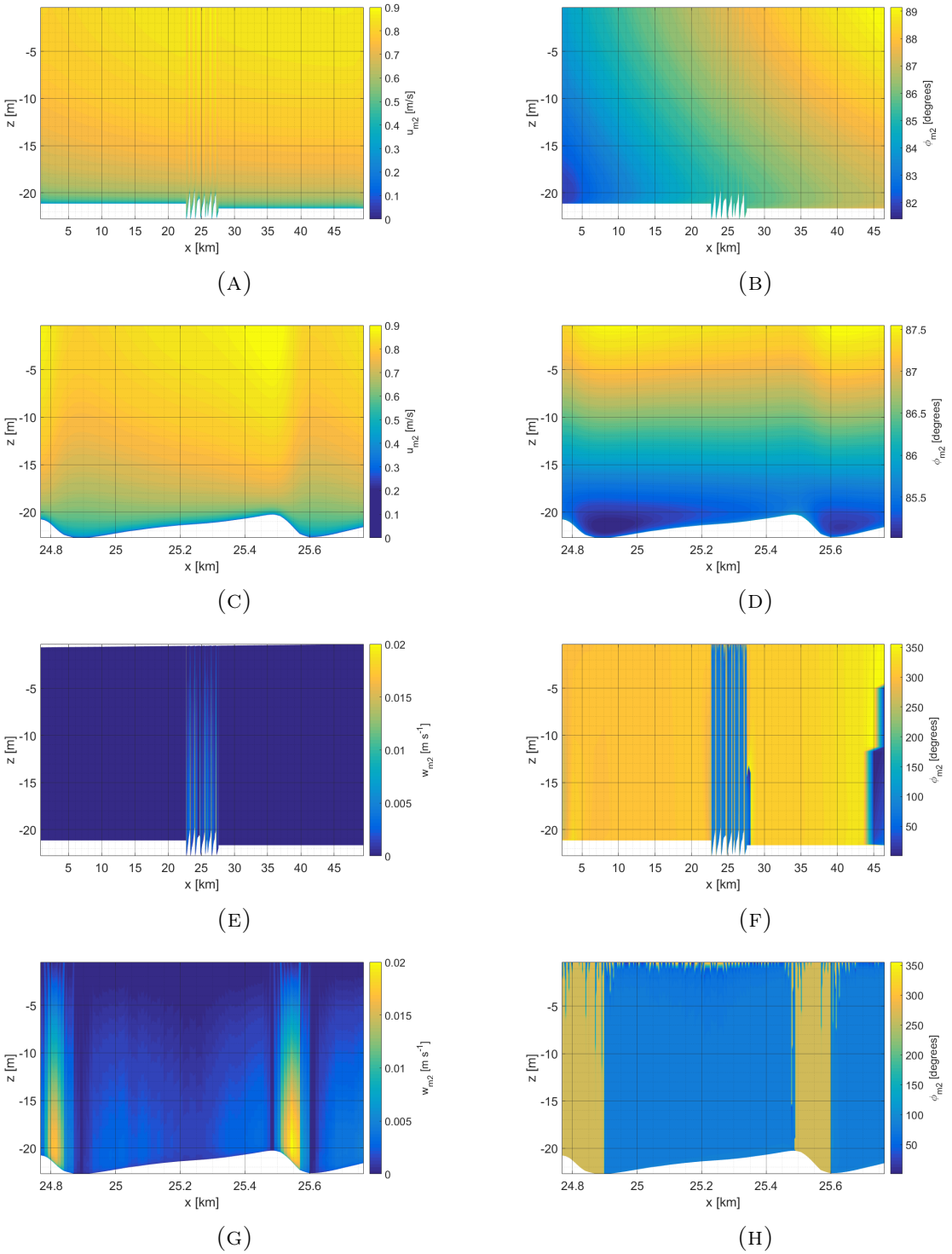

FIGURE A.3: M_2 amplitude (A) and M_2 phase (B) of the horizontal velocity u in the model domain and in the sand wave area ((C) and (D)). M_2 amplitude (E) and M_2 phase (F) of the vertical velocity w in the model domain and in the sand wave area ((G) and (H)).

A.2.2 Phase and amplitude of M_4

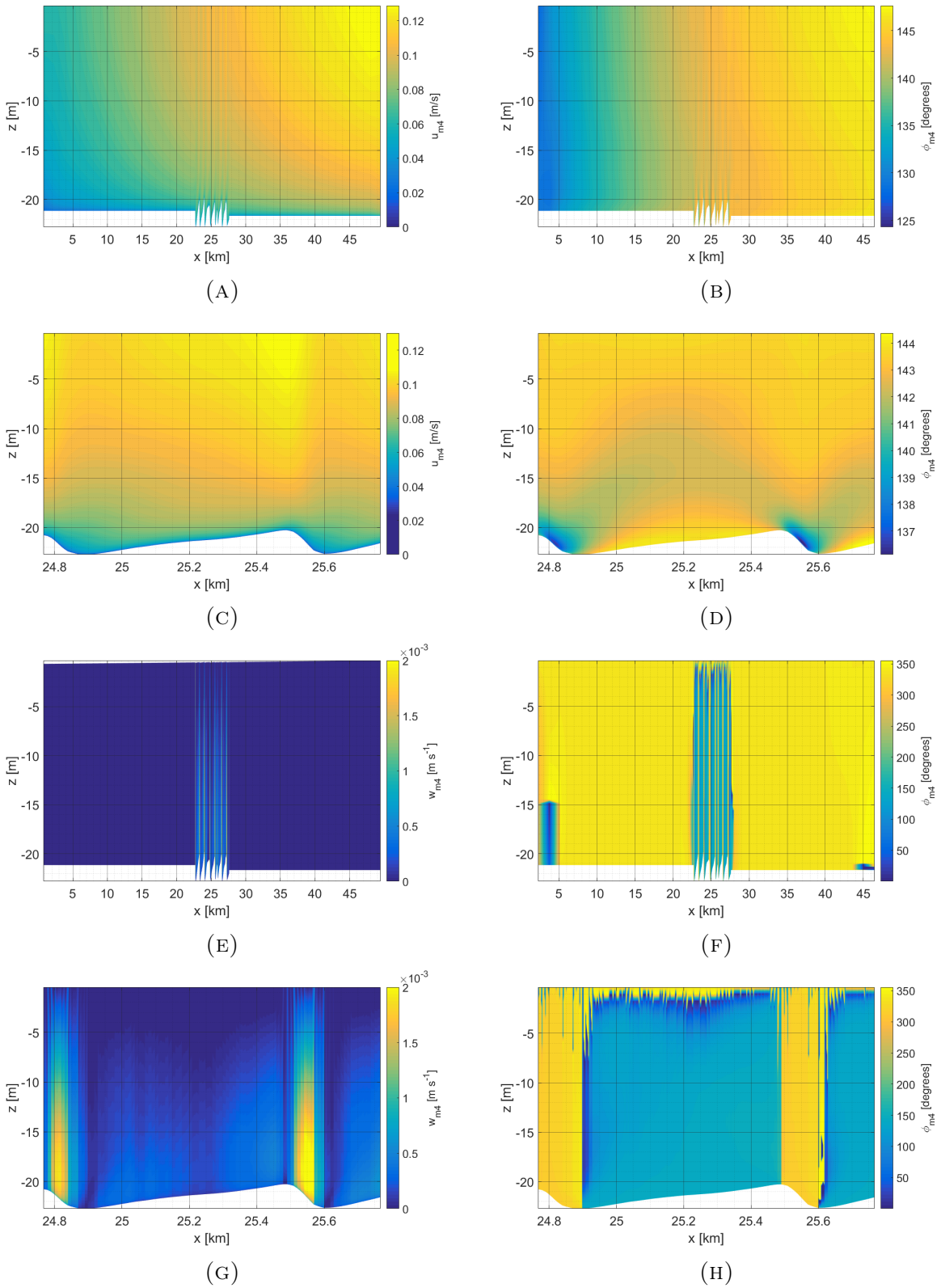

FIGURE A.4: M_4 amplitude (A) and M_4 phase (B) of the horizontal velocity u in the model domain and in the sand wave area ((C) and (D)). M_4 amplitude (E) and M_4 phase (F) of the vertical velocity w in the model domain and in the sand wave area ((G) and (H)).

Appendix B

Residual velocity

B.1 Default case

B.1.1 Time evolution

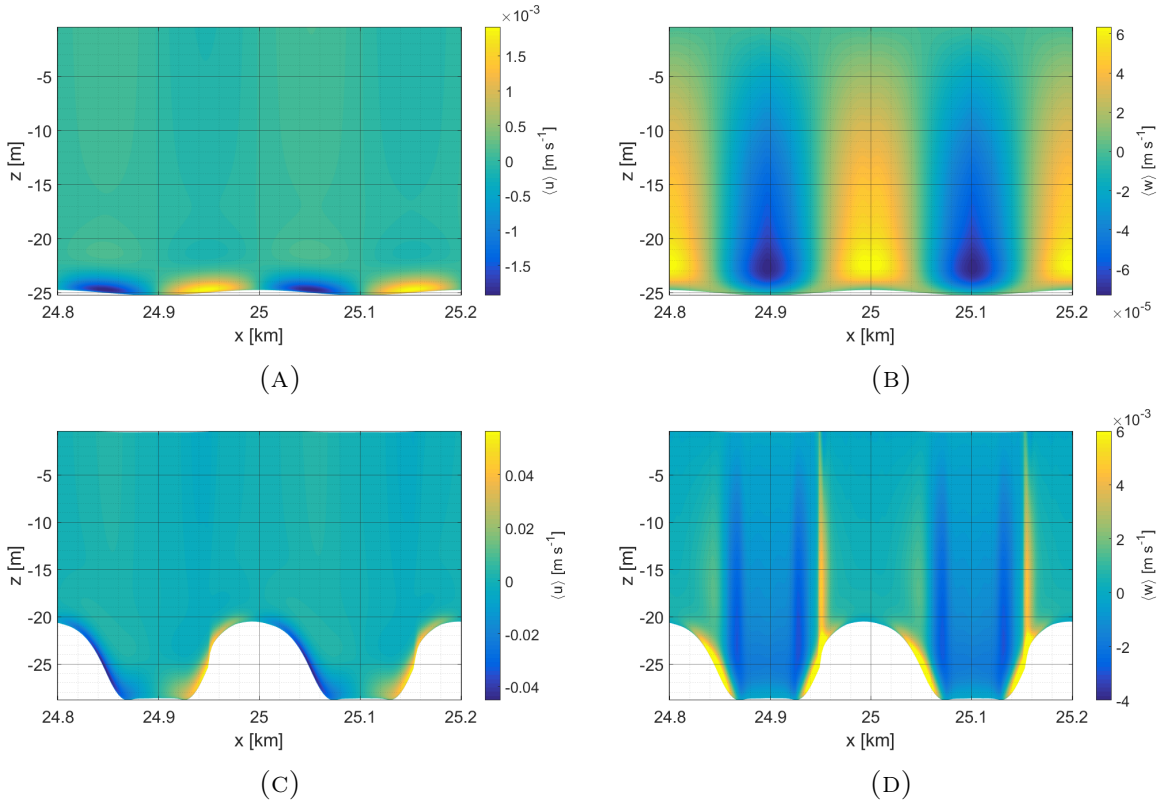

FIGURE B.1: The horizontal (A) and vertical (B) components of the residual velocity ($\langle u \rangle$ and $\langle w \rangle$) at $t = 1$ years. The horizontal (C) and vertical (D) components of the residual velocity ($\langle u \rangle$ and $\langle w \rangle$) at $t = 75$ years. Note the difference scales.

B.2 Time step

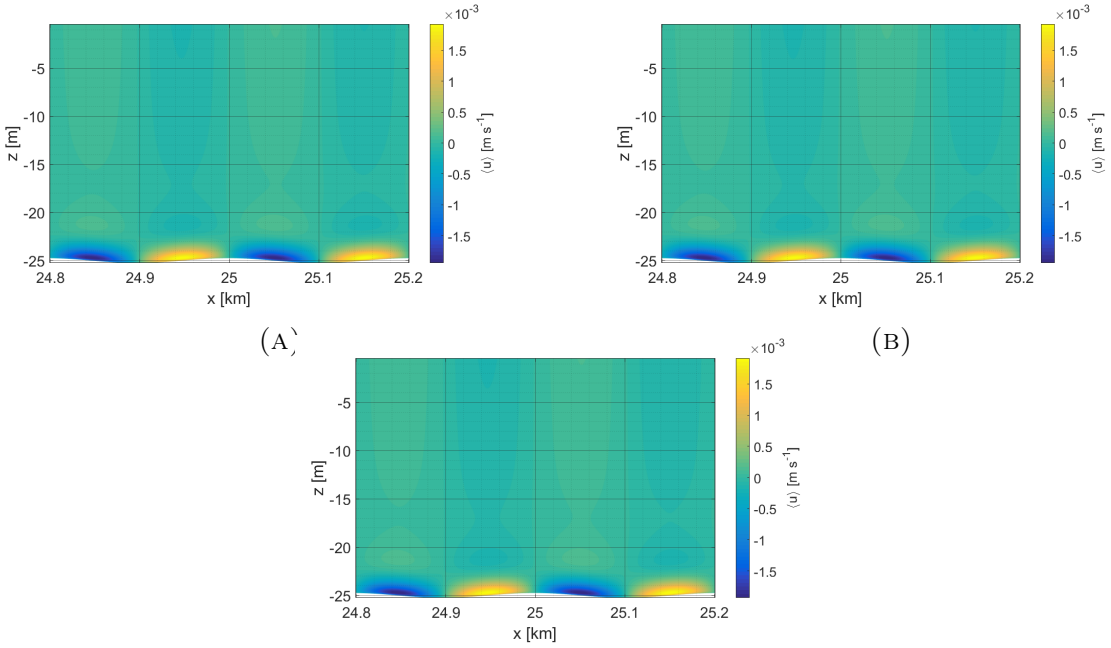

(A) (B)

(C)

FIGURE B.2: Horizontal component of the residual velocity $\langle u \rangle$ at $t = 0$ for $\Delta t = 6$ s (A), $\Delta t = 3$ s (B) and $\Delta t = 1.5$ s (C).

B.3 Vertical resolution

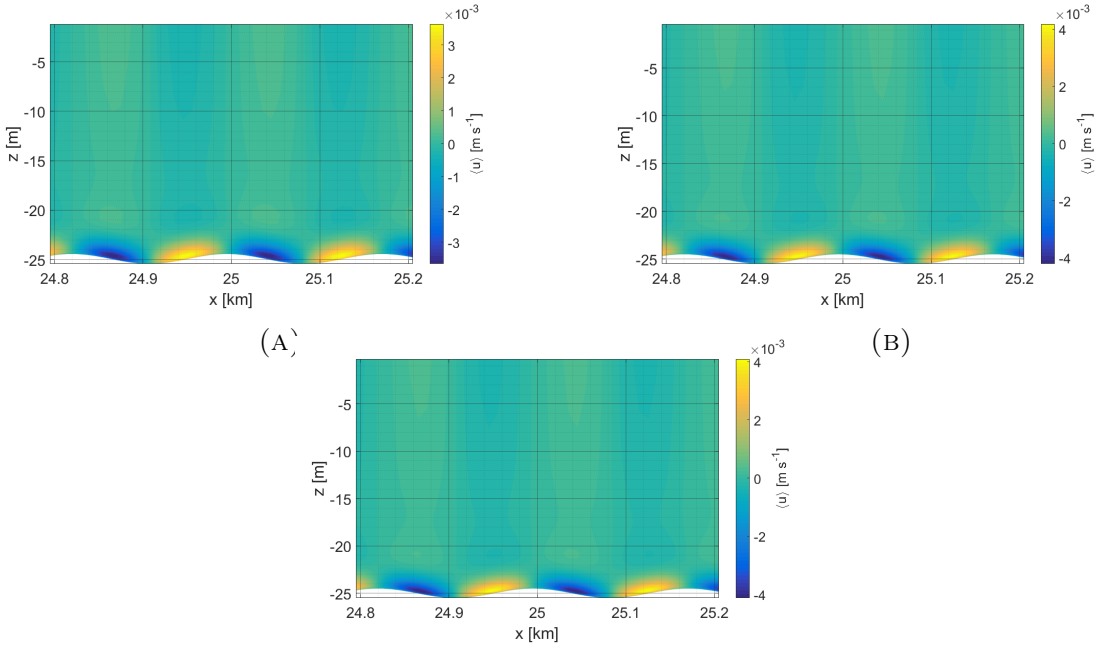

(A) (B)

(C)

FIGURE B.3: Horizontal component of the residual velocity $\langle u \rangle$ at $t = 0$ for 20 σ-layers (A), 60 σ-layers (B) and 100 σ-layers (C).

B.4 Horizontal grid spacing

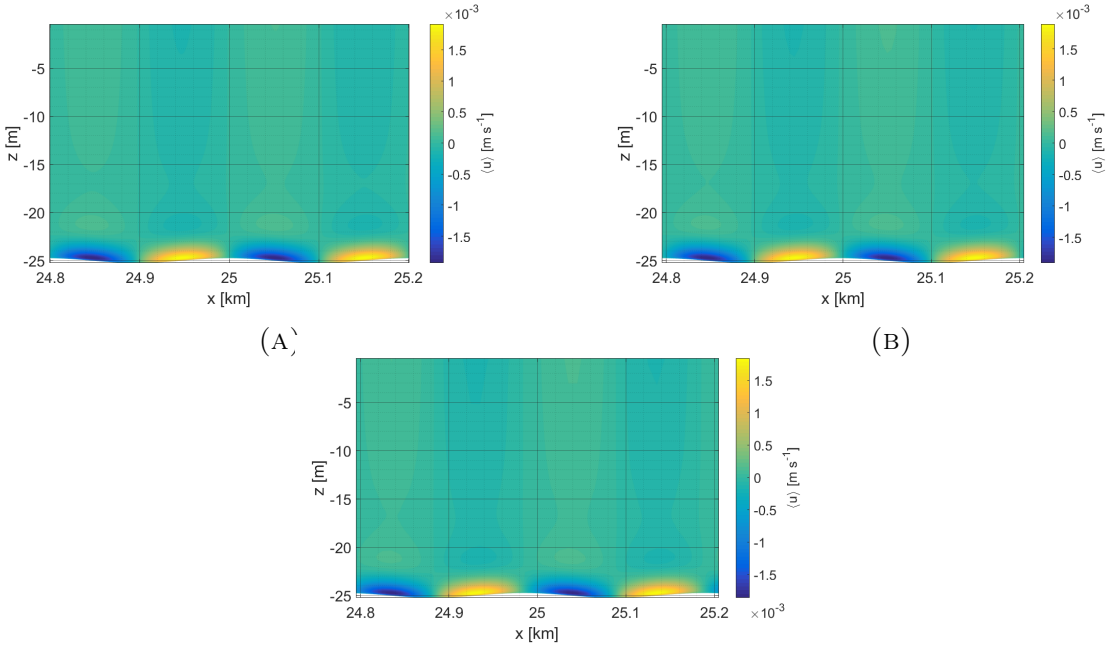

(A) (B)

(C)

FIGURE B.4: Horizontal component of the residual velocity $\langle u \rangle$ at $t = 0$ for $\Delta x = 2$ m (A), $\Delta x = 5$ m (B) and $\Delta x = 10$ m (C).

B.5 Water depth

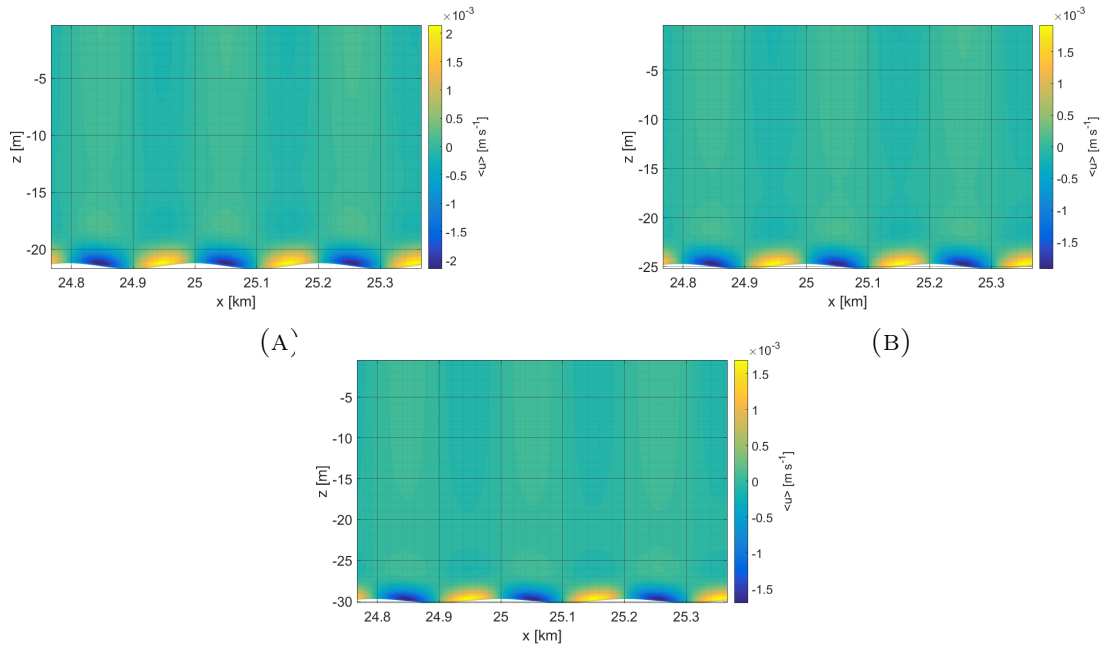

(A) (B)

(C)

FIGURE B.5: Horizontal component of the residual velocity $\langle u \rangle$ at $t = 0$ for $H_0 = 21.5$ m (A), $H_0 = 25$ m (B) and $H_0 = 30$ m (C).

B.6 Single tidal constituent

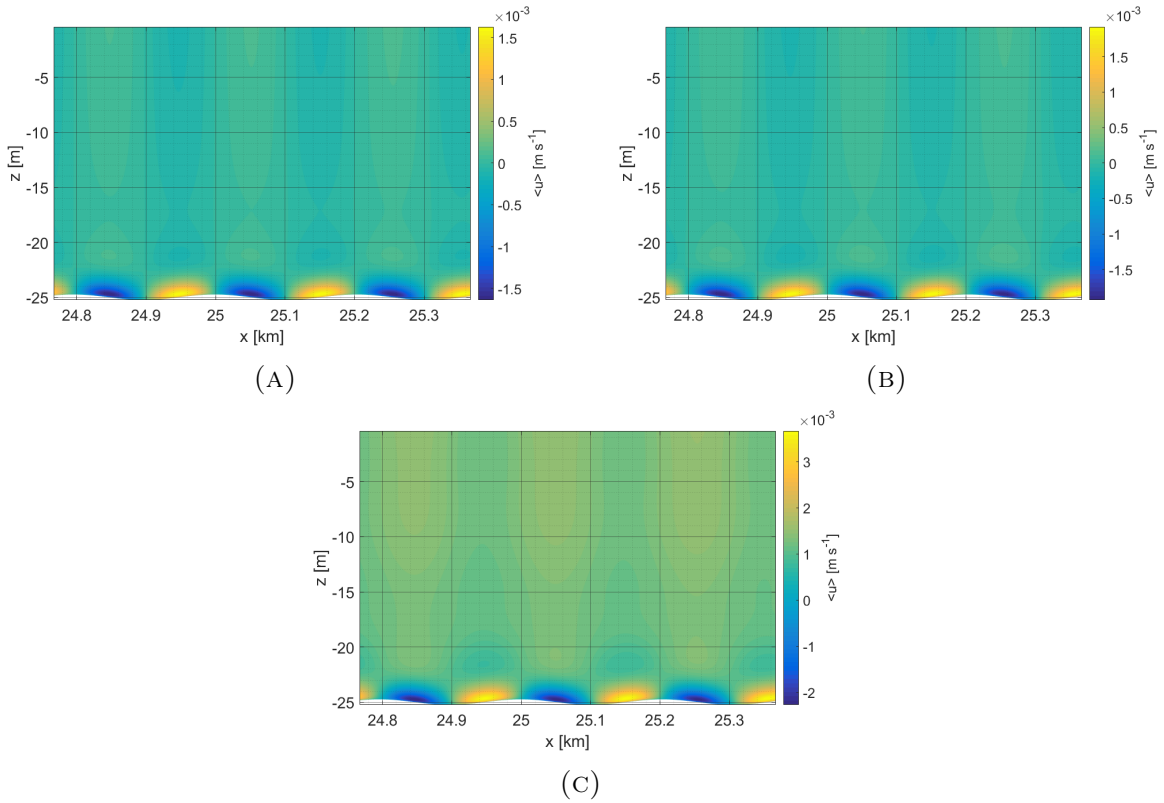

FIGURE B.6: Horizontal component of the residual velocity $\langle u \rangle$ at $t = 0$ for $M_2 = 0.5$ m s^{-1} (A), $M_2 = 0.6$ m s^{-1} (B) and $M_2 = 0.75$ m s^{-1} (C).

B.7 Multiple tidal constituents

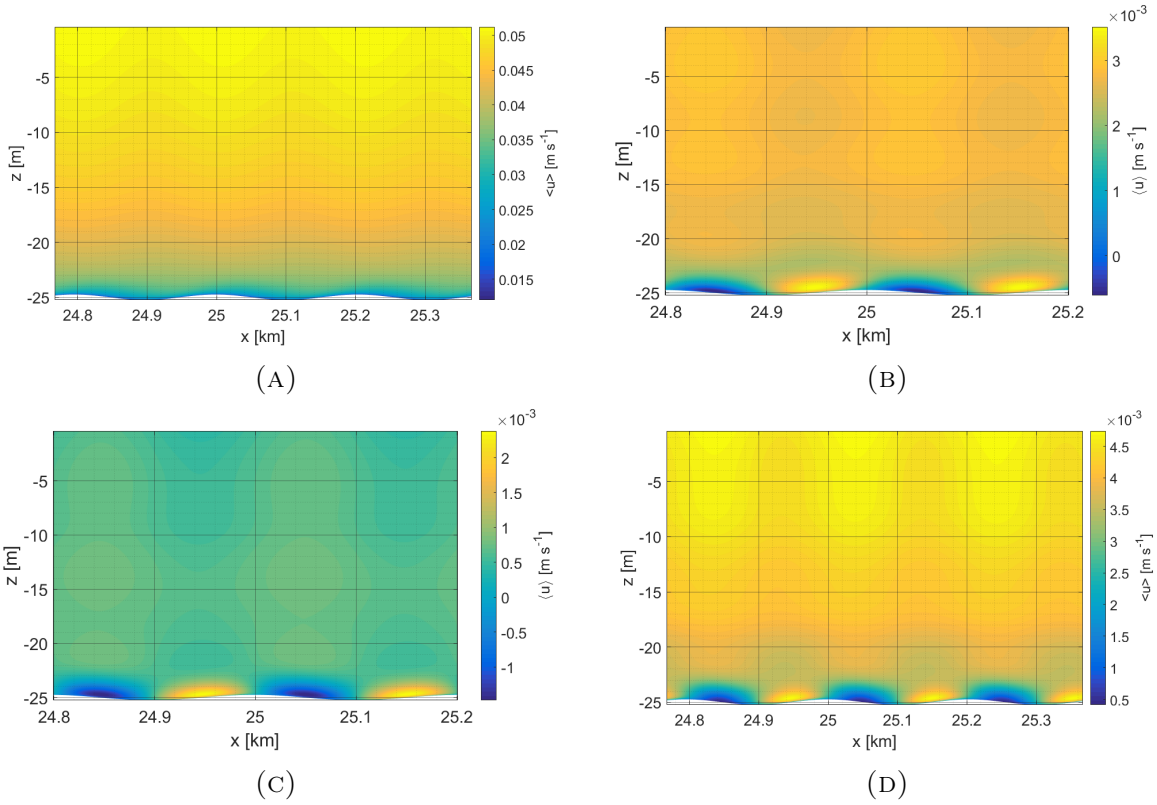

FIGURE B.7: Horizontal component of the residual velocity $\langle u \rangle$ at $t = 0$ for M_2 and M_0 (A), M_2 and M_4 with $\theta = 60°$ (B), M_2 and M_4 with $\theta = 120°$ (C) and M_2 and M_4 with $\theta = 180°$ (D).

B.8 HKZ Case

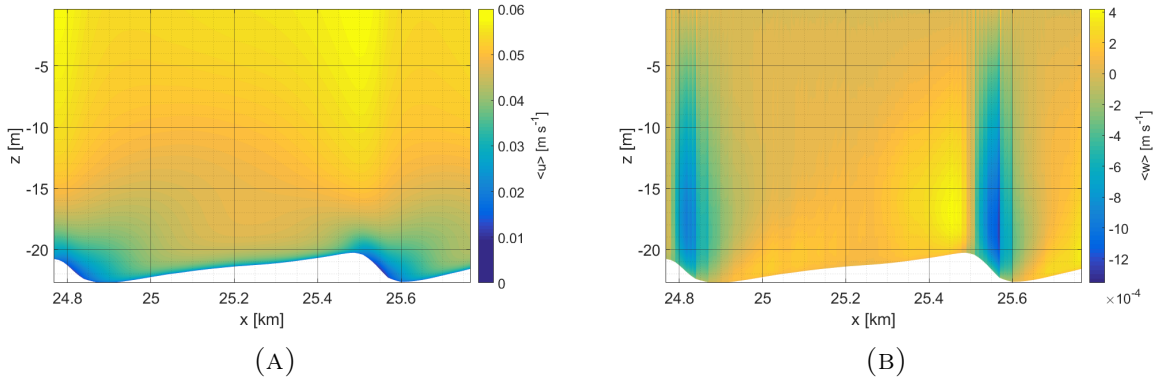

FIGURE B.8: The horizontal (A) $\langle u \rangle$ and vertical component (B) $\langle \omega \rangle$ of the residual velocity in the HKZ case at $t = 0$.

Appendix C

Residual sand transport

C.1 Default case

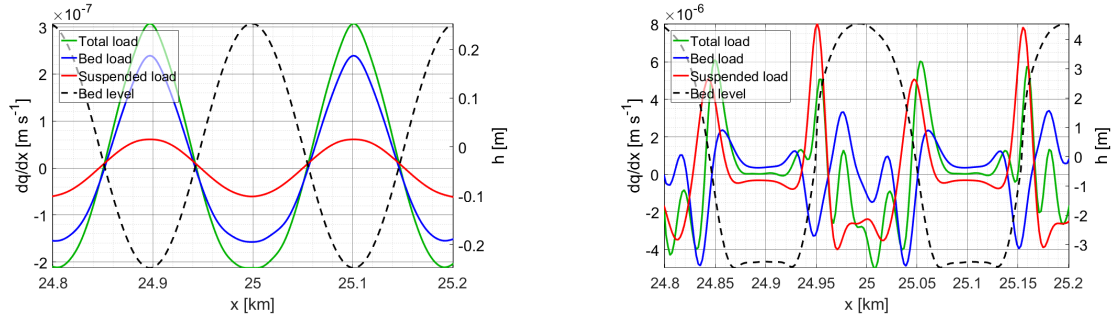

(A) (B)

FIGURE C.1: Horizontal gradient of the residual bed load transport $\frac{\partial \langle q_b \rangle}{\partial x}$ (blue), residual suspended load transport $\frac{\partial \langle q_s \rangle}{\partial x}$ (red) and residual total transport $\frac{\partial \langle q_t \rangle}{\partial x}$ (green) at $t_1 = 1$ year (A) and $t_3 = 75$ years (B).

C.2 MORFAC

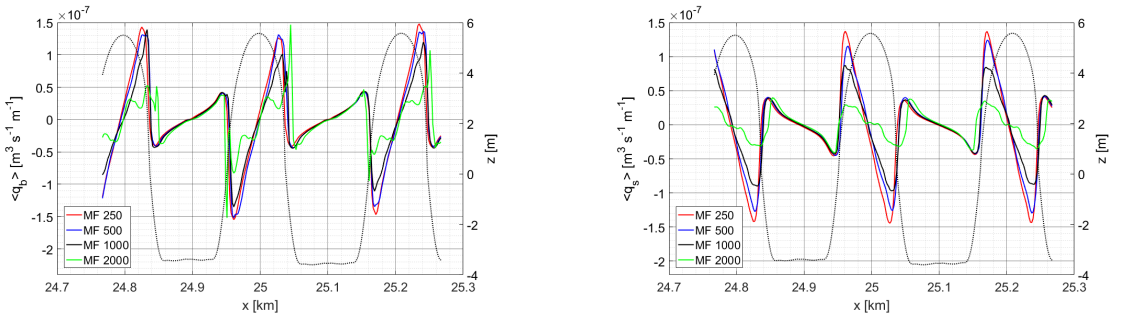

(A) (B)

FIGURE C.2: Residual bed load $\langle q_b \rangle$ and suspended load $\langle q_s \rangle$ transport for MF = 250 (red), MF = 500 (blue), MF = 1000 (black) and MF = 2000 (green) at $t = 150$ years.

C.3 HKZ Case

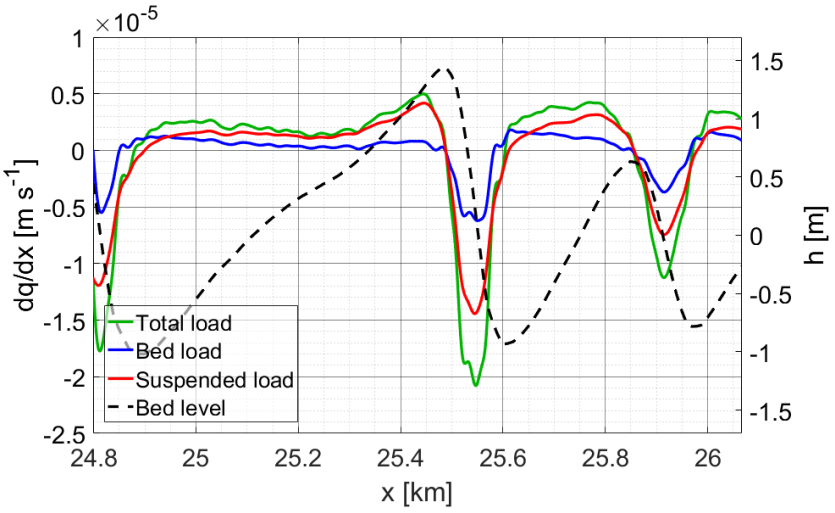

FIGURE C.3: Horizontal gradient of the residual bed load transport $\langle q_b \rangle$ (blue), residual suspended load transport $\langle q_s \rangle$ (red) and residual total transport $\langle q_t \rangle$ (green) for the HKZ Case at $t = 0$, for M_2, M_4 and M_0.

C.4 Suspended sand concentration

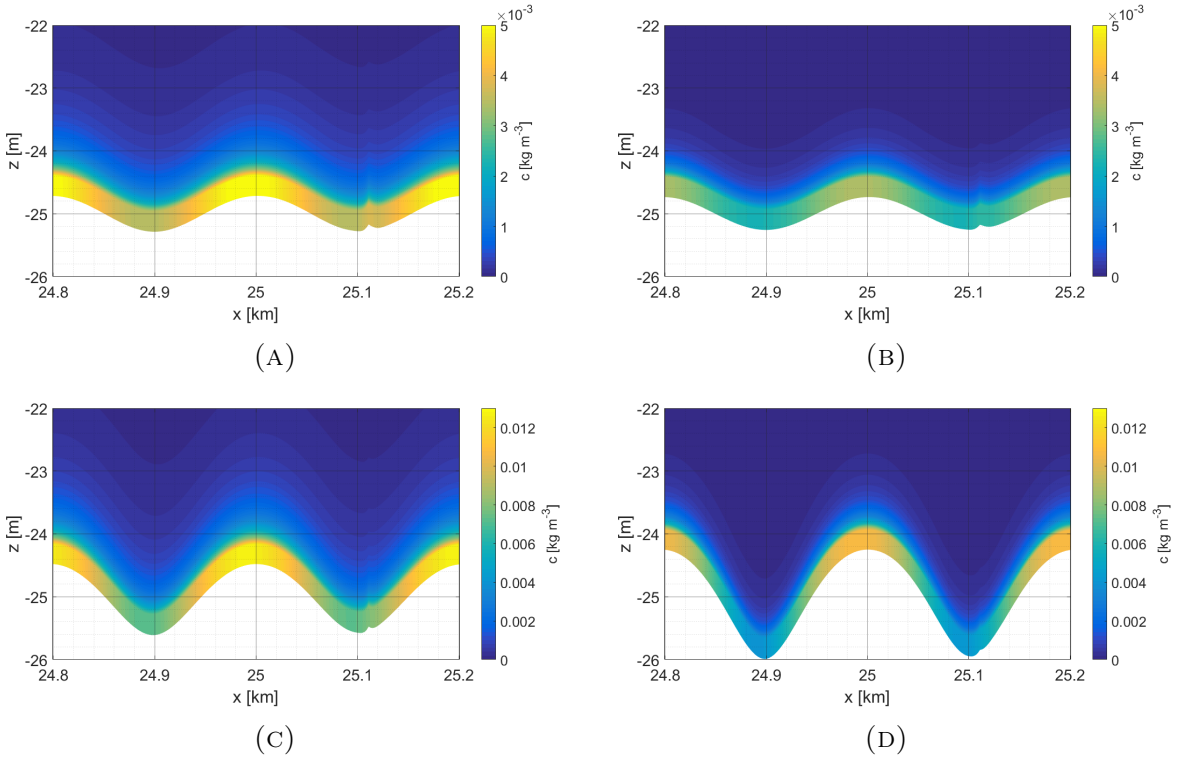

FIGURE C.4: (A) Suspended sand concentration c (kg m$^-$3) at $t = 4$ years for $d_{50} = 0.25$ mm. (B) Suspended sand concentration c (kg m$^-$3) at $t = 4$ years for $d_{50} = 0.35$ m. (C) Suspended sand concentration c (kg m$^-$3) at $t = 30$ years for $d_{50} = 0.25$ mm. (D) Suspended sand concentration c (kg m$^-$3) at $t = 30$ years for $d_{50} = 0.35$ mm.

Appendix D

Neumann boundary conditions

Some of the HKZ runs were also performed using Neumann boundary conditions. This was done in order to investigate whether this resulted in a different flow and sediment transport than when Riemann boundary conditions are imposed. Here, a water level condition ζ was imposed at $x = 0$ and $x = L_x$. At the sea ward boundary, a Neumann boundary condition was applied. To make sure that the tidal wave can pass through the boundaries, the reflection parameter α is set to 0. The Neumann boundary condition prescribes alongshore water-level gradient $\frac{\partial \zeta}{\partial x}$ with x the alongshore coordinate, which is normal to $x = 0$ and $x = L_x$. The model is forced by a tidal wave with harmonic constituents M_2 and M_4, which travels from the southwestern ($x = 0$) to the northeastern boundary ($x = L_x$). The propagation of ζ along the coast is:

$$\zeta(x,t) = \hat{\zeta}_2 \cos(\omega_2 t - \kappa_2 x - \phi_2) + \hat{\zeta}_4 \cos(2\omega_2 t - \kappa_4 x - \phi_4). \tag{D.1}$$

Here, $\hat{\zeta}_2$ and $\hat{\zeta}_4$ are the amplitudes, ω and 2ω the angular frequencies, κ_2 and κ_4 the alongshore wavenumbers and ϕ_2 and ϕ_4 the phases.

The alongshore water level gradient $\frac{\partial \zeta}{\partial x}$ at the sea ward boundary can be approximated by computing difference quotient of water level at the corner points ($x = 0$ and $x = L_x$). This results in

$$\frac{\partial \zeta(x,t)}{\partial x} \simeq \sum_j^2 \frac{\hat{\zeta}_{j,2} \cos(\omega_j t - \phi_{j,2}) - \hat{\zeta}_{j,1} \cos(\omega_j t - \phi_{j,1})}{L_x} = \sum_j^2 \frac{\hat{\zeta}_{j,3} \cos(\omega_j t - \phi_{j,3})}{L_x}. \tag{D.2}$$

In this expression, subscript j refers to tidal components M_2 and M_4, respectivel, $\hat{\zeta}_{i,1}$ and $\hat{\zeta}_{i,2}$ are amplitude of each tidal component in points $x = 0$ and $x = L_x$, respectively, $\phi_{i,1}$ and $\phi_{i,2}$ their corresponding phases (in degrees), and L_x is the alongshore distance between the two points. Expressions for amplitude $\hat{\zeta}_{j,3}$ and phase $\phi_{j,3}$ are obtained by applying straightforward algebra. The result is

$$\zeta_{j,3} = \sqrt{(\zeta_{j,2}\cos\phi_{j,2} - \zeta_{j,1}\cos\phi_{j,1})^2 + (\zeta_{j,2}\sin\phi_{j,2} - \zeta_{j,1}\sin\phi_{j,1})^2}, \tag{D.3}$$

$$\phi_{j,3} = \arctan\frac{\zeta_{j,2}\sin\phi_{j,2} - \zeta_{j,1}\sin\phi_{j,1}}{\zeta_{j,2}\cos\phi_{j,2} - \zeta_{j,1}\cos\phi_{j,1}}. \tag{D.4}$$

Gradient $\frac{\partial \zeta}{\partial x}$ is assumed to be constant over the entire length of the boundary